Fresnel Zone Antennas

Y. Jay Guo and Stephen K. Barton

Kluwer Academic Publishers

Fresnel Zone Antennas

Y. Jay Guo and Stephen K. Barton

Written by leading experts in the field, this book is a research monograph on Fresnel Zone Antennas. Fresnel zone antennas refer to reflector and lens antennas based on the Fresnel zone concept and phase correction techniques. Unlike the conventional reflector and lens antennas, the focusing effect in a Fresnel zone antenna is achieved by controlling the phase shifting property of the surface rather than its shape, thus allowing flat or arbitrary configurations. Other advantages of Fresnel zone antennas include low manufacturing and installation cost and ease of packaging. The material presented is mainly drawn from the theoretical and experimental work published and unpublished by the authors.

The book is intended to serve engineers, researchers and students in the fields of antennas, microwave and millimetre-wave engineering, radar, optics and telecommunications. In the book, readers will find the wealth of novel antenna configurations, first hand experimental results, and a large number of equations useful in the research, analysis and design of Fresnel zone antennas.

ISBN 1-4020-7124-8
9 781402 071249

KLUWER ACADEMIC PUBLISHERS

Fresnel Zone Antennas
Y. Jay Guo and Stephen K. Barton

KAP

Fresnel Zone Antennas
Y. Jay Guo and Stephen K. Barton

Kluwer Academic Publishers

Fresnel Zone Antennas

by

Y. Jay Guo
Mobisphere Ltd.,
A Siemens and NEC Company

and

Stephen K. Barton
The University of Manchester

KLUWER ACADEMIC PUBLISHERS
BOSTON / DORDRECHT / LONDON

A C.I.P. Catalogue record for this book is available from the Library of Congress.

ISBN 1-4020-7124-8

Published by Kluwer Academic Publishers,
P.O. Box 17, 3300 AA Dordrecht, The Netherlands.

Sold and distributed in North, Central and South America
by Kluwer Academic Publishers,
101 Philip Drive, Norwell, MA 02061, U.S.A.

In all other countries, sold and distributed
by Kluwer Academic Publishers,
P.O. Box 322, 3300 AH Dordrecht, The Netherlands.

Printed on acid-free paper

Printed in the Netherlands.

Contents

Acknowledgement

The authors would like to express their gratitude to the UK Engineering and Physical Science Research Council and Mawzones Ltd for their sponsorship of the research, which generated most of the material presented in the book. We are indebted to Mr T. M. B. Wright, Mr. G. Colinge and Dr I. H. Sassi for their support and assistance which the authors received in the course of several projects on Fresnel zone antennas. Special thanks go to their families for the love, kind understanding and support the authors have enjoyed.

Chapter 1 Introduction

This book is a research monograph on Fresnel zone antennas. It covers various lens and reflector antennas based on the Fresnel zone concept and phase correction techniques. The material presented is mainly drawn from the theoretical and experimental work published and unpublished by the authors. The book is intended to serve engineers, researchers and students in the fields of antennas, microwave and millimetre-wave engineering, radar, optics and telecommunications. The authors hope that readers will find the wealth of unique antenna configurations and the theoretical framework presented inspirational, and the large number of equations useful in the analysis and design of Fresnel zone antennas.

1.1 Historical Background

Conventionally, electrically large antennas are classified into two main categories according to the feed arrangements. In the first category, the aperture is illuminated by a small feed antenna placed at the focus of a reflector or lens, which is often curved, bulky and of canonical profile. In reception, the electromagnetic energy intercepted by the reflector or lens is re-directed to the feed located at the focal point through reflection or refraction. The second category, array antennas, consist of a number of small radiating elements fed by a network of transmission lines, often in the plane of the array aperture itself.

For a conventional reflector or lens antenna, the radiation pattern is controlled mainly by the shape of the reflector or lens. With tight mechanical tolerance, a reflector or lens antenna can achieve very high efficiency and very low sidelobes. Disadvantages of conventional reflector and lens antennas include high production and installation cost, bulky structure and unsightly appearance, which are especially undesirable for consumer products. In contrast, the array antenna, especially the printed array antenna, is of compact low-profile structure. It does not need a separate feed antenna, and can be made cheaply for mass production. In principle, a printed array can be beam-steered by electronically tunable phase shifters, but this is too expensive for commercial products, such as receivers for the Direct Broadcasting Satellite (DBS) service. Printed array antennas commercially

available for DBS receivers in Europe, North America and Japan are normally tilted out from the wall of a building when being installed. Furthermore, as the aperture of a printed array antenna and hence the directivity increases, the intrinsic loss of the feeding network also increases, ultimately faster than the directivity of the array. Therefore, printed array antennas are normally regarded as suitable only for low and medium gain (less than 25dB) antennas.

Alongside the two mainstream types of antennas, another type is emerging as a promising candidate on the consumer electronics market, the Fresnel zone antenna. The Fresnel zone antenna belongs to the category of reflector and lens antennas. Unlike the traditional reflector and lens antennas, however, the focusing effect in a Fresnel zone antenna is achieved by controlling the phase shifting property of the surface rather than its shape, thus allowing flat or arbitrary configurations. For historical reasons, a flat Fresnel zone antenna is termed a Fresnel zoneplate antenna. An offset Fresnel zoneplate reflector can be flush mounted to the wall or roof of a building, and an offset Fresnel lens can be printed on a window or made conformal to the body of a vehicle.

The advantages of the Fresnel zoneplate antenna are numerous. It is normally cheap to manufacture and install, easy to transport and package and can achieve high gain. Owing to its flat nature, the windloading force of a Fresnel zoneplate can be as little as 1/8 of that of conventional solid or wire-meshed reflectors of similar size. When used at frequencies above microwave, a Fresnel zone antenna can be an integral device and becomes even more competitive than the microstrip antenna array.

The simplest Fresnel zoneplate antenna is the circular half-wave zoneplate invented in the nineteenth century [1, 2]. The basic idea is to divide a plane aperture into circular zones with respect to a chosen focal point on the basis that all radiation from each zone arrives at the focal point in phase within $\pm\pi/2$ range. If the radiation from alternate zones is suppressed or shifted in phase by π, an approximate focus is obtained and a feed can be placed there to collect the received energy effectively. Despite its simplicity, the half-wave zoneplate remained mainly as an optical device for a long time, partly because its efficiency is too low (less than 20%) and the sidelobe level of its radiation pattern is too high to compete with conventional dishes, and partly because antenna cost was not a crucial issue

for military equipment. Compared with conventional reflector and lens antennas, reported research on microwave and millimetre-wave Fresnel zone antennas appears to be limited. In 1948, Maddaus published the design and experimental work on stepped half-wave lens antennas operating at 23GHz and sidelobe levels of around -17dB were achieved [3]. In 1961, Buskirk and Hendrix reported an experiment on simple circular phase reversal zoneplate reflector antennas for radio frequency operation [4]. Unfortunately, the sidelobe level they achieved was as high as -7 dB. In 1987, Black and Wiltse published their theoretical and experimental work on the stepped quarter-wave zoneplate at 35GHz. A sidelobe level of about -17dB was achieved [5]. A year later a phase reversal zoneplate reflector operating at 94GHz was reported by Huder and Menzel, and 25% efficiency and -19dB sidelobe level were obtained [6]. An experiment on a similar antenna at 11.8GHz was reported by NASA researchers in 1989. 5% 3dB bandwidth and -16dB sidelobe level were measured [7].

Until the 1980s, the Fresnel zoneplate antenna was regarded as a poor candidate for microwave applications. Following the development of DBS services in the eighties, however, antenna engineers began to consider the use of Fresnel zoneplates as candidate antennas for DBS reception, where antenna cost is an important factor [8]. A British firm, Mawzones Ltd., was inspired by the simplicity and ease of fabrication of zoneplates and started marketing zoneplate antenna products in the late 1980s [9]. This, to some extent, promoted the research on Fresnel zone antennas which the authors and their colleagues carried out between 1990 and 1997 at the University of Bradford, United Kingdom. The research was mainly sponsored by the UK Science and Engineering Research Council (SERC) and Mawzones Ltd. It proved to be fruitful; several novel antenna configurations were developed, offering higher efficiency and lower sidelobes, and a number of papers [10 – 19], [27 – 31], [38], [40], [44], [46], [48 , 49], [59 – 61] were published by the authors and their colleagues.

1.2 Outline of the Book

Based on our own published and unpublished work, this book provides a systematic introduction to the theory, design and practical performance of Fresnel zone antennas, especially Fresnel zoneplate antennas. It is not only written for antenna engineers and researchers, but also applied physicists, students and radio amateurs. It is interesting to note

that simple Fresnel zoneplate antennas have been successfully used at the University of Southampton, U. K., on open days to entertain and educate potential students of Electrical and Electronic Engineering.

The book is organised as follows. Chapter 2 presents a thorough study on the geometrical characteristic of offset Fresnel zoneplates. Explicit equations for designing offset Fresnel zoneplate antennas are given. In contrast to the symmetrical circular Fresnel zoneplate, an offset zoneplate consists of a set of elliptical zones [10]. This feature introduces some new problems to the analysis of offset Fresnel zoneplate antennas. Formulae and algorithms for predicting the radiation pattern of a Fresnel lens antenna are presented. Experimental results of an offset Fresnel lens antenna are reported [11]. Although a simple Fresnel lens antenna has low efficiency, it serves as a very attractive indoor candidate when a large window or an electrically transparent wall is available. In the application of DBS service, for example, an offset Fresnel lens can be produced by simply painting a zonal pattern on a window glass or a blind with conducting material. The satellite signal passing through the transparent zones is then collected by using an indoor feed [12].

To increase the efficiency of Fresnel zoneplate antennas, one can divide each Fresnel zone into several sub-zones, such as quarter-wave sub-zones, and provide an appropriate phase shift in each of them, thus resulting in a sub-zone phase correcting zoneplate. The problem with dielectric based zoneplate lens antenna is that whilst a dielectric is providing a phase shift to the transmitted wave, it inevitably reflects some of the energy back, so the efficiency of such a lens is limited. However, the low efficiency problem for a zoneplate reflector is less severe, as total reflection can be achieved by using a conducting reflector behind the zoneplate. Based on the focal field analysis, chapter 3 presents a theory of the sub-zone phase correcting technique [13]. This is followed by some theoretical studies on the efficiency and sidelobe performance of zoneplate antennas. Then, it is demonstrated that high efficiency zoneplate reflectors can be obtained by employing the multilayer phase correcting technique, which is to use a number of dielectric slabs of low permittivity and print different metallic zonal patterns on the different interfaces. The design and experiments of circular and offset multilayer phase correcting zoneplate reflectors are described in this chapter [14, 15].

Chapter 4 presents a theoretical study of zonal reflectors using the moment method. The objective is to provide some insight into the sidelobe limit of zoneplate antennas and demonstrate a new approach to reducing the sidelobe level of stepped Fresnel zoneplate antennas. It is shown that although corner diffraction makes significant contribution to the sidelobe level, zoning intrinsically produces high far-out sidelobes [16].

A problem with the multilayer zoneplate reflector is the complexity introduced, which might offset the advantage of using Fresnel zoneplate antennas. One solution is to print an inhomogeneous array of conducting elements on a grounded dielectric plate, thus leading to the so-called single-layer printed flat reflector [17]. This configuration bears much in common with the printed array antenna but it requires the use of a feed antenna instead of a feeding network. In contrast to the normal array antenna, the array elements are different and are arranged in a pseudo-periodic manner. Chapter 5 presents the theory and design method of single layer printed flat reflectors incorporating conducting rings. Experimental results on such an antenna operating in the X-band are described [18]. In addition, two similar designs, one incorporating patches and holes and the other known as FLAPS™ by Malibu Research, are introduced. Naturally, this chapter leads to a more general antenna concept, the passive reflective phase correcting array.

A passive reflective phase correcting array consists of an array of phase shifting elements illuminated by a feed placed at the focal point [19]. The word "passive" refers to the fact that the array does not have electronic phase shifters connected to the elements, and "reflective" refers to the fact that each element reflects back the energy in the incident wave with an appropriate phase shift. Each element can be designed to either produce a phase shift which is equal to that required at the element centre, or provide some quantised phase shifting values. Although the former does not seem to be commercially attractive, the latter proved to be a practical antenna configuration. One potential advantage is that such an array can be reconfigured by changing the positions of the elements to produce different radiation patterns. Chapter 6 gives a systematic theory of the phase efficiency of passive phase correcting array antennas and experimental results on an X-band prototype are reported [19].

Finally, chapter 7 introduces a wider range of Fresnel zone antennas of various configurations for different applications and offers some directions for future study.

Chapter 2 Offset Fresnel Zoneplate

The most common form of Fresnel zone reflectors and lenses is the circular zoneplate. The design of the simple circular zoneplate is well documented in the open literature, and experiments at various frequencies and with various configurations had been reported from time to time since late nineteenth century [1-7]. However, no serious attention was paid to the offset or elliptical zoneplate until the 1980s [2, 9]. This might be due to the fact that "offset feeding" is mainly a microwave antenna concept and flush mounting a zoneplate to a chosen surface was not regarded as an important issue for optical and millimetre devices. In this chapter, a thorough study on the geometrical characteristics of offset zoneplates is presented and explicit design equations of offset zoneplate antennas are given. Then, based on the physical optics approximation, formulae for calculating the radiation pattern of offset Fresnel lens antennas are derived [11]. Owing to the asymmetry caused by the offset configuration, calculation of the radiation integral can be time-consuming, so solutions to this problem are also provided in this chapter. Finally, an experiment on the offset Fresnel lens antenna is reported.

2.1 Circular Zoneplate

A simple circular zoneplate consists of a series of concentric opaque and transparent ring-like zones (see Fig. 2.1), which can be used as either a lens or a reflector. When used for reception, the function of energy collection is performed by the transparent zones for the transmission zoneplate (Fresnel lens) or opaque zones for the reflection zoneplate (Fresnel zone reflector). Since the efficiency of a reflection zoneplate can be easily improved by placing a conducting plate a quarter wavelength behind the zoneplate [4], which makes the contribution from the transparent zones in phase with that from opaque zones, the simple zoneplate is mainly used as a lens. In the following, some fundamental equations for designing the simple circular zoneplate are given.

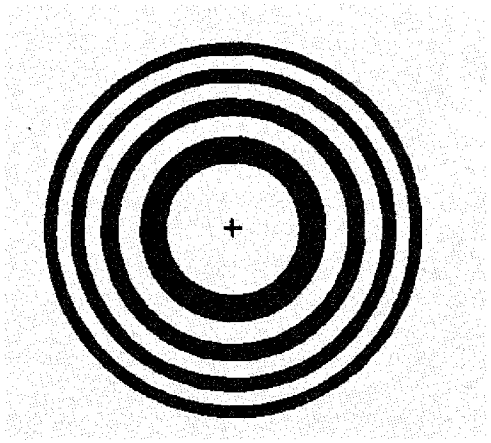

Fig. 2.1 Illustration of a circular zoneplate.

According to Huygen's diffraction principle, when a plane wave is incident on a Fresnel lens, each point in a transparent zone acts as a secondary source, which emits a spherical wave. If the zones are so designed that radiation from all the transparent zones arrives in phase within $\pm\pi/2$ range at the focal point F, there will be constructive interference. This requires that the distance from F to the edge of the successive zones be integral multiples of half wavelength, i. e.,

$$R_n = f + \frac{n\lambda}{2} \tag{2.1}$$

where R_n is the distance from the focal point to the nth zone boundary, f is the focal length, and λ is the wavelength. The radius of the nth edge is given by

$$\rho_n = \frac{n\lambda}{2}\sqrt{1+\frac{4f}{n\lambda}}. \tag{2.2}$$

The area covered by the nth zone is given by

$$A_n = \pi\lambda(f+\frac{\lambda}{4}) + \frac{n\pi\lambda^2}{2}. \tag{2.3}$$

It is interesting to note that the area covered by each zone increases linearly with the associated index number n. The ratio of the second term to the first term in Eq. (2.3) is given by

$$\frac{n\lambda}{2(f+\frac{\lambda}{4})}.$$

For a practical zoneplate antenna with reasonable focal length to aperture diameter ratio, however, the aperture normally covers only a few half-wave zones whereas the focal length is in the tens of wavelengths. Therefore, the second term in Eq. (2.3) can be neglected and all the zones can be regarded as having approximately the same area.

2.2 Elliptical Zoneplate

Although the circular zoneplate is simple to fabricate, it has two main disadvantages when used as an antenna. First, since the main radiation beam is perpendicular to the plate, orienting it in the direction of the signal arrival may make it impossible to flush mount the plate on a building or a vehicle; second, the feed blockage inevitably degrades the antenna performance of the zoneplate reflector. A natural solution to these problems is to use the non-blocking offset configuration. An offset zoneplate consists of elliptical zones instead of circular ones and the direction of the maximum radiation and the feed axis form the same angle with the normal of the plate [10]. As with its circular counterpart, the offset zoneplate can have various versions, such as the simple zoneplate [11], the phase reversal zoneplate reflector [10] and the phase correcting zoneplate [15] etc.. In the following, equations which define the zone boundaries of an offset zoneplate are derived. Compared with the one given by the authors in [10], the following derivation provides a deeper insight into the operation of a zoneplate.

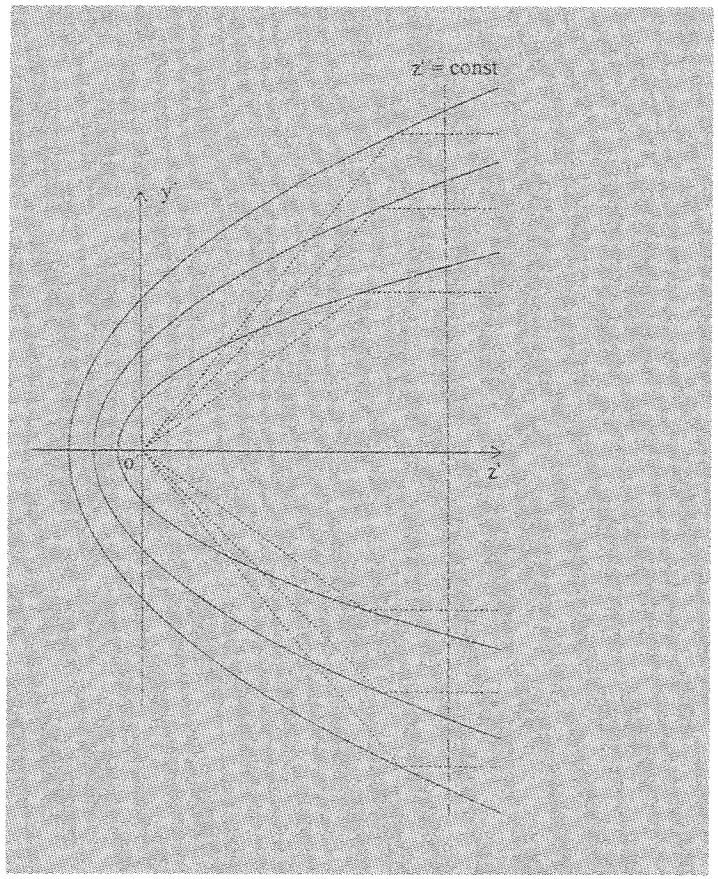

Fig. 2.2 A set of confocal paraboloids cut by a plane perpendicular to the axis.

The basic requirement on the half-wave zone boundaries is that rays originating from the focal point and diffracted at different zone boundaries in the direction of the maximum radiation have $n\lambda/2$ (n = 1, 2, ...) pathlength difference. Given a focal point F and the direction of maximum radiation z', one can form a set of Cartesian coordinates (x', y', z') with their origin located at $O' = F$ and the z' axis in the z' direction (see Fig. 2.2). Then, the following equation gives a set of confocal and coaxial paraboloids of revolution:

$$x'^2 + y'^2 = 4 f_n (z' + f_n) \tag{2.4}$$

where f_n, the focal length of the n'th paraboloid, is given by

$$f_n = n\lambda / 4 \ . \tag{2.5}$$

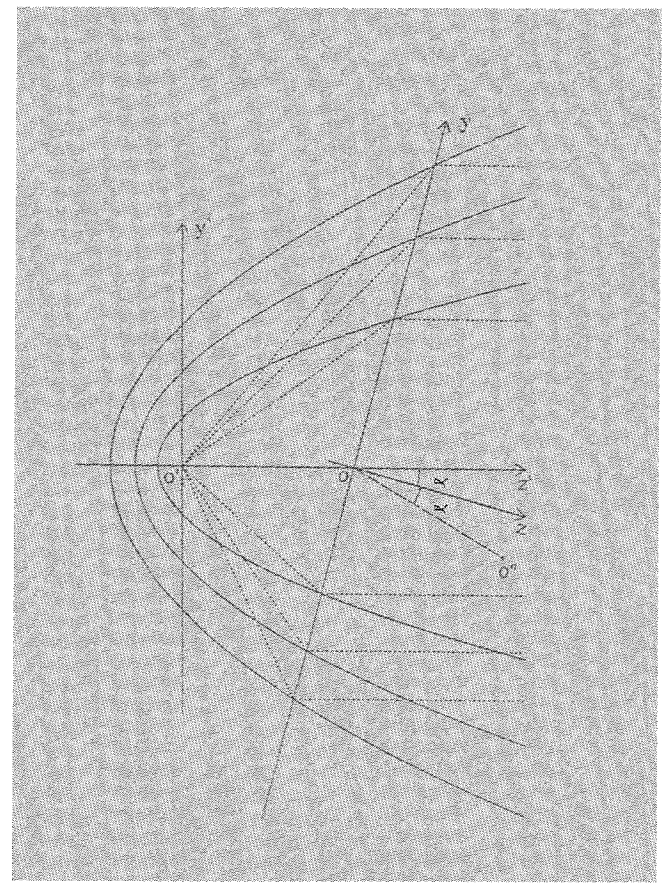

Fig. 2.3 A set of confocal paraboloids cut by a skew plane.

It is well known that a paraboloid converts a spherical wave originating from the focus into a plane wave propagating in its axial direction. On a plane given by z' = const, which is perpendicular to the axis

of the paraboloids, rays reflected from the n'th paraboloid experience $n\lambda/2$ + const pathlength (see Fig. 2.2). Consequently, the plane waves produced by two adjacent paraboloids have $\lambda/2$ pathlength difference, no matter where reflection occurs. To obtain the zone boundaries of an offset zoneplate, imagine cutting the paraboloids with a virtual plane which is penetrated by the z' axis at point O and whose normal vector forms an angle of α with the z' axis (see Fig. 2.3). This yields a set of lines of intersection. Since all the lines of intersection lie on the confocal paraboloids, rays in the z' direction originating from the focal point and diffracted from a given line of intersection experience the same pathlength, while those diffracted from adjacent lines of intersection have $\lambda/2$ pathlength difference (see Fig. 2.3). Therefore, the zone boundaries of an offset zoneplate located in the virtual cutting plane are simply given by these lines of intersection. As such, the procedure for determining the zone boundaries of an offset zoneplate becomes straightforward: Given a plane on which the zoneplate is to be placed, draw a piercing line in the desired direction of the maximum radiation. With this line as the z' axis and a point behind the plane as both the focal point and the origin of a Cartesian co-ordinate system, Eq. (2.4) produces a set of paraboloids of revolution. The lines of intersection between the paraboloids and the reference plane yield the zone boundaries, and the distance between the focal point and the piercing point, $|O'O|$ gives the focal length (see Fig. 2.3).

To obtain an explicit expression for the zone boundaries, a new set of Cartesian coordinates is introduced with the z axis in the direction normal to the zoneplate, and the y axis as the line of intersection between the reference plane and the $y'z'$ plane. The x, y and z axes form a set of right-handed Cartesian coordinates (see Fig. 2.3). On the $z = 0$ plane where the zoneplate is placed, one has

$$\begin{aligned} y' &= y\cos\alpha \\ x' &= x \\ z' &= y\sin\alpha + f \end{aligned} \tag{2.6}$$

where f is the focal length and α is the offset angle. Substituting Eq. (2.6) into Eq. (2.4) yields

$$x^2/b^2 + (y - c)^2/a^2 = 1 \tag{2.7}$$

where

$$a = b/\cos\alpha \tag{2.8.a}$$

$$b = [nf\lambda + (n\lambda/2)^2(1 + \tan^2\alpha)]^{1/2} \tag{2.8.b}$$

$$c = 2f_n\tan\alpha/\cos\alpha \tag{2.8.c}$$

Eq. (2.7) describes an ellipse with major axis a, minor axis b and centred at $(c, 0, 0)$. Its eccentricity is given by

$$e = \sin\alpha. \tag{2.9}$$

Eq. (2.9) indicates that all the elliptical zone boundaries of a zoneplate with given offset angle have the same eccentricity. For illustration, Fig. 2.4 gives the zonal patterns of offset zoneplates with different offset angles. It can be seen from Fig. 2.4 that with a fixed focal length f, increasing the offset angle α makes the zone widths in the upper half plane wider and those in the lower half plane narrower.

One advantage of the offset zoneplate antenna is that it can be flush mounted on a building or vehicle. With a given plane on which a zoneplate is to be fixed, the direction of the maximum radiation z' (such as the direction of a satellite) can be specified by two parameters, the polar angle α and the azimuth angle ϕ. α is the angle between z' and the plane normal, which is equal to the offset angle. ϕ is the angle between a horizontal line and the projection of z' on the plane. The zone boundaries of a conformal zoneplate are still given by Eq. (2.7) but with the major axis (y axis) rotated by an angle of $\pi/2 - \phi$, and the projection of the focal point on the plane, F', lies on the major axis of the ellipses (see Fig. 2.5).

Although the above analysis is based on the transmission zoneplate, all the equations apply equally to the reflection zoneplate. The only difference is that the focal point is located at F'' for the latter, which is the image position of F' about the zoneplate. For the reflection zoneplate, the feed axis forms the same angle with the plate normal as the z' axis does, so any two rays in the z' direction originating from F'' and diffracted from two different zone boundaries have the same pathlength difference as those from F' for the transmission zoneplate.

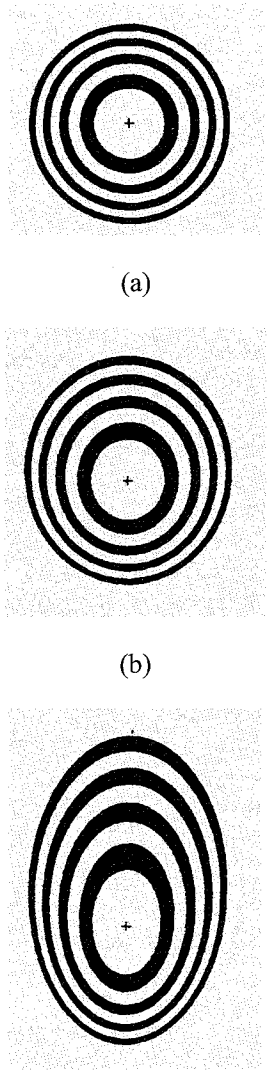

(a)

(b)

(c)

Fig. 2.4 Zonal patterns with different offset angles: (a) 0°, (b) 25° and (c) 50°.

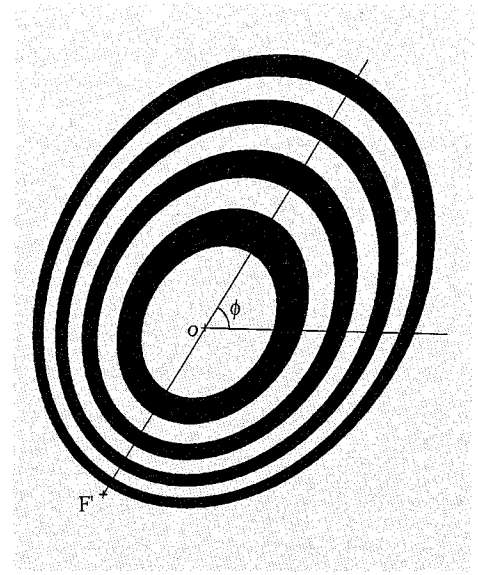

Fig. 2.5 A skew offset zoneplate.

It is interesting to study the projection of the elliptical zones in the direction of the maximum radiation (z' in Fig. 2.3). Substituting Eq. (2.6) into Eq. (2.7) gives

$$x'^2 + (y' - c')^2 = b^2 \tag{2.10}$$

where b is given by Eq. (2.8.b) and

$$c' = 2f_n \tan\alpha. \tag{2.11}$$

Eq. (2.10) describes a set of eccentric circles. Fig. 2.6 gives the zonal pattern of an offset zoneplate and its projection.

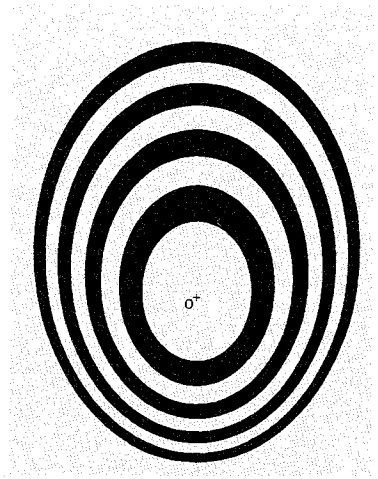

(a)

(b)

Fig. 2.6 An offset zoneplate (a) and its projection in the direction of maximum radiation (b).

2.3 Radiation of the Offset Fresnel Lens Antenna

A simple offset Fresnel antenna can be formed by using an elliptical zoneplate and a feed. For elliptical zoneplates, the asymmetrical geometry

brings in significant complexity to the analysis of the radiation field, so formulae for predicting the radiation pattern of the offset Fresnel lens antennas are derived in this section.

When illuminated by a feed horn placed at the focal point F (see Fig. 2.7), the radiation of the Fresnel lens is mainly attributed to the aperture field over the transparent zones. As a good approximation, the conductor around the Fresnel lens can be extended to infinity (see Fig. 2.8). Then, by virtue of Love's field-equivalence principle [20], the transparent zones can be represented by an equivalent magnetic current $\boldsymbol{J}_m$ on an infinite conducting plane without openings. With $\boldsymbol{E}_s$ as the tangential electric field on the lens surface, $\boldsymbol{J}_m$ is given by

$$\boldsymbol{J}_m = -\boldsymbol{n} \times \boldsymbol{E}_s \qquad (\textit{over transparent zones}) \qquad (2.12)$$

where $\boldsymbol{n}$, the unit vector normal to the lens surface, is given by

$$\boldsymbol{n} = \cos\alpha\, \boldsymbol{z} - \sin\alpha\, \boldsymbol{y} \qquad (2.13)$$

$\boldsymbol{J}_m$ vanishes over the regions covered with conductor (the reflection zones and the area outside the zoneplate). It should be noted that, for convenience, the direction of z axis is assumed to be aligned with that of the maximum radiation of the offset Fresnel lens in the following analysis.

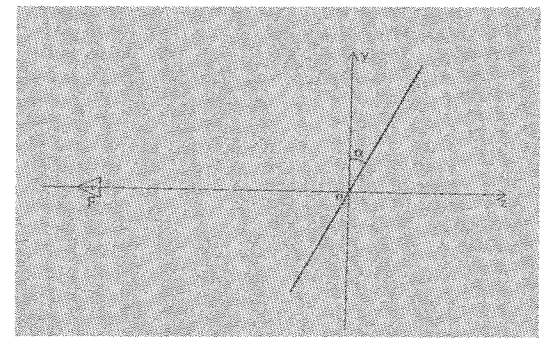

Fig. 2.7 Illustration of the co-ordinates for analysing a Fresnel lens.

Since the Fresnel lens is usually electrically large and the width of half-wave zones are normally greater or comparable with the operating wavelength, the following Kirchhoff approximation can be employed:

$$\boldsymbol{n}\times \boldsymbol{E}_s = \boldsymbol{n}\times \boldsymbol{E}_f \qquad (over\ transparent\ zones) \quad (2.14)$$

where $\boldsymbol{E}_f$ is the feed radiation field. Without loss of generality, it is assumed that the far field of the feed is of the following form

$$\boldsymbol{E}_f = \exp(-jkR)/R\ (\boldsymbol{\theta} E_\theta \sin\varphi + \boldsymbol{\phi} E_\phi \cos\varphi). \quad (2.15)$$

Substituting Eqs. (2.13) - (2.15) into Eq. (2.12) yields

$$\boldsymbol{J}_m = \boldsymbol{x}J_{mx} + \boldsymbol{y}J_{my} + \boldsymbol{z}J_{mz}$$

$$= exp(-jkR)/R\ \{\boldsymbol{x}[(\cos\alpha\cos\theta\sin\phi - \sin\alpha\sin\theta)\sin\phi\, E_\theta + \cos\alpha\cos^2\phi E_\phi]$$

$$+ \boldsymbol{y}\cos\alpha\sin\varphi\cos\phi[-\cos\theta E_\theta + E_\phi] + \boldsymbol{z}\sin\alpha\sin\varphi\cos\phi[-\cos\theta E_\theta + E_\phi]\} \quad (2.16)$$

where the spherical coordinates (R, θ, φ) are related with the Cartesian coordinates (x, y, z) through the following equations:

$$R = [x^2 + y^2 + (f + y\tan\alpha)^2]^{1/2} \quad (2.17.a)$$

$$\theta = \tan^{-1}[(x^2 + y^2)^{1/2}/(f + y\tan\alpha)] \quad (2.17.b)$$

$$\varphi = \tan^{-1}(y/x). \quad (2.17.c)$$

Eq. (2.16) shows that

$$J_{mz} = \tan\alpha J_{my}. \quad (2.18)$$

By virtue of a magnetic-type vector potential [20], the radiation field of the magnetic current can be expressed as

$$\boldsymbol{E} = jk/(2\pi r\cos\alpha)\exp(-jkr)\int_S \{J_{mx}(\zeta\sin\psi + \psi\cos\zeta\cos\psi)$$

$$- J_{my}[\zeta\cos\psi + \psi[\tan\alpha\sin\zeta - \cos\zeta\sin\psi)]\}$$

$$\exp\{jk[x\sin\zeta\cos\psi + y(\sin\zeta\sin\psi + \tan\alpha\cos\zeta)]\}dxdy \quad (2.19)$$

where (r, ζ, ψ) are the conventional spherical co-ordinates corresponding to the Cartesian co-ordinates (x, y, z).

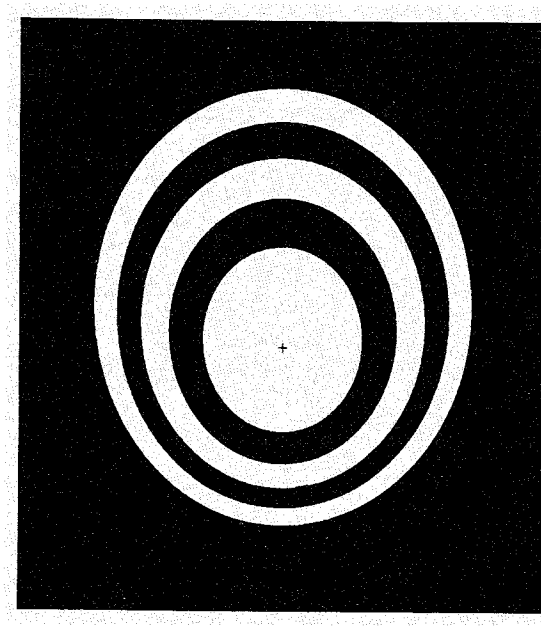

Fig. 2.8 Theoretical model of an offset Fresnel zone lens.

According to Ludwig's definition three [21], the co-polarised and the cross-polarised unit vectors are given respectively by

$$\boldsymbol{e}_1 = (\zeta\sin\psi + \psi\cos\psi) \quad (2.20.a)$$

$$\boldsymbol{e}_2 = (\zeta\cos\psi - \psi\sin\psi). \quad (2.20.b)$$

The scalar product of Eq. (2.19) with $\boldsymbol{e}_1$ and $\boldsymbol{e}_2$ respectively yields the co- and cross-polarised radiation fields of the Fresnel lens antenna:

$$E_{co} = jk/(2\pi r\cos\alpha)\exp(-jkr) \int_S \{J_{mx}(\sin^2\psi + \cos\zeta\cos^2\psi) - J_{my}\cos\psi[\sin\psi(1-\cos\zeta) + \tan\alpha\sin\zeta]\} \exp\{jk[x\sin\zeta\cos\psi + y(\sin\zeta\sin\psi + \tan\alpha\cos\zeta)]\}dxdy \quad (2.21.a)$$

$$E_{cross} = jk/(2\pi r\cos\alpha)\exp(-jkr) \int_S \{J_{mx}\cos\psi\sin\psi(1-\cos\zeta) - J_{my}[(\cos^2\psi + \cos\zeta\sin^2\psi) - \tan\alpha\sin\zeta\sin\psi]\} \exp\{jk[x\sin\zeta\cos\psi + y(\sin\zeta\sin\psi + \tan\alpha\cos\zeta)]\}dxdy \quad (2.21.b)$$

Eq. (2.21) shows that the x-component of the magnetic current, which corresponds to the y-component of the aperture electric field, has no contribution to the cross-polarised field in the E- and H- planes; whilst the y-component of the magnetic current, which corresponds to the x-component of the aperture electric field, has no contribution to the co-polarised field in the E-plane. When the aperture field has a pure linear polarisation in the y-direction, one obtains

$$\boldsymbol{J}_m = \boldsymbol{x}\, f(\theta,\phi)(\cos\alpha\cos\theta - \sin\alpha\sin\theta\sin\varphi)\exp(-jkR)/R. \quad (2.22)$$

and Eq. (2.21) simplifies to

$$E_{co} = jk/(2\pi r\cos\alpha)\exp(-jkr)(\sin^2\psi + \cos\zeta\cos^2\psi) \int_S \{J_{mx}\exp\{jk[x\sin\zeta\cos\psi + y(\sin\zeta\sin\psi + \tan\alpha\cos\zeta)]\}dxdy \quad (2.23.a)$$

$$E_{cross} = 2jk/(\pi r\cos\alpha)\exp(-jkr)\sin\psi\cos\psi(1-\cos\zeta) \int_S \{J_{mx}\exp\{jk[x\sin\zeta\cos\psi + y(\sin\zeta\sin\psi + \tan\alpha\cos\zeta)]\}dxdy. \quad (2.23.b)$$

Eq. (2.23) represents a far field without cross-polarisation in the E- and the H- planes. According to Eq. (2.16), it can be produced with a feed radiation pattern of the following type:

$$E_\theta = f(\theta,\phi) \quad (2.24.a)$$

$$E_\phi = f(\theta,\phi)\cos\theta \quad (2.24.b)$$

It is noted that owing to the flatness of the Fresnel lens, its optimal feed radiation pattern given by Eq. (2.24) is different from that for the conventional parabolic reflector by a factor of cosθ [20]. However, it should be pointed out that this conclusion is based on the Kirchhoff approximation given by Eq. (2.14). For a practical Fresnel lens antenna, the scattering from the edges of the conducting zones inevitably produces an aperture field with cross-polarisation, thus giving rise to a cross-polarised radiation field.

2.4 Evaluation of the Integral

Section 2.3 shows that, to obtain the radiation pattern of an offset Fresnel lens, it is required to evaluate the following two dimensional integration:

$$I(\zeta,\psi) = \int_S J_{mi}(x,y)\exp[j(u(\zeta,\psi)x + v(\zeta,\psi)y)]dxdy \quad (2.25)$$

where J_{mi} represents the x-component or the y-component of the magnetic current, and the spatial spectra $u(\zeta,\psi)$ and $v(\zeta,\psi)$ are given by

$$u(\zeta,\psi) = k\sin\zeta\cos\psi \quad (2.26.a)$$

$$v(\zeta,\psi) = k(\sin\zeta\sin\psi + \tan\alpha\cos\zeta). \quad (2.26.b)$$

It is seen that the offset configuration introduces an oblique factor $\exp(jk\tan\alpha\cos\zeta)$, which makes the relationship between the spatial spectra and the observation angle different from that for the symmetrical configuration [14, 22]. If the xy plane is chosen as the plane of the lens, the oblique factor will disappear, but the direction of the maximum radiation will form an angle α with the z-axis, and the definitions of the co- and cross-polarisation, as well as the expression of the feed field, will become more complicated.

Although the integration in Eq. (2.25) appears as a Fourier type and can be efficiently evaluated by using the fast Fourier transform technique (FFT) [23], it is not straightforward to calculate the plane-cut patterns except for the *E*-plane one. With $\psi = 0$ for *H*-plane, for example, Eq. (2.26) describes a curve instead of a straight line in the spectral plane, while the FFT gives only a discrete set of spectra on the rectangular grid. To tackle the problem, two approaches are introduced in the following.

The first approach is the one used for analysing offset parabolic reflector antennas [23, 24]. For convenience, we rearrange Eq. (2.25) as

$$I(\zeta,\psi) = \exp(-jvy_0) \int_S J_{mi}(x,y)\exp[j(ux + vy)]dxdy \tag{2.27}$$

where

$$y_0 = N\lambda\tan\alpha/2 \tag{2.28}$$

with N as the number of transparent and opaque half-wave zones in the Fresnel lens. The domain of integration in Eq. (2.27) is a circle centred at (0,0,0) with radius R_p given by

$$R_p = [Nf\lambda + (N\lambda/2)^2(1 + \tan^2\alpha)]^{1/2} . \tag{2.29}$$

Then, one can extend the domain of integration into a square with side length D and expand the magnetic current $J_{mx}(x,y)$ as the following finite Fourier series:

$$J_{mi}(x,y) = \sum_{-Q}^{Q-1}\sum_{-Q}^{Q-1} C_{qp}\exp[-j\omega(qx+ p y)] \tag{2.30}$$

where the upper and lower limits are chosen differently for convenience of implementing the FFT and

$$\omega = 2\pi/D \tag{2.31.a}$$

$$C_{qp} = \int_S J_{mi}(x,y)\exp[j\omega(qx + py)]\, dxdy. \tag{2.31.b}$$

Substituting Eq. (2.30) into Eq. (2.27) produces

$$I(\zeta,\psi) = \exp(-jvy_0)\sum_{-Q}^{Q-1}\sum_{-Q}^{Q-1} C_{qp}\frac{\sin[(u - qa)D/2]}{[(u-q\omega)D/2]}\frac{\sin[(v - pa)D/2]}{[(v-p\omega)D/2]} \tag{2.32}$$

Eq. (2.32) can be calculated at any given point (ζ,ψ) and the coefficients C_{qp} can be evaluated efficiently by using the FFT [24]. When only the gain of the antenna is concerned, one has

$$I(0,0) = \exp(-jky_0\tan\alpha)C_{00}. \tag{2.33}$$

The second approach is to obtain a discrete set of spectra by evaluating the integration in Eq. (2.31.b) with the FFT algorithm first. Then, the discrete spectra are used to produce a continuous spectral function by using the sub-domain interpolations such as the cubic spline interpolation and the bivariate interpolation. Mathematically, this gives

$$I(\zeta,\psi) = \exp(-jvy_0)\sum_{-Q}^{Q+1}\sum_{-Q}^{Q+1} C_{pq}\chi(u-p\omega, v-q\omega) \tag{2.34}$$

where $\chi(u-p\omega,v-q\omega)$ is the sub-domain basis function centred at $(p\omega,q\omega)$. Since the phase of C_{pq} changes rapidly with p and q, however, it was found that Eq. (2.34) failed to give stable results. Therefore, an interpolation of the magnitude is employed instead as follows

$$|I(\zeta,\psi)| = \sum_{-Q}^{Q+1}\sum_{-Q}^{Q+1}|C_{pq}|\chi(u-p\omega, v-q\omega) \tag{2.35}$$

When Eq. (2.35) is used, the second approach produces antenna patterns very close to the ones obtained with Eq. (2.32).

Comparing Eq. (2.32) with Eq. (2.35), it is seen that the first approach is equivalent to approximating a continuous spectrum with all-domain basis functions. For a given observation angle, a double summation which involves a large number of sin$x$/x operation is required. This is very time-consuming for electrically large lenses. As a sub-domain interpolation technique, the second approach requires only a few adjacent discrete spectra

for a given observation angle. Therefore, the CPU time used by the second approach is much less than that by the first one. It is suggested, therefore, that the first approach be used when both the amplitude and the phase patterns are of interest, while the second be used when only the amplitude patterns are of interest. In the next section, the second approach with bivariate basis functions is employed to predict the radiation patterns of offset Fresnel lenses.

2.5. Numerical and Experimental Results

In order to investigate the radiation performance of the offset Fresnel lens antenna, a pyramidal horn was used as the feed. The aperture field of the feed horn is assumed to be an expanded waveguide mode with a quadratic phase error [25, 26]. Using both the equivalent electric current and the equivalent magnetic current [20], the radiation field is obtained as

$$E_\theta(\theta,\phi) = E_\phi(\theta,\phi)$$

$$= jk(1+\cos\theta)\, P_y(\theta,\varphi)/4\pi \qquad (2.36)$$

where

$$P_y = E_0 \int_{-A/2}^{A/2}\int_{-B/2}^{B/2} \cos(\pi x/A)\exp\{j[-(\pi/\lambda)(x^2/R_1 + y^2/R_2) + k(\mu x + \gamma y)]\}dxdy \qquad (2.37)$$

with

$$\mu = k\sin\theta\cos\phi \qquad (2.38.a)$$

$$\gamma = k\sin\theta\sin\phi. \qquad (2.38.b)$$

In Eq. (2.37), A and B are the width and height of the horn aperture, and R_1 and R_2 are the distances from the aperture to the two virtual apex lines respectively [25, 26]. Varying A and B changes the edge illumination level of the offset Fresnel lens.

As shown in section 2.4, the projection of an offset Fresnel lens boundary on the xy plane produces a circle with diameter equal to the lens

width $2R_p$. To investigate the performance of the offset configuration, it is appropriate to have the lens width fixed [27]. Fig. 2.9 shows the normalised E-plane and H-plane patterns of an offset Fresnel lens with different offset angles. The lens comprises four transparent half-wave zones with R_p fixed at 0.3m, and the operating frequency is chosen at 10.39GHz. The feed parameters are for a pyramidal horn made by the Mid-Century Microwavegear Ltd. with an aperture of 4.1cm by 2.8cm. Since the Kirchhoff approximation is suited mainly for near-in patterns, we restrict the observation angle in a range of (-50°, 50°). For the E-plane patterns, it is seen that when the offset angle is increased from 0° to 20° and 40°, the 3dB beamwidths remain almost constant, the skirts of the main beams become wider, and the sidelobe level is increased from -15.9dB, to -15.4dB and -14.8dB respectively. Less change is observed in the H-plane patterns. The antenna directivity is actually reduced by 0.1dB and 0.7dB respectively. Fig. 2.10 shows the cross-polarised patterns of the same lens antenna in the $\psi = 45°$ plane. It is observed that increasing the offset angle hardly changes the cross-polarisation level. Increasing the offset angle further leads to further reduction of the antenna directivity and further increase of the sidelobe level.

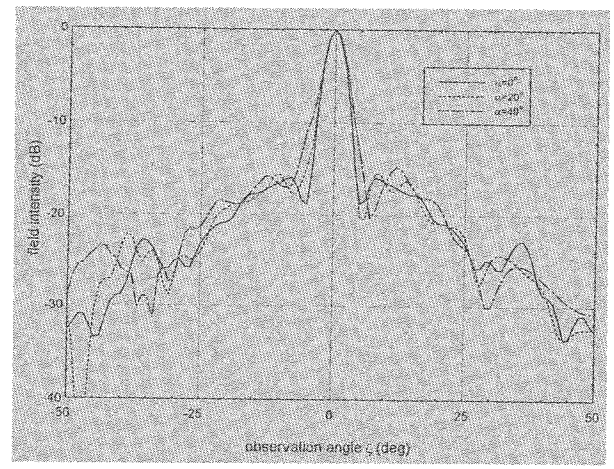

(*a*) *E-plane patterns.*

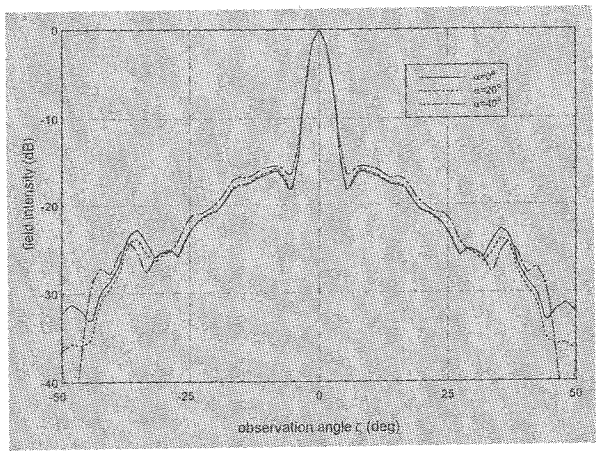

(*b*) *H-plane patterns.*

Fig. 2.9 Co-polarised patterns of a Fresnel lens with fixed width and different offset angles.

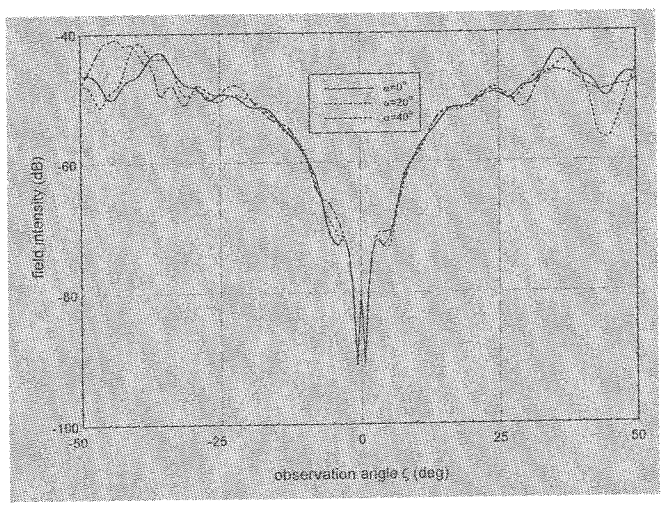

Fig. 2.10 Cross-polarised patterns of the Fresnel lens.

For conventional lenses and reflectors, decreasing the edge illumination level effectively reduces the sidelobe level. However, this is not

necessarily true for the Fresnel lens antenna. Numerical results show that increasing the dimension of the feed does not change the sidelobe level much. This is because in a Fresnel lens antenna spherical phase errors in a range of $\pm\pi/2$ exist over all the transparent half-wave zones. These severe phase errors dominate the sidelobe level of the antenna. Besides, since the scattering from the edges of the conducting zones has not been considered in the theoretical model given in section 2.3, it is expected that the sidelobe level of a practical Fresnel lens will be higher than predicted. The simple (not phase corrected) Fresnel lens should, therefore, only be used when the interference through sidelobes is not a major concern.

As an experimental prototype, an offset Fresnel lens comprising three transparent half-wave zones with $f = 0.14$m, offset angle $\alpha = 20^\circ$ and operating at 10.39GHz was designed. The conducting pattern was printed on a 2mm dielectric substrate with relative dielectric constant $\varepsilon_r = 2.1$. The same pyramidal horn used in the numerical analysis was employed as the feed. Fig. 2.11.a shows the E-plane patterns of the antenna. For the co-polarisation, the theoretical pattern has a wider main beam, but lower sidelobes. It follows the trend of the experimental pattern as far as 50° away from the direction of the maximum radiation. Theoretically, the cross-polarisation in the E-plane is below -60dB, while it is shown in Fig. 2.11.a that the measured cross-polarisation was about -29dB. Fig. 2.11.b shows the corresponding results in the H-plane. For the co-polarisation, it is seen that the experimental pattern has about the same sidelobe level as that of the predicted one, but slightly wider main beam. The two far-out patterns have similar profiles, but are less close than the E-plane patterns. The predicted cross-polarisation in the H-plane is below -45dB, while it is shown in Fig. 2.11.b that the measured cross-polarisation was about -22dB. One reason for the discrepancy between the theoretical and experimental results is that the lens width is only 12.4 wavelengths and the focal length is only 4.8 wavelengths so there is a strong multiple scattering between different conducting zones, and the lens and feed, which is not considered in the theoretical model. The other reason is the feed alignment accuracy. Better agreement is expected with a larger Fresnel lens and better alignment mechanism. Furthermore, the higher cross-polarisation level in the H-plane is attributed to the stronger edge scattering in this plane.

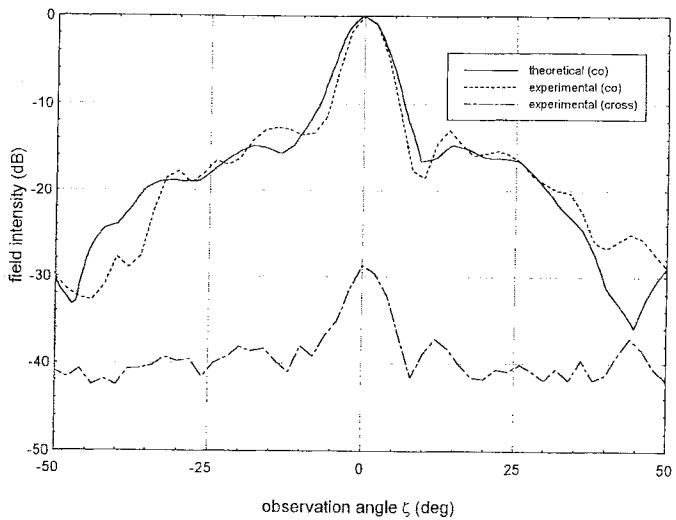

(*a*) *E-plane patterns.*

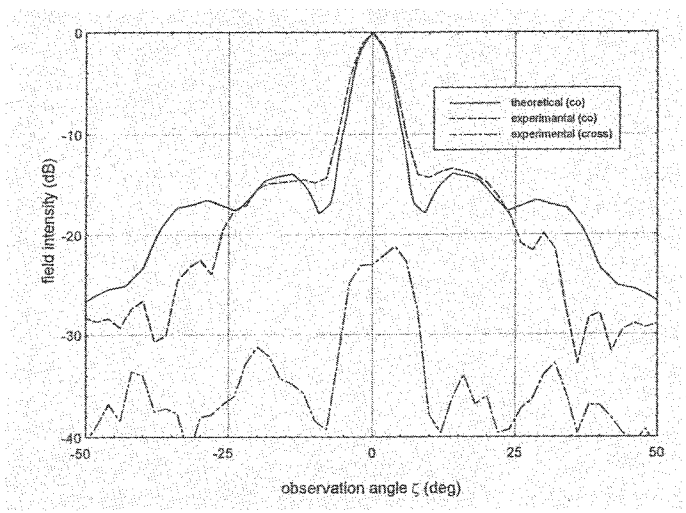

(*b*) *H-plane patterns.*

Fig. 2.11 Experimental patterns of the offset Fresnel zone lens in comparison with theoretical predictions.

2.6 Conclusions

The geometrical characteristic of offset Fresnel zoneplate antennas has been studied. It is shown that the elliptical zone boundaries of an offset Fresnel zoneplate are given by the lines of intersection between a set of confocal paraboloids of revolution and a cutting plane, where the axis of the paraboloids is in the direction of the maximum radiation (or the signal arrival) and the zoneplate is located on the cutting plane. The angle between the paraboloidal axis and the plane normal gives the offset angle α. The paraboloidal axis, the major axis of the ellipses and the feed axis lie in one plane. The ellipses have the same eccentricity, $e = \sin\alpha$. The projection of these ellipses in the direction of the maximum radiation produces a set of eccentric circles.

Formulae for predicting the far-field pattern of offset Fresnel lens antennas have been derived and the radiation performance of the offset Fresnel lens antennas including sidelobe and cross-polarisation levels is investigated. Two approaches to evaluating the radiation integral efficiently are introduced. It is shown that with a fixed lens width (or a fixed projected area in the direction of the maximum radiation), the H-plane and cross polarisation patterns remain almost constant with changing offset angle. There is no significant deterioration of gain or E-plane sidelobe level if the offset angle is not very large (say less than 40°). Since the sidelobe level of the Fresnel lens is not sensitive to the edge illumination level, its feed should be designed to achieve maximum efficiency.

Chapter 3 Phase Correcting Fresnel Zoneplates

Although the simple Fresnel zoneplate antenna with alternative reflective and transparent half-wave zones is easy to fabricate, its efficiency is too low for many practical applications. There are two factors that cause low efficiency to the simple Fresnel zoneplate. First, from a reception point of view, half of the energy intercepted by the aperture of a Fresnel zoneplate antenna is completely rejected. Second, the other half of the energy intercepted by the aperture is not efficiently focused into the feed, as the secondary radiation from a transparent half-wave zone does not add up completely in phase at the focal point. The first problem can be easily solved for reflection zoneplates, by placing a conducting plate at a quarter distance behind the simple zoneplate to form a phase reversal zoneplate reflector [4, 6]. The solution to the second problem is to apply phase correction techniques to the zoneplate surface [5]. Since a continuous phase compensation is very difficult to achieve, two sub-optimal phase correction techniques have been used for high efficiency zoneplate antennas, the subzone phase correction and the optimal discrete phase correction [5, 14, 19]. This chapter is concerned with the first technique and the second one, which is to employ an array of discrete phase shifters, will be dealt with later in chapter 6.

It is well known that the efficiency of a reflector or lens antenna can be expressed as

$$\eta = \eta_f \eta_p \eta_\psi \tag{3.1}$$

where η_f is the efficiency of the feed, η_p is the phase efficiency and η_ψ represents the product of the illumination efficiency, the spillover efficiency and the polarisation efficiency [20, 29]. The phase correction technique is aimed to increase the phase efficiency of the zoneplate antenna. The essence of the subzone phase correction technique is to divide each full wave zone

into several finer subzones and allocate an appropriate constant phase shifter in each of them, thus achieving a good approximation to the ideal continuous phase correcting function. In this chapter, a theory of subzone phase correcting techniques based on the focal field study is fully developed in sections 3.1 to 3.3 [13]. This is followed by some theoretical study on the optimisation of η_ψ in section 3.4 [14, 31]. Section 3.5 presents an investigation of the sidelobe performance of subzone phase correcting zoneplates. Sections 3.6 and 3.7 describe the design and experimental results of circular and offset multilayer phase correcting Fresnel zoneplate antennas.

3.1 Focal Field Expression

The phase correction technique attempts to maximise the field intensity at the focal point. Assume a plane wave is normally incident on a circular zoneplate, the field at the focal point can be well predicted by the Kirchhoff scalar diffraction integral [14, 28]:

$$\Psi = \frac{jk}{2}\int_0^{\rho_N} \exp\{j[\Phi(\rho) - kR]\}(1+\frac{f}{R})\frac{\rho}{R}d\rho \tag{3.1}$$

where f is the focal length, ρ_N is the radius of the zoneplate, $\Phi(\rho)$ is a phase correcting function, $k = \frac{2\pi}{\lambda}$ is the wave number and $R = (f^2 + \rho^2)^{1/2}$ represents the distance between the focal point and a point at the plate surface with radius ρ (see Fig. 3.1). Dividing the integration range in Eq. (3.1) into a series of full wave zones yields

$$\Psi = \frac{jk}{2}\sum_{n=1}^{N}\int_{\rho_{n-1}}^{\rho_n} \exp\{j[\Phi(\rho) - kR]\}(1+\frac{f}{R})\frac{\rho}{R}d\rho \tag{3.2}$$

where ρ_n satisfies the following zone boundary equation :

$$(f^2 + \rho_n^2)^{1/2} = f + n\lambda \qquad (n = 0,1,\ldots,N). \tag{3.3}$$

In the range of $\rho_{n-1} < \rho < \rho_n$, R changes from $f + (n-1)\lambda$ to $f + n\lambda$. Therefore, the magnitude factor $1 + f/R$ in Eq. (3.2) can be expressed as

$$1+\frac{f}{R} = 1+\frac{f}{f+(n-\frac{1}{2})\lambda}+\Delta,$$

where

$$\Delta = \frac{-t\lambda f}{[f+(n-1/2+t)\lambda][f+(n-1/2)\lambda]} \qquad -1/2 \le t \le 1/2.$$

Since a zoneplate is normally placed in the radiation zone of its feed, it can be assumed that $f >> \lambda$ so one can neglect the small term Δ and replace $1 + f/R$ with $1 + f/[f + (n-1/2)\lambda]$. The relative error of this approximation decreases when f/λ increases and is less than 2.5% for a zoneplate with $f = 10\lambda$. This yields

$$\Psi \approx \frac{jk}{2}\sum_{n=1}^{N}[1+\frac{f}{f+(n-1/2)\lambda}]\int_{\rho_{n-1}}^{\rho_n}\exp\{j[\Phi(\rho)-kR]\}\frac{\rho}{R}d\rho \quad (3.4).$$

To obtain a closed form expression of the focal field, let

$$\theta = k\{(f^2+\rho^2)^{\frac{1}{2}} - [f+(n-1)\lambda]\} \qquad (\rho_{n-1} \le \rho \le \rho_n) \quad (3.5)$$

Substituting Eq. (3.5) into Eq. (3.4) yields

$$\Psi \approx \frac{j}{2}\exp(-jkf)\sum_{n=1}^{N}[1+\frac{f}{f+(n-1/2)\lambda}]\int_{0}^{2\pi}\exp\{j[\Phi'(\theta)-\theta]\}d\theta \quad (3.6)$$

where $\Phi'(\theta) = \Phi[\rho(\theta)]$. Eq. (3.6) shows that the contributions from different full wave zones with the same phase correcting function $\Phi'(\theta)$ differ only with a multiplier $1 + f/[f + (n-1/2)\lambda]$. The physical interpretation is as follows. When a plane wave is incident on a full wave zone, its contribution to the focal field is proportional to the area

$\pi(\rho_n^2 - \rho_{n-1}^2)$ and inversely proportional to its mean distance to the focal point $f + (n-1/2)\lambda$, and the product of these two factors gives a constant which is independent of the location of the full wave zone. The multiplier $1 + f/[f + (n-1/2)\lambda]$ is due to the variation of the oblique angle ϕ over the zoneplate surface (see Fig. 3.1).

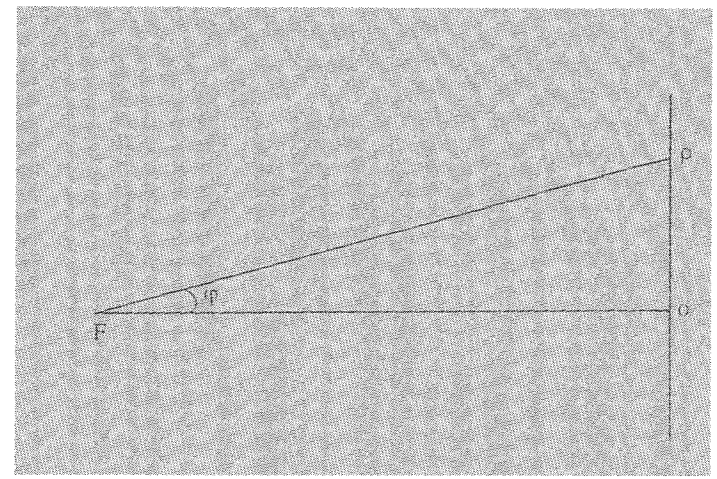

Fig. 3.1 Illustration of the co-ordinates.

When $\Phi'(\theta) = \theta$, the zoneplate is ideally phase corrected and Eq. (3.6) gives the maximum field intensity at the focal point:

$$|\Psi|_{\max} \approx \pi\sum_{n=1}^{N}[1+\frac{f}{f+(n-1/2)\lambda}] \quad (3.7)$$

The corresponding ideal phase correcting function in the ρ domain is given by

$$\Phi_{opt}(\rho) = k\{(f^2+\rho^2)^{\frac{1}{2}} - [f+(n-1)\lambda]\} \qquad (\rho_{n-1} \le \rho \le \rho_n).$$

3.2 Subzone Phase Correction

The subzone phase correction technique employs M discrete phase shifters in each full wave zone in order to realise a stepwise phase correcting function to approximate $\Phi_{opt}(\rho)$. Let θ_{nm} represent the subzone boundary in θ domain and Φ'_{nm} represent the constant phase shift in the subzone defined by $\theta_{n(m-1)} < \theta < \theta_{nm}$ $(m = 1,2,\ldots, M;\ \ n = 1,2,\ldots, N)$ respectively, Eq. (3.6) produces

$$\Psi \approx j\exp(-jkf)\sum_{n=1}^{N}[1+\frac{f}{f+(n-1/2)\lambda}]\sum_{m=1}^{M}\exp[j(\Phi'_{nm}-\frac{\theta_{n(m-1)}+\theta_{nm}}{2})]\cdot \sin(\frac{\theta_{nm}-\theta_{n(m-1)}}{2}) \tag{3.8}$$

Maximising $|\Psi|$, the field intensity at the focal point, yields

$$\theta_{nm} = \frac{2\pi m}{M} \tag{3.9.a}$$

$$\Phi'_{nm} = \frac{2\pi m}{M} + \alpha \tag{3.9.b}$$

$$(m = 1,2,\ldots, M)$$

where the constant α can take any arbitrary value, but it must be the same for different full wave zones. This means that for a given M, the number of different phase shifters, the optimum choice of phase shift values is the equally spaced set where the phase difference between each value and the adjacent one is $2\pi/M$. For a zoneplate with the optimum subzone boundaries and the corresponding phase shifts given by Eq. (3.9), the contributions from different subzones have the same magnitude and add in phase. Using Eq. (3.5), Eq. (3.9.a) gives ρ_{nm}, the outer radius of the m'th subzone in the n'th full wave zone:

$$(f^2+\rho_{nm}^2)^{\frac{1}{2}} = f+[(n-1)+\frac{m}{M}]\lambda \quad (m=1,2,\ldots,M; n=1,2,\ldots,N) \tag{3.10}$$

Note that there are two requirements in Eq. (3.9). First, M subzones must be equally divided in θ domain. Second, the phase difference between two adjacent phase shifters must be $2\pi/M$. With the constant α in Eq. (3.9.b) as $-\pi/M$, this leads to zero mean error between the stepwise phase correcting function $\Phi'(\theta)$ and the ideal one $\Phi'_{opt}(\theta) = \theta$. However, since one can add an arbitrary constant to $\Phi'_{opt}(\theta)$, which is equivalent to changing the initial value of the ideal phase correcting function at the zoneplate centre, one can equally choose the initial value of $\Phi'(\theta)$ in the first subzone. This accounts for the arbitrary constant α in Eq. (3.9.b). For illustration, Fig. 3.2.a shows the ideal phase correction (dotted line) and its two equivalent quarter-wave approximations with different initial values (solid and dashed lines) for a zoneplate with $f = 20\lambda$, where ρ/λ is taken as the abscissa. Since the diffracted fields from subzones add on the basis of effective areas intercepted, $(\rho/\lambda)^2$ is a better choice of abscissa for averaging contributions. With $(\rho/\lambda)^2$ as abscissa, the ideal phase correcting function becomes almost linear and the subzone widths are almost equal, which is shown in Fig. 3.2.b.

Substituting Eq. (3.9) into Eq. (3.8) yields

$$\psi \approx j\pi\exp[-j(kf-\alpha-\pi/M)]\mathrm{sinc}(1/M)\sum_{n=1}^{N}\{1+f/[f+(n-1/2)\}] \tag{3.11}$$

where

$$\mathrm{sinc}(x) = \sin(\pi x)/(\pi x) \tag{3.12}$$

Comparing Eq. (3.11) with Eq. (3.7), one obtains the phase efficiency of a $1/M$-wave zoneplate antenna

$$\eta_p = \mathrm{sinc}^2(1/M) \tag{3.13}$$

Table 1 gives the phase efficiency of the phase correcting zoneplate with different numbers of subzones.

M	2	4	6	8
$\eta_p(\%)$	41	81	91	95

Table 1 Phase efficiency of the subzone phase correcting zoneplates

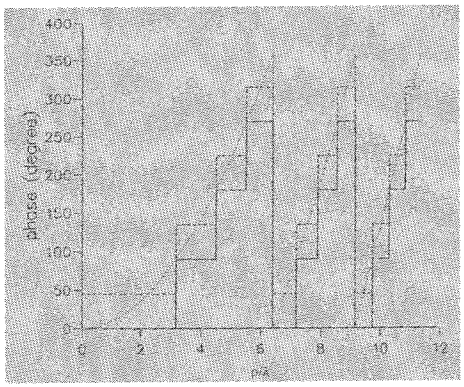

(a)

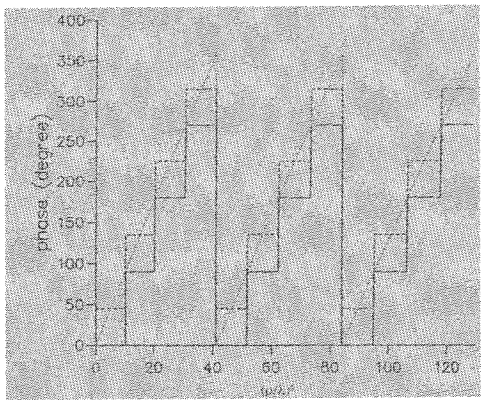

(b)

Fig. 3.2 The ideal phase correcting function and its quarter-wave approximations with ρ/λ (a) and $(\rho/\lambda)^2$ as abscissa, respectively.

3.3 Aperiodic Subzone Phase Correction

It can be shown from Eq. (3.3) that the width of a full wave zone decreases as the zone index n increases. As an illustration, Fig. 3.3 shows the widths of the outermost full wave zones for zoneplates with different f/D ratios and different number of full wave zones N, where D is the diameter of the zoneplate. It is observed that for a typical millimetre wave or microwave zoneplate with f/D around 0.8 and N around 4, the outermost full wave zone is about 2λ wide. Since most practical annular phase shifters can not be made arbitrarily narrow, it may not be possible to place as many phase shifters in the outer full wave zones as in the inner ones. Practically, it may be appropriate to employ the aperiodic subzone phase correction technique. The concept is to allocate more subzone phase shifters in the inner full wave zones and fewer in the outer ones. Consequently, the phase correcting function becomes aperiodic in θ domain. With an aperiodic phase correcting zoneplate, care must be taken to ensure that the contributions from different full wave zones add in phase.

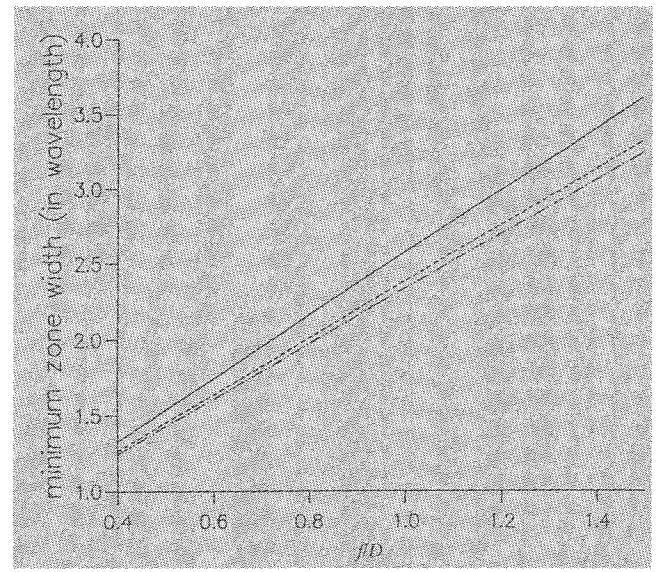

Fig. 3.3 Width of the outmost full-wave zones vs. f/D ratio. Solid line: N = 2; dot dashed line: N = 4; double dot dashed line: N = 6.

For an aperiodic subzone phase correcting zoneplate, the focal field intensity is given by

$$\psi = j\exp(-jkf)\sum_{n=1}^{M}\{1+f/[f+(n-1/2)\lambda\}. \sum_{m=1}^{M_n}\exp\{j[\Phi'_{mn}-(\theta_{n(m-1)}+\theta_m)/2]\}\sin[(\theta_{nm}-\theta_{n(m-1)})/2] \quad (3.14)$$

where M_n stands for the number of subzones in the n'th full wave zone. Maximising the focal field intensity produces

$$\theta_{nm} = 2\pi m/M_n \quad (3.15.a)$$

$$\Phi'_{nm} = (2m-1)\pi/M_n + \alpha \quad (3.15.b)$$

Compared with Eq. (3.9.b) for periodic phase correction, an extra phase compensation term $-\pi/M_n$ appears in Eq. (3.15.b). Its function is to make contributions from different full wave zones add in phase. Substituting Eq. (3.15) into Eq. (3.14) produces

$$y = j\pi\exp[-j(kf-\alpha)]\sum_{n=1}^{N}\{1+f/[f+(n-1/2)\lambda]\}\sin c(1/M_n) \quad (3.16)$$

The phase efficiency of the aperiodically phase corrected zoneplate is given by

$$\eta_p = \{\sum_{n=1}^{N}\{1+f/[f+(n-1/2)\lambda]\}\mathrm{sinc}(1/M_n)/\sum_{n=1}^{N}\{1+f/[f+(n-1/2)\lambda]\}\}^2 \quad (3.17)$$

Fig. 3.4 shows the optimal phase correcting function for the same zoneplate as in Fig. 3.2 with quarter-wave zones in the two inner full wave zones and half wave zones in the third one, where α is taken as $-\pi/2$. To understand the function of the phase compensation term, $(\rho/\lambda)^2$ is taken as the abscissa again and the ideal phase correcting function (dotted line) is assumed to start from $-\pi/2$ at the zoneplate centre. It is observed that the mean error between the ideal phase correcting function and the quarter-wave approximation (solid line) in the two inner full wave zones is almost zero.

For the half-wave approximation (solid line) used in the third full wave zone, this is only possible by moving the phase correcting function upward by $\pi/4$, which is the difference between $-\pi/4$ and $-\pi/2$. A practically important conclusion from Fig. 3.4 is that if the conventional phase reversal configuration is used in the outer full wave zones of a zoneplate to realise 0 and π phase shifts, the quarter-wave zone phase shifters in the inner full wave zones must take the following values: $-\pi/4$, $\pi/4$, $3\pi/4$ and $5\pi/4$. For comparison, Fig. 3.5 shows the same phase correcting functions as in Fig. 3.4 with ρ/λ as the abscissa.

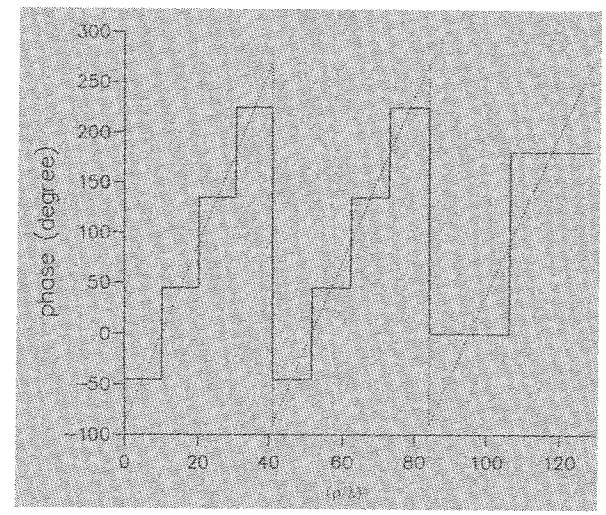

Fig. 3.4 The optimal phase correcting function for an aperiodic zoneplate.

3.4 Design of High Efficiency Zoneplate Antenna

The theory of high efficiency parabolic dishes has been well established [20]. For a zoneplate with the same *f/D* as that of a dish, however, the feed radiation field suffers more space attenuation at the edge, which is due to the flat nature of the zoneplate. On the other hand, the plate does not degrade the polarisation of the feed radiation field, providing that the edge diffraction is negligible. The optimum taper to obtain the maximum efficiency for a zoneplate must therefore be different from that of a dish.

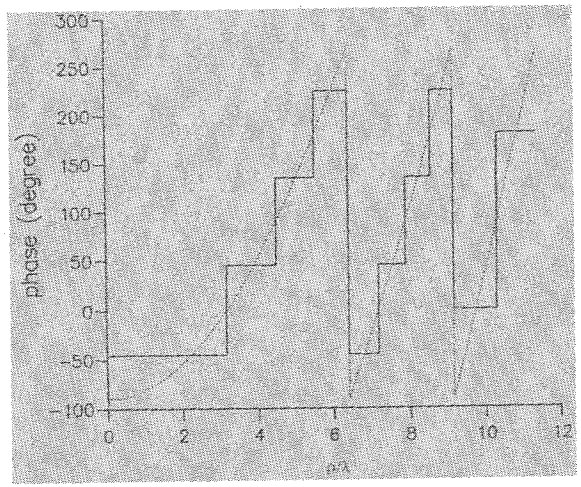

Fig. 3.5 The same phase correcting function as in Fig. 3.4 against ρ/λ.

For convenience, assume the feed radiation pattern is circularly symmetrical and polarised in the y direction:

$$\boldsymbol{E}_f(\theta,\phi,r) = \cos^p\theta\,(\boldsymbol{\theta}\sin\phi + \boldsymbol{\phi}\cos\theta\cos\phi)\exp(-jkr)/r \quad \theta \le \pi/2$$

$$= 0 \qquad \text{otherwise} \qquad (3.18)$$

where θ, φ and r are the conventional spherical co-ordinates, $\boldsymbol{\theta}$ and $\boldsymbol{\phi}$ are the unit vectors in the θ and ϕ directions and the index n is used to control the edge illumination level. Eq. (3.18) leads to the following spillover efficiency

$$\eta_s = \{(2p+3)[1 - \cos^{2p+1}(\Psi/2)] + (2p+1)[1 - \cos^{2p+3}(\Psi/2)]\}/[4(p+1)] \qquad (3.19)$$

where Ψ is the angle spanned by the zoneplate at the focal point. Under the geometrical optics assumption, the feed field given in Eq. (3.18) produces an aperture field without cross polarisation :

$$E_y(\rho) = \cos^{p+2}[\tan^{-1}(\rho/f)]\exp[-jk(f^2+\rho^2)^{1/2}]/f \qquad (3.20)$$

and the polarisation efficiency becomes unity. The illumination efficiency for a circularly symmetric aperture field is given by [20]

$$\eta_i = (8/D^2)\left(\int_\rho |E_y(\rho)|\rho d\rho\right)^2 \Big/ \int_\rho |E_y(\rho)|^2\rho d\rho \qquad (3.21).$$

Substituting Eq. (3.20) into Eq. (3.21) yields

$$\eta_i = 4(p+1)\alpha_p\cot^2(\Psi/2)/(1 - \cos^{2p+2}(\Psi/2)) \qquad (3.22)$$

with

$$\alpha_p = [\ln\cos(\Psi/2)]^2 \qquad p = 0$$

$$= \{[1 - \cos^p(\Psi/2)]/p\}^2 \qquad p > 0$$

The product of the spillover efficiency η_s and the illumination efficiency η_i is a function of Ψ and p. When f/D is kept constant, increasing p lowers the edge illumination level, enhances the spillover efficiency η_s but decreases the illumination efficiency η_i. For a zoneplate with given f/D, there is an optimum edge illumination level which yields the maximum $\eta_i\eta_s$. The optimum $\eta_i\eta_s$ and the optimum edge illumination level as a function of f/D are shown in Fig. 3.6 and Fig. 3.7. It is observed that when f/D is increased from 0.25 to 1.5, the optimum $\eta_i\eta_s$ increases from 62% to 81%, and the optimum edge illumination level of the feed decreases from -3.5dB to -10.4dB. Increasing the f/D ratio further leads to very little change. From this and Table 1, we conclude that the maximum efficiency of a quarter-wave zoneplate antenna is about 65% and that of a 1/6-wave zoneplate is about 74%.

It should be pointed out that for a practical feed and a Fresnel zoneplate, cross polarisation is usually inevitable and, with a given f/D ratio, the polarisation efficiency decreases when increasing the edge illumination level. Therefore, the optimum edge illumination level in a practical design must be lower than that given in Fig. 3.7. Since the feed blockage and the losses in the feed and the practical zoneplate have been ignored in the above analysis, the realisable antenna efficiencies of the sub-zone phase correcting zoneplate antennas are generally less than those predicted with the above theory.

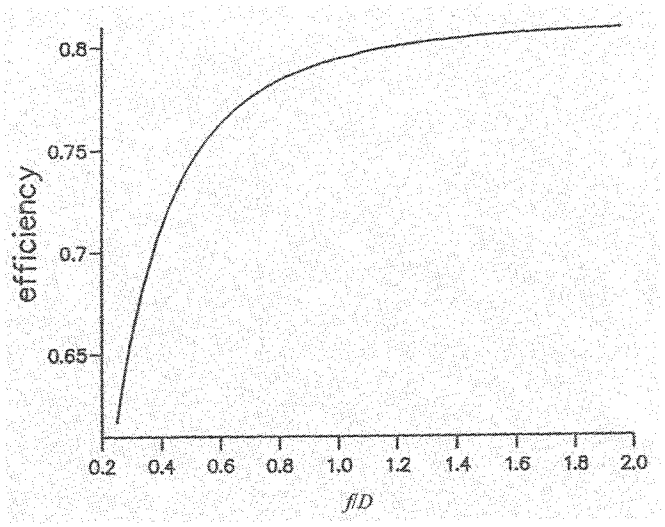

Fig. 3.6 Maximum $\eta_i\eta_s$ vs. f/D.

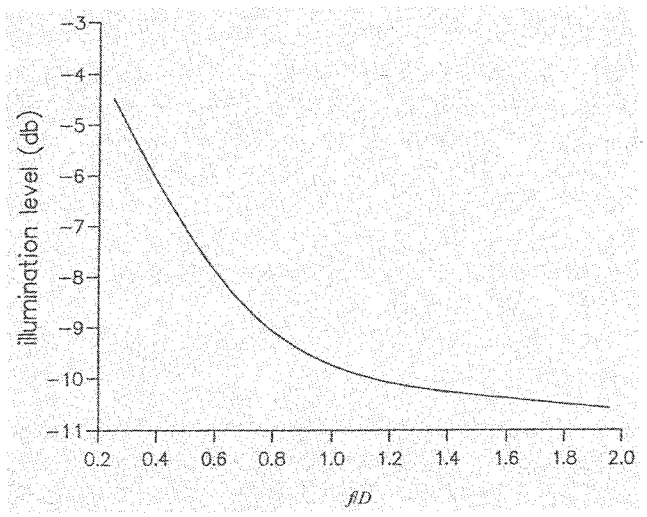

Fig. 3.7 Optimum edge illumination level vs. f/D.

3.5 Sidelobe Performance

Historically, attention has been paid mainly to the efficiency, bandwidth and focal fields of zoneplate antennas. Due to the numerous physical discontinuities existing over a Fresnel zoneplate surface, an accurate analysis of the radiation pattern is very computationally demanding. However, the close-in patterns can be well predicted with the Kirchhoff scalar diffraction integral [2, 5].

Generally speaking, the near-in radiation patterns of most phase correcting zoneplates can be well approximated by the following scalar integral [14, 31]:

$$F(\theta) = \int_{\rho} \exp[j\Phi(\rho)]E_y(\rho)\, J_0(k\rho\sin\theta)\, \rho d\rho \qquad (3.23)$$

where J_0 is the zeroth order Bessel function of the first kind and θ is the observation angle. Substituting Eq. (3.20) into Eq. (3.23) results in

$$F(\theta) = \int_{\rho} \exp[j\Phi(\rho)]\cos^{n+2}(\tan^{-1}(\rho/f)\exp[-jk(f^2+\rho^2)^{1/2}]J_0(k\rho\sin\theta)\rho\, d\rho/f \qquad (3.24)$$

Fig. 3.8 shows the radiation patterns of a zoneplate reflector with 4 full wave zones and diameter $D = 30\lambda$, and operating at 12GHz. An edge illumination level of -9.5dB was chosen to obtain the maximum antenna efficiency. It is seen that with $M = 2$ for the phase reversal zoneplate, the phase error in the aperture field produces a wide skirt in the radiation pattern and the envelope of sidelobes is quite flat. When M increases from 2 to 4 the sidelobe level is reduced from -21.8dB to -27dB. The difference between the first sidelobe level of the quarter-wave zone plate ($M = 4$) and that of the ideally phase corrected zoneplate ($M = \infty$) is only 0.5dB. The residual phase errors tend to fill the nulls in the radiation pattern and make the sidelobe envelope flat.

For conventional reflector antennas, lower edge illumination level always leads to lower sidelobes. To understand the effect of edge illumination level on the sidelobe performance of zoneplate antennas, Fig. 3.9 shows the radiation patterns of the same zoneplate with an edge

illumination level of -20dB. Compared with Fig. 3.8, it is seen that the low edge illumination does not affect the antenna sidelobes much for the phase reversal zoneplate, which is due to the severe residual phase error. Significant sidelobe reduction occurs for the quarter-wave zoneplate and the ideally phase corrected one, whose sidelobe levels are reduced to -31.4dB and -36.2dB respectively. In practice, the edge illumination level of a zoneplate is unlikely to be less than -20dB in order to retain reasonable antenna efficiency and various manufacturing inaccuracies are inevitable. Therefore, it is concluded that the phase correcting zoneplate is only suitable for moderately low sidelobe antennas.

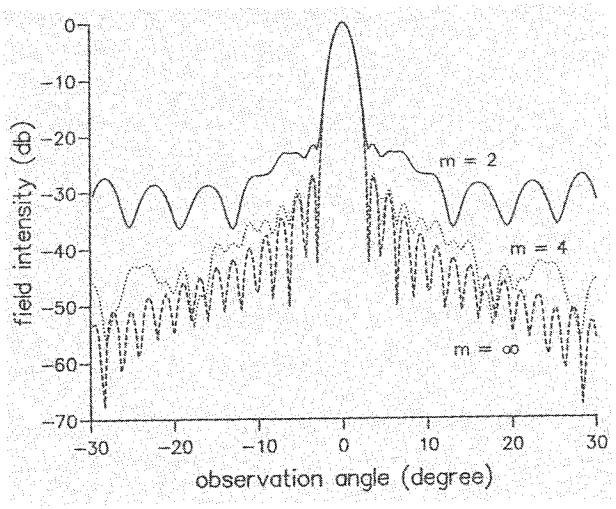

Fig. 3.8 Radiation patterns of subzone phase correcting zoneplates with –9.5dB edge illumination level.

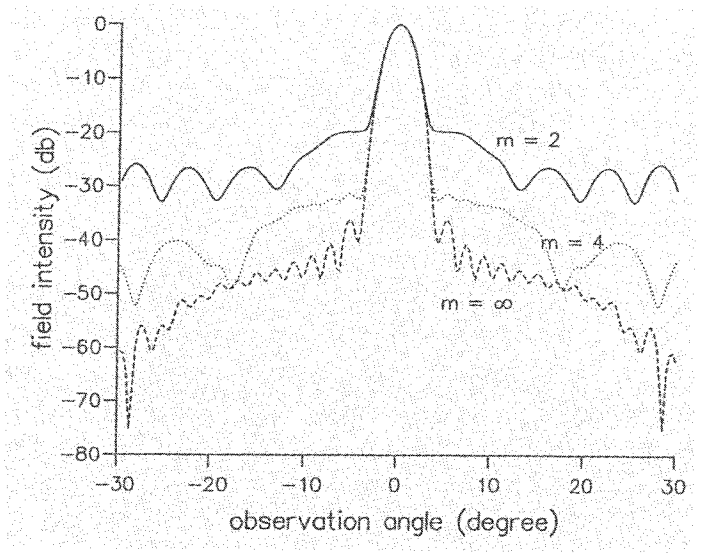

Fig. 3.9 Radiation Patterns of subzone phase correcting zoneplates with –20dB edge illumination level.

3.6 Multilayer Phase Correcting Zoneplate Reflector

As shown above, the subzone phase correction technique provides an effective approach to producing high efficiency zoneplate antennas. One practical way of realising the subzone phase correction is to employ a multilayer configuration [30], which is a natural evolution from the phase reversal zoneplate. The basic idea behind the phase reversal zoneplate is to place a refelctor a quarter wavelength behind the simple zoneplate in order to bring back the energy leaked from the transparent zones, thus resulting in an increase in efficiency by a factor of 2. Generally, one can use a number of dielectric substrates and place conductors in each subzone at the appropriate interface, which leads to the so-called multilayer zoneplate reflector antenna [14]. In theory, the efficiency of such an antenna increases with M, the number of dielectric substrates or the number of subzones in each full wave zone, but as seen earlier in this chapter the most significant improvement is obtained by increasing M from 2 to 4.

A multilayer quarter-wave zoneplate reflector and its phase correcting function is illustrated in Fig. 3.10. It consists of a metallic ground and three layers of concentric rings separated by three dielectric substrates. The rings are so located at different interfaces that for any full wave zone, there are (4 -j) layers of substrates above the conducting ring at the jth sub-zone (j = 1, 2, 3, 4), thus producing the required stepwise phase correction. The boundary radii of the sub-zones are determined by

$$(f^2+\rho_{nm}^2)^{\frac{1}{2}} = f+[(n-1)+\frac{m}{M}]\lambda \quad (m=1,2,\ldots,M;\ n=1,2,\ldots,N) \quad (3.25)$$

with M = 4. In fact, this configuration applies to any 1/M-wave zoneplate reflector. According to the geometrical optics analysis, the substrate thickness should be so determined that a normally incident ray experiences $2\pi/M$ phase delay after transmission and reflection. This gives

$$t = \lambda/(2M\sqrt{\varepsilon_r}) \quad (3.26)$$

where ε_r represents the relative dielectric constant of the substrate. With M = 4 for the quarter-wave zoneplate reflector, Eq. (3.25) leads to four constant phase shifts in each full wave zone: 0, $\pi/2$, π and $3\pi/2$.

An experimental prototype of the quarter-wave zoneplate reflector was designed and fabricated at Mawzones Ltd. The diameter of the zoneplate was chosen as D = 0.6m with 4 full wave zones and Eq. (3.25) gives the focal length f = 0.4m. From Fig. 3.7 the optimum edge illumination level is found to be -8.8dB and from Fig. 3.6 and Eq. (3.1) the maximum antenna efficiency is deduced as 62%. For convenience, a Marconi polyrod feed with 43 degree 3dB beamwidth was used, which yielded -10.8dB edge illumination level. Fig. 3.11 shows the measured antenna gain as a function of operating frequency. The antenna has a peak efficiency of 55.5% at 11.81GHz. The discrepancy with the theoretical expectation is due to the manufacturing inaccuracy, the losses in the feed and the dielectric substrate, the blockage and cross polarisation. Fig. 3.12 shows a typical E-plane radiation pattern which was obtained using the near field measurement technique and the sidelobe level was below -20dB.

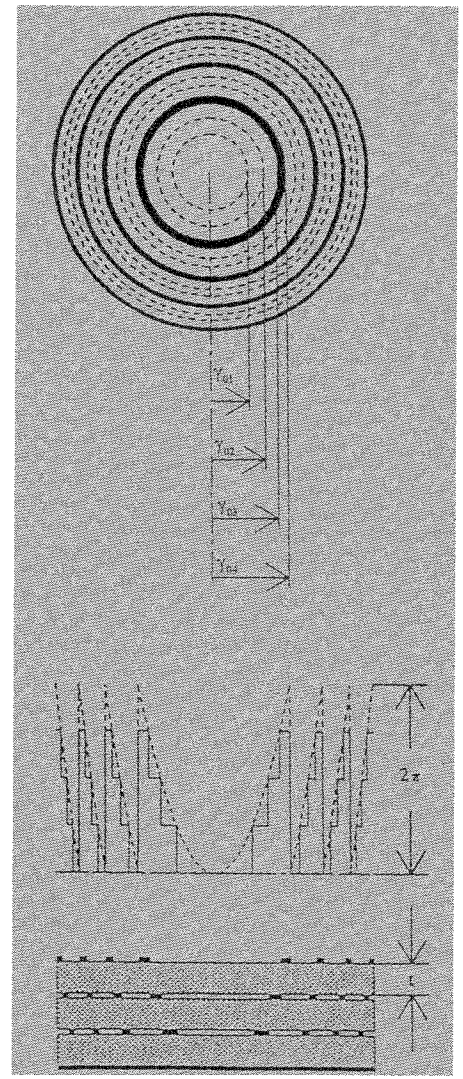

Fig. 3.10 A multilayer quarter-wave zoneplate reflector. Top: front view; middle: phase correction function; bottom: sectional view.

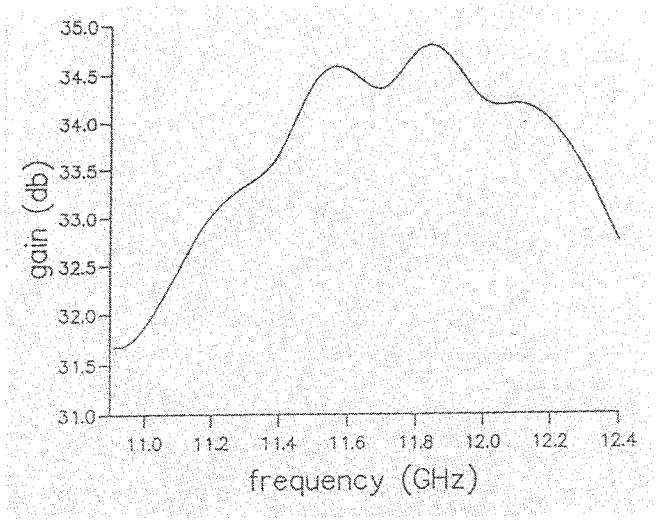

Fig. 3.11 Measured gain of the quarter-wave zoneplate reflector.

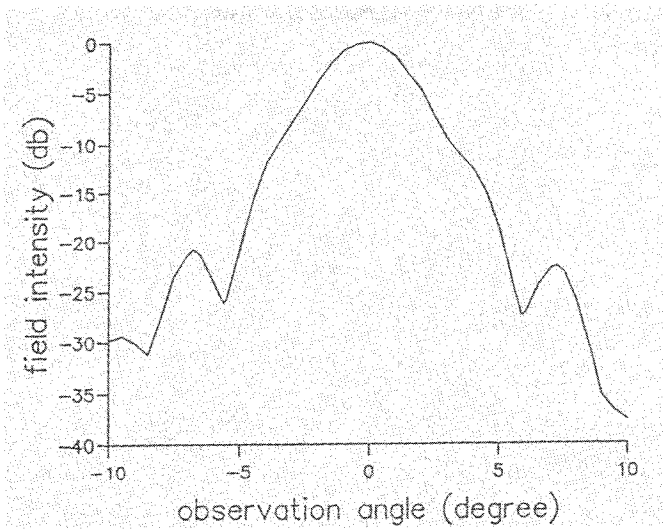

Fig. 3.12 Measured E-plane pattern of the quarter-wave zoneplate reflector.

3.7 Offset Multilayer Zoneplate Reflector

Replacing the circular subzones with elliptical ones, the multilayer configuration can be employed to produce an offset zoneplate reflector [15]. For illustration, an offset multilayer 1/5-wave zoneplate reflector is shown in Fig. 3.13. It consists of a metallic ground and four layers of different metallic patterns separated by four dielectric substrates. The top conducting layer covers the fifth subzones, the second one covers the fourth and the fifth subzones, the third one covers the third and the fourth subzones and the fourth one covers the second and the third subzones. The subzone boundaries are designed according to Eqs. (2.7) and (2.8). As an improvement to the configuration used for the circular zoneplate reflector, an overlapping area of one subzone is introduced here to reduce the scattering effect from the outer edges of the elliptical conducting rings. In fact, a few reflectors with different overlapping area were fabricated and tested. It appeared that extending the overlapping area further does not make noticeable difference. The four dielectric substrates shown in Fig. 3.13 serve as spacers and the substrate thickness, d, provides the path length difference required to produce a stepwise subzone phase correction function. A simple geometrical optics analysis gives

$$d = (1 - \sin^2\alpha/\varepsilon_r)^{1/2}\lambda\cos\alpha/(2M\sqrt{\varepsilon_r}) \qquad (3.27)$$

where ε_r is the relative dielectric constant of the substrate. For the present 1/5-wave zoneplate, this configuration produces five phase shifts in each subzone: 0, $2\pi/5$, $4\pi/5$, $6\pi/5$ and $8\pi/5$.

As an experimental prototype, an offset 1/5-wave zone reflector comprising two full wave zones was designed and fabricated to operate at 10.39GHz. The reflector has a 0.32m by 0.34m elliptical aperture, a 20^0 offset angle and a 0.19m focal length. The dielectric material used for the substrate has a permittivity $\varepsilon_r = 2.1$ and loss tangent $\tan\delta = 0.0069$. For convenience, the substrate thickness was chosen as 2mm, which is 6.4% greater than that given by Eq. (3.27). A pyramidal horn with aperture dimension 4.1cm by 2.8cm was used as the feed. This design was not aimed to obtain the optimum antenna performance, but to demonstrate the feasibility of the configuration. Fig. 3.14 shows the measured E-plane and H-plane patterns of the antenna at the design frequency. The two patterns

have almost the same 3dB beamwidth. Owing to the configuration asymmetry in the E-plane, however, it is observed that the main beam of the E-plane pattern becomes broadened from the shoulders. For comparison, an offset phase reversal zoneplate was also fabricated. Experimental results showed that the two reflectors have an average gain difference of 3.3dB in a 10.3% 3dB bandwidth. Taking the phase efficiency of the phase reversal zoneplate as 41%, this gives the predicted 87.5% phase efficiency for the 1/5-wave zoneplate [15]. For illustration, the measured E-plane patterns of the two reflectors are shown in Fig. 3.15. Significant reduction of the sidelobe level relative to the main lobe has been achieved by the multilayer zoneplate reflector.

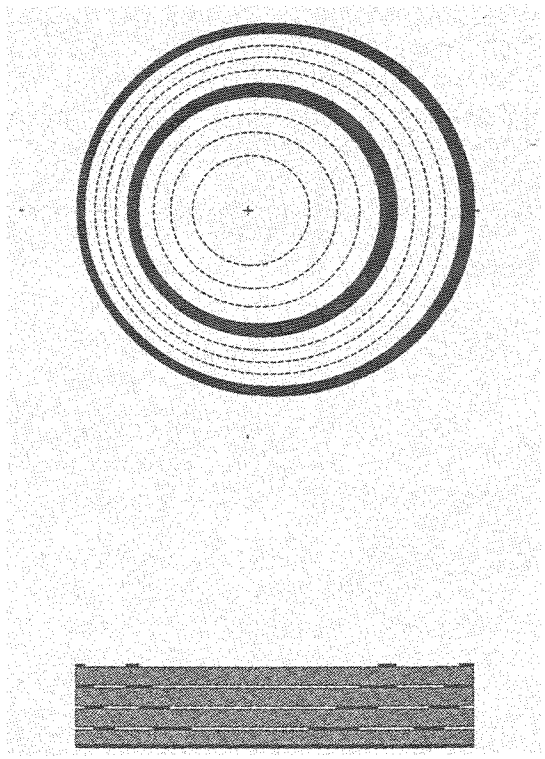

Fig. 3.13 An offset multilayer zoneplate reflector. Top: front view; bottom: sectional view.

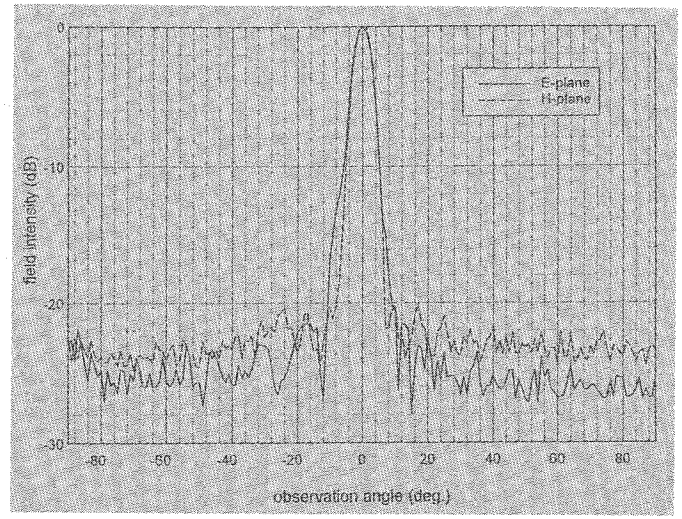

Fig. 3.14 E-plane and H-plane patterns of the offset 1/5-wave zoneplate reflector.

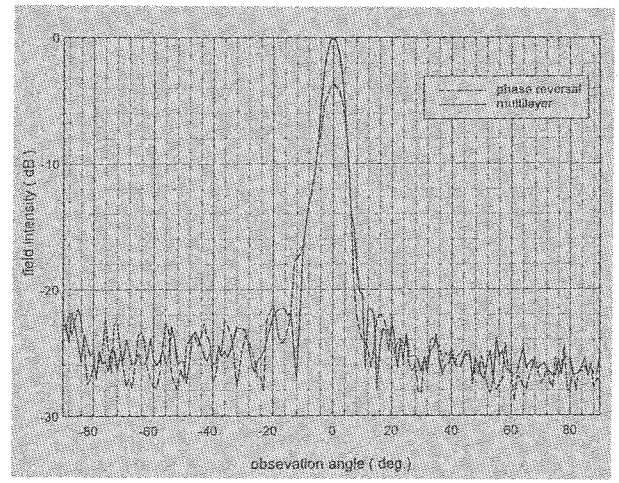

Fig. 3.15 E-plane patterns of the 1/5-wave and phase reversal offset zoneplate reflector.

3.8 Conclusions

A theory underlying the subzone phase correction technique is presented. Closed form expressions for the focal field of subzone phase correction zoneplate antennas are given. An aperiodic subzone phase correction technique is introduced to overcome the difficulty of placing too many phase shifters in the narrow outer full wave zones. Explicit expressions for the optimal subzone division, the corresponding phase shift and the phase efficiency are presented. It is proved that when a full wave zone of a zoneplate is divided into M subzones, the adjacent phase shifters must have $2\pi/M$ phase difference. If the same number of subzones are used in different full wave zones, the phase shifters in the first subzones can take any value but must be the same. When fewer subzones are used in the outer full wave zones, however, the phase shifters in the subzones of the inner full wave zones must be appropriately adjusted so that contributions from different full wave zones add in phase.

The antenna efficiency of the zoneplate reflector is also discussed and the optimum edge illumination level against f/D ratio is given. Using Kirchhoff diffraction integral, the sidelobe performance of the subzone phase correcting zoneplate is investigated. It is shown that the subzone phase correcting technique can significantly reduce the antenna sidelobes. However, the residual phase error at each subzone and zoning do limit the scope of the sidelobe reduction. For a practical zoneplate antenna, such as the quarter-wave zoneplate favoured by various research groups, the sidelobe level is unlikely to be lower than -30dB. A further study on the sidelobe issue will be given in the next chapter.

The design and experiments of two multilayer zoneplate reflectors, a quarter-wave circular zoneplate and a 1/5-wave offset zoneplate are reported. It is shown that the multilayer configuration provides a viable engineering approach to realising high efficiency phase correcting Fresnel zoneplate antennas.

Chapter 4 Zonal Reflectors

In chapter 3, it was demonstrated that the efficiency of a Fresnel zoneplate antenna can be effectively improved by using subzone phase correcting techniques, such as the multilayer phase correction technique. However, both theoretical study and experiments showed that the sidelobe level of the zoneplate antenna tends to be high and the envelope of the sidelobes tends to be flat. Obviously, an understanding of this phenomenon is very important. This chapter is aimed to provide some insight into the sidelobe performance of Fresnel zoneplate antennas. The physical model employed as the reference is the parabolic zonal reflector, which comprises a set of confocal parabolic segments arranged along a plane surface. Within the accuracy of scalar optical theory, such a configuration should offer ideal phase correction. To model the multilayer zoneplates, the stepped zonal reflector is introduced, in which the parabolic function is replaced by a stepwise function. Since an accurate analysis of any two dimensional zonal reflector (i. e. those with a two dimensional aperture) using the method of moments (MoM) is bound to demand excessive computation power, an analysis of one dimensional zonal reflectors is carried out instead. Here, the term "one dimensional zonal reflectors" refer to those which are traditionally called "cylindrical reflectors" [16, 20]. The second objective of this chapter is to demonstrate an engineering approach to reducing the near-in sidelobes of the stepped zoneplate antennas.

This chapter is organised as follows. In section 4.1, the profiles of three one-dimensional zonal reflector configurations are described. The first is the parabolic zonal reflector mentioned above. The second is termed the standard stepped zonal reflector, in which each full-wave zone is divided into M-subzones and M-1 steps are used to provide M-1 phase increments of $2\pi/M$ followed by one step of $-2\pi(M\text{-}1)/M$. The third configuration is a modification to the second one, in which the first subzone in each full-wave zone is split into two half-subzones located at the two ends of the full wave zone, thus allowing M steps of $2\pi/M$ phase increment followed by one step of -2π to be used to achieve a full range of $0\text{-}2\pi$ phase correction. Section 2 gives a brief description of the MoM model used and numerical results are

given in section 4.3. By comparing the MoM solution and the physical optics (P. O.) approximation, it is shown that the contribution of the corner diffraction is significant, but zoning intrinsically plays the most important role in raising the far-out sidelobes. Of the two types of stepped zonal reflectors investigated, the one with modified configuration offers much lower near-in sidelobe levels, very close to those of the corresponding parabolic one. These results are instructive in the design of both conducting zonal reflectors and multilayer phase correcting zoneplates.

4.1 Parabolic and Stepped Zonal Reflectors

The zoning technique was initially introduced to reduce the weight of lens antennas [32, 33]. When used in a cylindrical reflector, it leads to the parabolic zonal reflector shown in Fig. 4.1, which comprises a set of confocal parabolic sub-reflectors arranged along a plane surface. In a polar co-ordinate system whose z-axis coincides with the focal line, the surface of the parabolic zonal reflector is described by

$$\rho=\frac{2f-(n-1)\lambda}{1+\cos\phi} \qquad (\varphi_{n-1}\le|\varphi|<\varphi_n,\ n=1,2,\ldots,N) \tag{4.1}$$

where f is the focal length of the central sub-reflector, λ is the operating wavelength, N is the number of full wave zones in each symmetrical half of the reflector and

$$\phi_n=\cos^{-1}\frac{f}{f+n\lambda}. \tag{4.2}$$

There are N wedges on each side of the reflector centre and the height of the nth wedge is given by

$$t_n=\frac{f\lambda}{2f+n\lambda}. \qquad (n=1,2,\ldots,N) \tag{4.3}$$

Eq. (4.3) indicates that the outer wedges are lower than the inner ones. It is shown in Fig. 4.1 that zoning reduces the height of the reflector, but it introduces 2(N-1) slopes used for joining adjacent parabolic segments. These slopes produce shadowing areas in the aperture field.

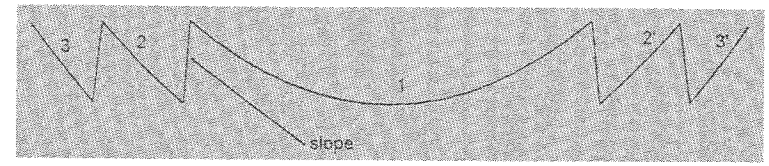

Fig. 4.1 Profile of the zonal parabolic reflector.

According to the subzone phase correction theory described in the preceding chapter, the parabolic zonal reflector can be approximated by a stepped zonal reflector. In the standard stepped zonal reflector, each full-wave zone is divided into M subzones and M steps are used at the subzone boundaries in order to provide a stepped phase correction to a normally incident plane wave. The height of the first M-1 steps are given by

$$t_s=\frac{\lambda}{2M}, \tag{4.4}$$

which yields the height of the overall reflector (the Mth step):

$$t=\frac{(M-1)\lambda}{2M}. \tag{4.5}$$

In contrast to the parabolic zonal reflector, the wedges of the standard stepped zonal reflector reach the same maximum height in every full-wave zone. For convenience, we define the aperture plane of the stepped zonal reflector as the one that coincides with the tips of the wedges and measure the focal length f from the aperture plane to the focal point. Accordingly, the outer boundary of the mth subzone in the nth full-wave zone, y_{nm}, is given by

$$\sqrt{f^2+y_{nm}^2}=f+[(n-1)+\frac{m}{M}]\lambda \quad (n=1,2,\ldots,N;\ m=1,2,\ldots,M). \tag{4.6}$$

This configuration serves as a good model of the multilayer phase correcting zoneplate described in chapter 3. When illuminated by a normally incident plane wave, it produces the following quantified phase shifts: -2(M-1)π/M, -

$2(M\text{-}2)\pi/M$, ..., 0. A standard stepped zonal reflector with $M = 4$ is shown by the solid line in Fig. 4.2.

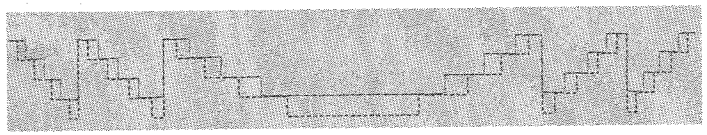

Fig. 4.2 Profiles of the standard and modified stepped Fresnel zonal reflectors with $M = 4$.

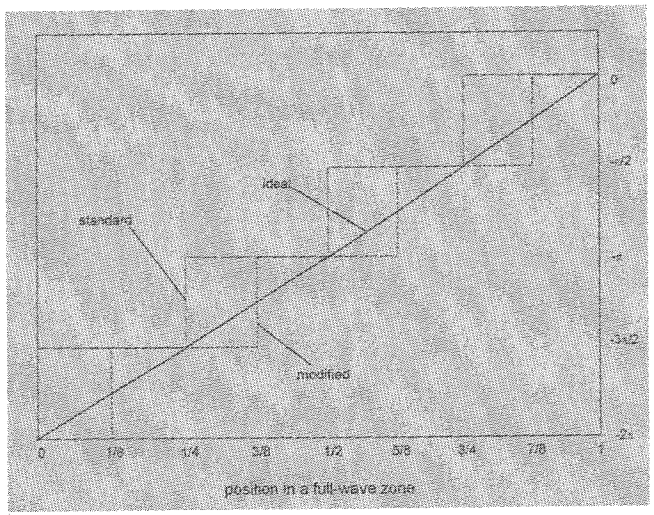

Fig. 4.3 Phase correcting functions of the standard and modified stepped Fresnel zonal reflectors.

The phase correction achieved by the standard stepped zonal reflector goes over a range of $(-2(M\text{-}1)\pi/M, 0)$. In order to obtain a full range of $(-2\pi, 0)$ phase correction, the standard stepped zonal reflector can be modified as follows: the first subzone with $-2(M\text{-}1)\pi/M$ phase shift in each full-wave zone is split into two half-subzones. Then, the first half-subzone is moved downward to produce a -2π phase shift. Accordingly, the subzone boundaries are adjusted so that the first half-subzone are followed by M-1 full subzones, and the other half-subzone is located at the end of the full-wave zone. This yields M+1 steps in each full-wave zone. Fig. 4.2 shows a

modified stepped zonal reflector with $M = 4$ by the dashed line. With the focal length measured from the aperture plane, the zonal boundaries of the modified stepped zonal reflector are given by

$$\sqrt{f^2+y_{nm}^2} = \begin{cases} f+[(n-1)+\dfrac{(m-0.5)}{M}]\lambda & (1 \le m \le M) \\ f+n\lambda & (m = M+1) \end{cases} \quad (4.7)$$

Fig. 4.3 shows the phase correcting functions provided by the standard and the modified stepped zonal reflectors to a normally incident plane wave, in comparison with the ideal phase correcting function.

4.2 Method of Moments (MoM) Model

To analyse the radiation performance of zonal reflectors, assume that the reflectors are illuminated by a directional TM-wave given by

$$E_z^i(\rho,\phi) = \begin{cases} -\dfrac{k\eta}{4}\sqrt{\dfrac{2j}{\pi k\rho}}\exp(-jk\rho)\cos^p\phi & (0 \le |\phi| \le \dfrac{\pi}{2}) \\ 0 & (\dfrac{\pi}{2} < |\phi| \le \pi) \end{cases} \quad (4.8)$$

where k and η are the wave number and the intrinsic impedance in free space respectively, and the index p is used to control the edge illumination level. With such an incident field, the induced current has only a z-component uniform in the z-direction and the scattering field is given by

$$E_z^s(\vec{\rho}) = -\frac{k\eta}{4}\int_c J_z(\vec{\rho}\,')H_0^{(2)}(k|\vec{\rho}-\vec{\rho}\,'|)dl \quad (4.9)$$

where J_z is the induced current to be determined and $H_0^{(2)}(x)$ is the Hankel function of the second kind and zero order [35, 36]. According to the boundary condition, the superposition of the incident and scattering fields must produce an electric field with vanishing tangential component on the conducting surface of the zonal reflector, which leads to the following integral equation :

$$E_z^i(\vec{\rho}) = \frac{k\eta}{4}\int_c J_z(\vec{\rho}')H_0^{(2)}(k|\vec{\rho}-\vec{\rho}'|)dl \qquad (4.10)$$

Eq. (4.10) can be solved by the method of moments (MoM). When the pulse basis functions and point matching are used, the impedance matrix elements are derived as

$$Z_{ij} = \frac{k\eta}{4}\int_{\Delta c_j} H_0^{(2)}(k|\vec{\rho}-\vec{\rho}_i|)dl \qquad (i \neq j) \quad (4.11.a)$$

$$Z_{ii} = \frac{k\eta}{4}\Delta C_i[1 - j\frac{2}{\pi}\ln(\frac{\gamma k\Delta C_i}{4e})] \qquad (4.11.b)$$

where $\gamma = 1.781072...$ is Euler's constant, $e = 2.718283$, and ΔC_i and $\vec{\rho}_i$ represent the length and the position of the central point of the ith segment respectively [35, 36]. The ith element of the voltage matrix is given by

$$V_i = E_z^i(\vec{\rho}_i). \qquad (4.12)$$

Thus, we obtain a matrix equation of the following form

$$[Z][J] = [V]. \qquad (4.13)$$

Once Eq. (4.13) is solved, the radiation field of the reflector can be obtained through the following equation:

$$E_z^r(\theta) = \frac{k\eta}{4}\sqrt{\frac{2j}{\pi k\rho}}\,exp(-jk\rho)\sum J_i\int_{\Delta C_i}\exp[-jk\rho'\cos(\theta+\phi)]dl + E_z^i \qquad (4.14)$$

where J_i is the current on the ith segment ΔC_i and θ is the angle between the observation direction and the norm of the zonal reflector.

4.3 Numerical Results

To understand the performance of different zonal reflectors, some numerical results are given in this chapter. First, the sidelobe performance of the parabolic zonal reflector is compared with that of the conventional parabolic reflector without zoning. Then, the performance of the two different stepped zonal reflector configurations are studied. Finally, the effect of subzone phase correction is investigated.

4.3.a Sidelobe Profile of the Parabolic Zonal Reflector

Fig. 4.4 shows the predicted radiation pattern of a parabolic zonal reflector with three full-wave zones in comparison with that of a conventional parabolic reflector. The two reflectors have the same focal length $f = 0.25m$, the same aperture width $D = 0.4m$ and the same edge illumination level of -10dB, and are operated at 12GHz. After some optimisation process, the number of basis functions in the MoM model is chosen as 296 for the conventional parabolic reflector and 310 for the parabolic zonal reflector. It is seen in Fig. 4.4 that the radiation pattern of the zonal reflector has slightly wider main beam, clearer first nulls and lower near-in sidelobes, but much higher far-out sidelobes.

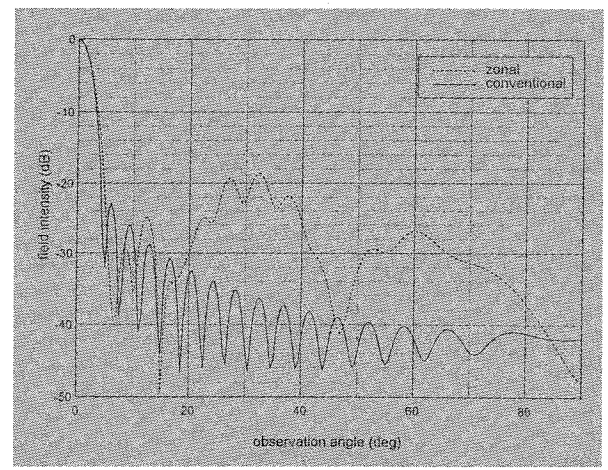

Fig. 4.4 Radiation patterns of zonal and conventional parabolic reflectors.

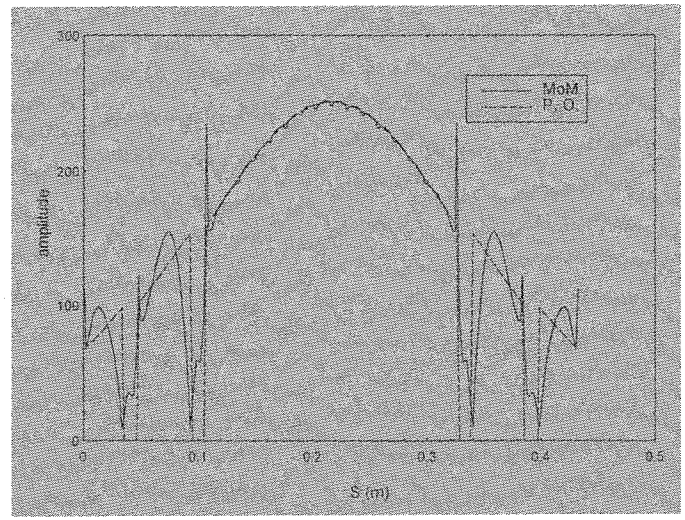

(a)

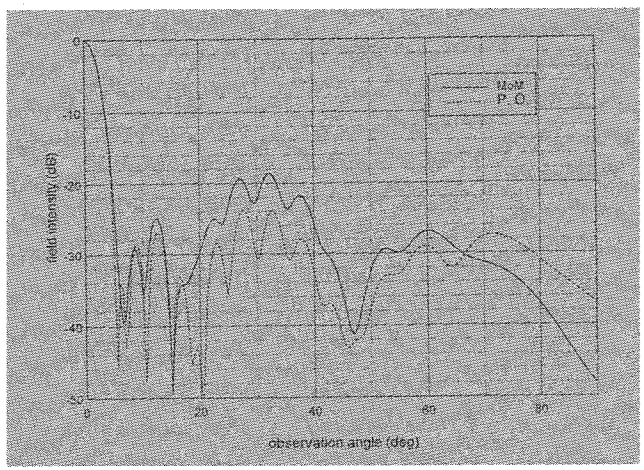

(b)

Fig. 4.5 MoM and P. O. solutions of the induced current on the zonal parabolic reflector (a) and the associated radiation patterns (b).

It had been noticed in several experiments that stepped zonal reflectors tend to have relatively high far-out sidelobes. Although the near-in sidelobes can be reduced by using phase correcting techniques, the far-out sidelobes always stay high. One explanation was that there is strong corner diffraction in the zonal reflectors. To investigate this phenomenon, Fig. 4.5.a shows the current distribution of the same parabolic zonal reflector in comparison with the physical optics (P. O.) current, where S is the length from the reflector end measured along the surface, not the length in the aperture plane. It is seen that the two currents differ significantly around the corners. On the slopes joining adjacent parabolic segments, the P.O. current vanishes whereas the MoM solution goes from infinity to some non-zero local minima.

The radiation patterns of the two currents shown in Fig. 4.5a are compared in Fig. 4.5.b. Not surprisingly, the two patterns have similar near-in sidelobes but exhibit about 5dB difference in the far-out sidelobe level. However, it is observed that although there is no singularity in the P. O. current, it still produces high far-out sidelobes, which leads to a flat sidelobe profile rather than a descending one. This indicates that the far-out sidelobe level of the parabolic zonal reflector is mainly caused by zoning, or by shaping of the reflector. Therefore, although reducing the effect of corner diffraction can decrease the sidelobes of a parabolic zonal reflector significantly, it cannot produce a low-sidelobe reflector antenna. This may limit the use of zonal reflectors in some applications.

In fact, when the slopes joining adjacent parabolic segments are neglected, a parabolic zonal reflector can be taken as an array of parabolic sub-reflectors (see Fig. 4.1). The main beams of all the sub-reflectors are pointed in the same direction. Since the central sub-reflector is much wider than the others, its main beam is much narrower. The addition of a narrow beam with a few wide beams inevitably produces the high far-out sidelobes of the zonal reflector.

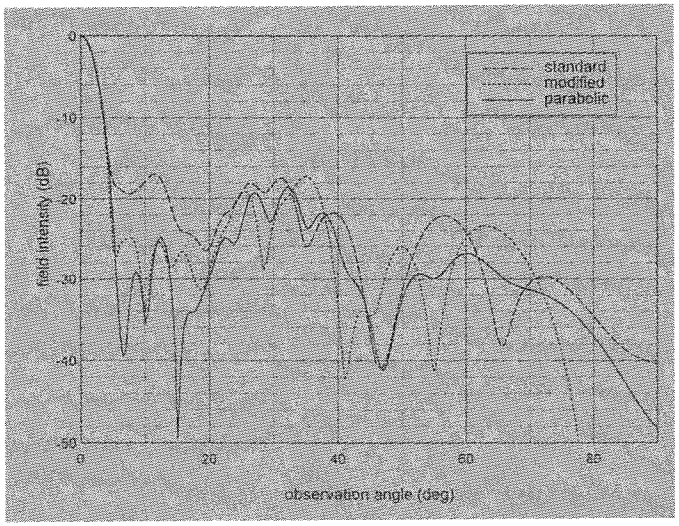

Fig.4.6 Radiation patterns of a zonal parabolic reflector, and the standard and modified stepped ones.

4.3.b Comparison Between the Two Stepped Zonal Reflectors

One approach to lowering the manufacturing cost of the parabolic zonal reflector is to use the stepped zonal reflector. Its one dimensional version consists of a set of horizontally and vertically placed conducting strips. A further practical modification of the stepped zonal reflector is to remove the metal joining adjacent subzones and to employ low-loss dielectric substrates as spacers, which results in the multilayer zoneplate reflector [30]. Since the multilayer zoneplate reflector requires a different theoretical model, it is not dealt with here.

Fig. 4.6 shows the predicted radiation patterns of a standard stepped zonal reflector and its modified counterpart, both with $N = 3$, $M = 4$, $D = 0.4m$, -10dB edge illumination level and operating at 12GHz. Since the reflector surfaces consist of a number of straight segments with adjacent ones perpendicular to each other, the induced currents exhibit many singularities due to the effect of corner diffraction. Therefore, larger number of basis functions are required than those employed for the parabolic reflector of the similar size. Furthermore, since the widths of subzones

decrease when the distances between the subzones and the reflector centre increase, finer sub-domain divisions must be used in the outer subzones to account for the rapid variation of the induced current. In this particular case, 400 and 444 basis functions, which are allocated to both the horizontal and the vertical conducting walls, are used for the standard and the modified stepped zonal reflectors respectively. For comparison, the radiation pattern of the corresponding parabolic zonal reflector is also presented in Fig. 4.6. It is seen that the modified stepped reflector has much lower near-in sidelobes and deeper nulls and the parabolic zonal reflector gives the best performance, or the lowest sidelobe profile.

Since the number of steps of the modified stepped zonal reflector mentioned above is five, while that of the standard one is four, the radiation pattern of the standard stepped zonal reflector with $M = 5$ is compared with that for $M = 4$ in Fig. 4.7 It is seen that the difference between the near-in sidelobes of the two patterns is much less significant. This indicates that modifying the configuration of the standard stepped zonal reflector is necessary in reducing the near-in sidelobes. This, in fact, has been experimentally demonstrated with the multilayer configuration [34].

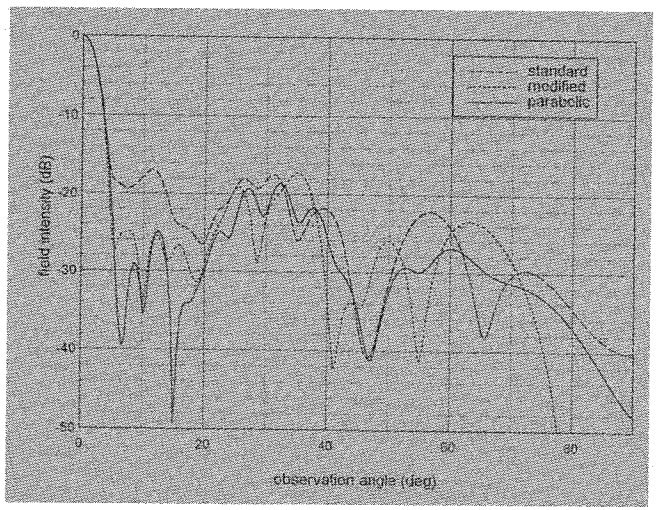

Fig. 4.7 Radiation patterns of the standard stepped zonal reflectors with different number of subzones M.

4.3.c Sidelobe Level versus M

As pointed out in chapter 3, the number of subzones in each full wave zone, *M*, determines the phase efficiency of the zonal reflector. To evaluate its influence on the sidelobe level, Fig. 4.8 shows the radiation patterns of the modified stepped zonal reflectors with different *M*. It is observed that the quarter-wave zonal reflector produces a radiation pattern very close to that of the corresponding parabolic one. Increasing *M* further brings little improvement to the sidelobe profile. This agrees with the similar conclusion made for the phase efficiency of zoneplate antennas [5, 14].

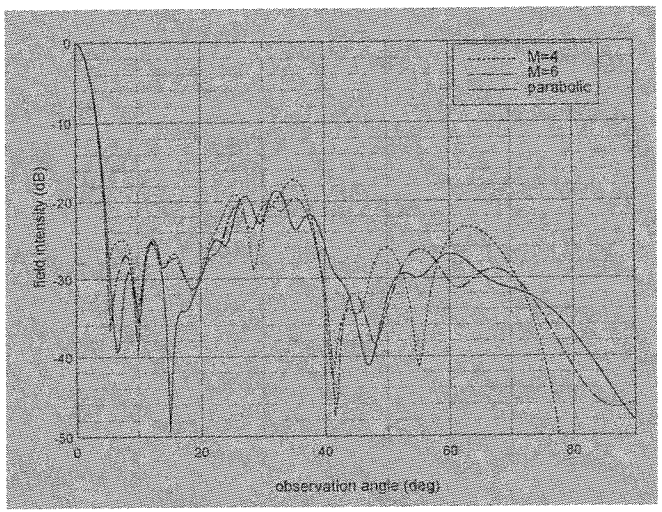

Fig. 4.8 Radiation patterns of the modified stepped zonal reflectors with different number of subzones M.

4.4 Conclusions

The method of moments (MoM) has been used in the analysis of one dimensional zonal reflectors. Three types of configurations have been described and investigated, which include the parabolic zonal reflector, the standard stepped zonal reflector and the modified stepped zonal reflector. It is shown that corner diffraction makes significant contribution to the

sidelobe level, but zoning intrinsically produces high far-out sidelobes. Furthermore, it is proved that the near-in sidelobes of the stepped zonal reflector can be greatly reduced by replacing the standard geometrical configuration with the modified one.

Chapter 5 Single Printed Flat Reflectors

As shown in the preceding chapters, a high efficiency Fresnel zoneplate reflector can be realised by stacking a few layers of dielectric together with metallic zonal patterns in between or by employing a stepped structure. Although these techniques are simple and insensitive to manufacturing tolerances, they can be relatively labour intensive and therefore costly. A much more economical and academically more interesting way of producing high efficiency Fresnel zone reflectors is to employ a single array of inhomogeneous phase correcting elements printed on a grounded dielectric substrate, thus resulting in the single printed flat reflector [17, 41]. In such a configuration, the phase correction is accomplished by an appropriate design of the array elements together with the substrate.

In this chapter, the concept of reflective phase shifters incorporating frequency selective surfaces is discussed. The integral equation and the method of moments (MoM) for solving the equation are presented. The performance of reflective phase shifters incorporating conducting rings is then investigated. With straightforward modification to the basis functions, the equations can be easily employed for reflective phase shifters using different types of elements. Based on both theoretical analysis and experimental verification, the design of a quarter-wave Fresnel zone reflector incorporating rings is described and experimental results are given. Finally, other single printed flat reflectors are discussed to complete the discussion on the subject.

5.1 Reflective Phase Shifter Incorporating FSS

The principle behind the design of the single printed reflectors can be easily understood by looking at the function of frequency selective surfaces (FSS). An array of homogeneously distributed conducting elements printed on a low-loss substrate constitutes a FSS. Modelling free space as an infinite transmission line, a free standing FSS can be taken as a shunt

reactance B. When the FSS resonates, it gives either total reflection ($B = 0$) or total transmission ($B = \infty$) to an incident wave. When the FSS is off resonance, the incident electromagnetic energy is inevitably divided between reflection and transmission [37, 38]. Therefore, FSSs are usually employed as electromagnetic wave filters [39]. If the other side of a low-loss substrate is grounded, however, most of the energy in the incident wave will be reflected back, thus yielding a reflective phase shifter [40]. With a given substrate, the phase shift of the reflecting wave is determined by the equivalent reactance B. Fig. 5.1 shows the physical configuration and the transmission line model of the reflective phase shifter, where Z and Z_1 represent the wave impedance in free space and in the dielectric, respectively. The phase of the reflection coefficient Γ is given by

$$\mathrm{Arg}(\Gamma) = \pi - 2\mathrm{tg}^{-1}\{BZ_1\tan(k_1 t)/[Z(Z_1\tan(k_1 t) + B)]\} \qquad (5.1)$$

where t is the substrate thickness and $k_1 = 2\pi/\lambda_1$, with λ_1 as the wavelength in the dielectric.

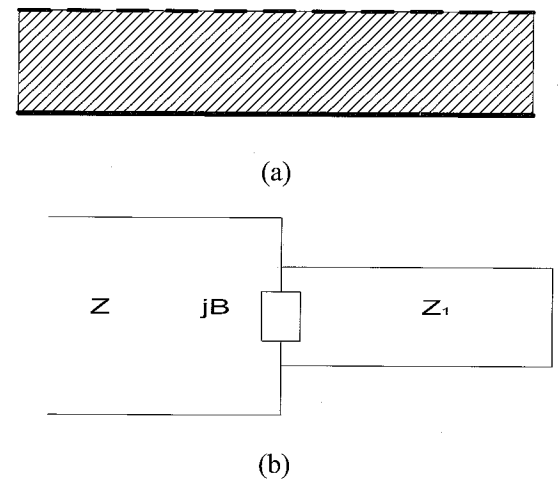

Fig. 5.1 Illustration of a reflective phase shifter (a) and the corresponding transmission line model.

Fig. 5.2 gives the phase shifting performance with the relative dielectric constant $\varepsilon_r = 2$ and varying substrate thickness. It is observed that the phase shift changes rapidly around $B = 0$ region and a dynamic range of

about 300° can be obtained by increasing B from -4Z to 4Z. As the substrate thickness t increases, the phase shifting curve for $B < 0$ gets flatter and that for $B > 0$ becomes sharper.

To apply the reflective phase shifter technique in a Fresnel zone reflector antenna, the employed FSS must provide the required flexibility of the equivalent reactance. The focusing ability will be severely limited if inappropriate FSS elements are used. One good candidate is the FSS consisting of conducting rings, whose equivalent reactance is determined by the circumference of each ring and the distance between adjacent rings [39]. In fact, there is no necessity in investigating the relation between the FSS parameters and the equivalent reactance. The phase shift of a given structure can be directly analysed by using the spectral domain integral equation method. As shown in the following section, this involves setting a spectral domain integral equation on the surface where the FSS lies and solving the induced current with the method of moments (MoM).

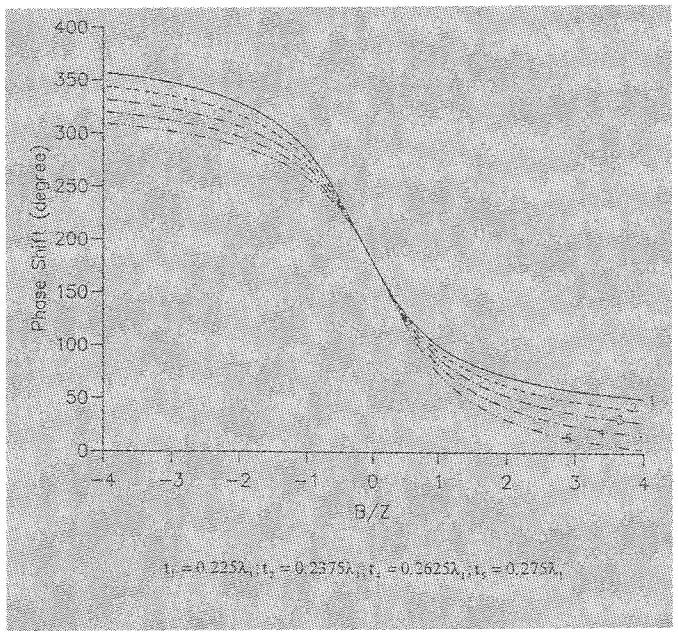

Fig. 5.2 Phase shifting performance of reflective phase shifters with different substrate thickness.

5.2 Analysis of Reflective Phase Shifters

Assume a plane electromagnetic wave is incident on a homogeneous reflective phase shifter with its transverse electric field $\boldsymbol{E}_t^i$ (x,y,z) = [E_x^i , E_y^i]^t given by

$$E_x^i(x,y,z) = E_x^i(\alpha_{00},\beta_{00})\exp[j(\alpha_{00}x + \beta_{00}y - \sqrt{k_0^2 - \alpha_{00}^2 - \beta_{00}^2}\,z)] \quad (5.2.a)$$

$$E_y^i(x,y,z) = E_y^i(\alpha_{00},\beta_{00})\exp[j(\alpha_{00}x + \beta_{00}y - \sqrt{k_0^2 - \alpha_{00}^2 - \beta_{00}^2}\,z)] \quad (5.2.b)$$

where α_{00} and β_{00} are related with the incident angles θ_{inc} and ϕ_{inc} through the following equations:

$$\alpha_{00} = k_0 \sin\theta_{inc} \cos\phi_{inc} \quad (5.3.a)$$

$$\beta_{00} = k_0 \sin\theta_{inc} \sin\phi_{inc} \quad (5.3.b)$$

$$k_0 = 2\pi/\lambda_0 \quad (5.3.c)$$

with λ_0 as the operating wavelength in free space [42]. If the array printed over the grounded substrate has an equilateral triangular grid (see Fig. 5.3), the scattered fields in and outside the substrate can be expressed as sums of the Floquet modes with discrete spectra given by

$$\alpha_{mn} = \alpha_{00} + 2m\pi/d \quad (5.4.a)$$

$$\beta_{mn} = \beta_{00} + 4n\pi/(\sqrt{3}\,d) - 2m\pi/(\sqrt{3}\,d). \quad (5.4.b)$$

where d is the spacing between the adjacent elements [43]. The boundary conditions at the interface between the phase shifter and free space ($z = 0$ plane) yield the following functional equation:

$$\sum_{mn} [G_{mn}]\boldsymbol{J}(\alpha_{mn},\beta_{mn})\exp[j(\alpha_{mn}x + \beta_{mn}y)]$$

$$= -[B_{00}]\,\boldsymbol{E}_t^i(\alpha_{00},\beta_{00})\exp[j(\alpha_{00}x + \beta_{00}y)] \quad (5.5)$$

where

$$[G_{mn}] = (1 - \exp(-j2k_{1z}t)]\,[M_{mn}]^{-1}[X]$$

$$[B_{00}] = 2(1 - \exp(-j2k_{1z}t)]\,[M_{00}]^{-1}[K^0_{00}]\,[X]$$

$$[M_{mn}] = (1 + \exp(-j2k_{1z}t)][K^1_{mn}]\,[X] + (1 - \exp(-j2k_{1z}t)]\,[K^0_{mn}]\,[X]$$

$$[K^i_{mn}] = \frac{-1}{\omega\mu k_{iz}}\begin{bmatrix} k_i^2 - \alpha_{mn}^2 & -\alpha_{mn}\beta_{mn} \\ -\alpha_{mn}\beta_{mn} & k_i^2 - \beta_{mn}^2 \end{bmatrix}$$

$$[X] = \begin{bmatrix} 0 & 1 \\ -1 & 0 \end{bmatrix}$$

$$k_{iz} = \sqrt{k_i^2 - \alpha_{mn}^2 - \beta_{mn}^2}$$

with k_i as the wave number in medium i (0 for free space and 1 for the substrate) and t as the substrate thickness. $\boldsymbol{J}(\alpha_{mn},\beta_{mn}) = [J_x(\alpha_{mn},\beta_{mn}), J_y(\alpha_{mn},\beta_{mn})]^t$ is the Fourier transformation of the induced current, $\boldsymbol{j}(x,y)$, on any array element at spectral point (α_{mn},β_{mn}), which can be obtained by solving Eq. (5.5) with the method of moments [42].

Owing to their symmetry and compactness, printed circular conducting rings were used as array elements in our research [39]. For narrow rings, the induced electric currents can be expressed as a series of harmonic functions of the form

$$\boldsymbol{j}(x,y) = \Sigma a_p \boldsymbol{j}_p$$

$$= \Sigma a_p \exp(jp\varphi)\,\boldsymbol{\varphi} \qquad (5.6)$$

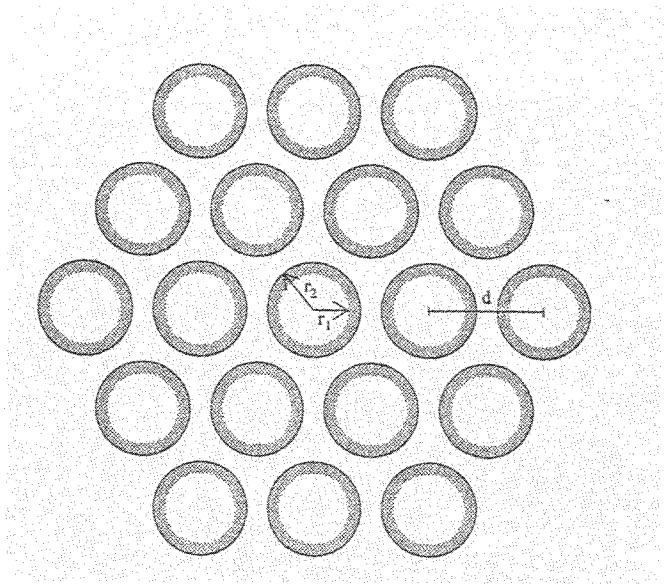

Fig. 5.3 Illustration of a ring array with triangular grid.

where φ is the angular position of a point on the ring circumference. Fourier transforming $\boldsymbol{j}_p$ gives

$$J_{px}(\alpha_{mn},\beta_{mn}) = (-j)^p\pi\exp(jp\varphi_{mn}) \int_{r_1}^{r_2} [\exp(j\varphi_{mn})\,J_{p+1}(\gamma_{mn}r) + \exp(-j\varphi_{mn})\,J_{p-1}(\gamma_{mn}r)\,]rdr \qquad (5.7.a)$$

$$J_{py}(\alpha_m,\beta_{mn}) = (-j)^{p+1}\pi\exp(jp\varphi_{mn}) \int_{r_1}^{r_2} [\exp(j\varphi_{mn})\,J_{p+1}(\gamma_{mn}r) - \exp(-j\varphi_{mn})\,J_{p-1}(\gamma_{mn}r)]rdr \qquad (5.7.b)$$

where r_1 and r_2 are the inner and outer radii of the rings (see Fig. 5.3), J_p is the Bessel function of the first kind of the p'th order, and

$$\varphi_{mn} = \tan^{-1}(\beta_{mn}/\alpha_{mn}) \qquad (5.8.a)$$

$$\gamma_{mn} = \sqrt{\alpha_{mn}^2 + \beta_{mn}^2} \qquad (5.8.b)$$

It should be pointed out that although the ring width r_2 - r_1 is small, γ_{mn} can be very large for higher order modes, so numerical integration must be used to evaluate Eq. (5.7). Substituting Eq. (5.6) and Eq. (5.7) into Eq. (5.5) and using Galerkin's method produces a linear system of algebraic equations, whose solution gives the coefficients a_n in Eq. (5.6) [39, 42].

For our application, a/λ_0 and b/λ_0 are less than 1 and the phase shifters are designed to provide desired phase delays to a normally incident plane wave, so $\alpha_{00} = \beta_{00} = 0$. Then, the only propagating mode of the scattering field outside of the dielectric is the reflected plane wave given by

$$\boldsymbol{E}^r(x,y,z) = \boldsymbol{E}^r(0,0)\exp(jk_0 z) \qquad (5.9)$$

where

$$\boldsymbol{E}^r(0,0) = \{[B_{00}] - [I_2]\}\boldsymbol{E}^i(0,0) + [G_{00}]\boldsymbol{J}(0,0) \qquad (5.10)$$

with $[I_2]$ as the two dimensional identity matrix. Since there are no z-components in the incident and reflected fields, the subscript 't' is dropped in Eqs. (5.9) and (5.10). The phase delay of a reflective phase shifter is defined as the phase difference between the incident and reflected plane waves at the plane where the ring array is located (z = 0). Accordingly, a totally conducting surface gives π phase delay, whereas the phase shift of a clear substrate with a backing ground is a function of the substrate thickness and permittivity.

To validate the theoretical model, two homogeneous reflective phase shifters with different size rings were fabricated and tested in a bandwidth from 9.8GHz to 11GHz. The substrate is of 2.08 permittivity and 5mm thickness, and different parameters were chosen for the two ring arrays. For the first, d = 8.5mm, r_1 = 2mm and r_2 = 3mm; while for the second, d = 16mm, r_1 = 7.5mm and r_2 = 7.9mm. Fig. 5.4 shows good agreement between the theoretical and experimental results. Given a point on a zoneplate surface, the phase compensation required to focus an incoming plane wave increases with frequency. However, it is seen from Fig. 5.4 that for a fixed configuration, the phase shift provided by the reflective phase shifter decreases with increasing frequency. This, to some extent, may limit

the bandwidth of the zoneplate antenna based on this phase correcting technique.

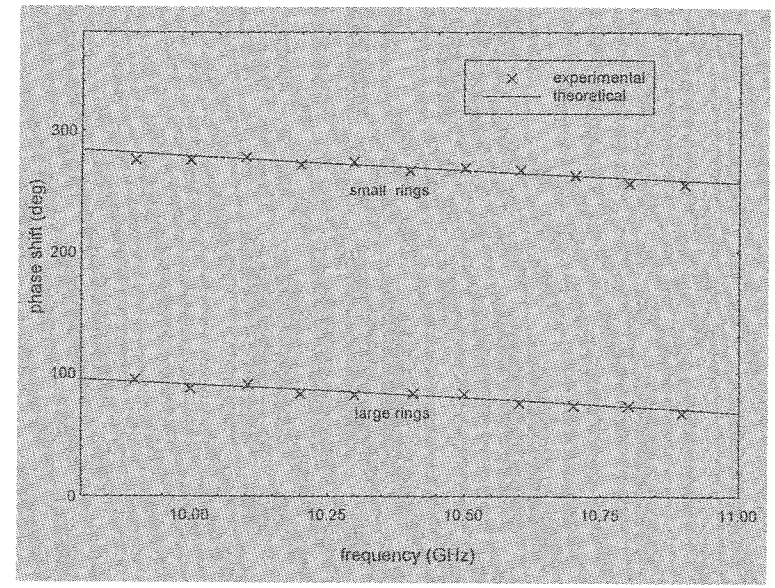

Fig. 5.4 Frequency response of two reflective phase shifters.

Fig. 5.5 shows the numerical results of a reflective phase shifter as a function of the median ring radius $r = (r_1 + r_2)/2$ for three different distances between ring centres, d = 6, 9 and 15mm. The operating frequency is chosen as 11.4 GHz, which is the design frequency of an antenna to be described in the following section. The substrate thickness is 4.5 mm, i.e., approximately a quarter wavelength in the dielectric with a permittivity of 2.08. The ring width is fixed at $(r_2 - r_1)$ = 0.4mm. Note that each curve stops when the outer ring radius, r_2 is equal to half of the separation, i. e., when rings just touch each other. It is observed that the phase shift is mainly determined by the ring dimension. Small rings are capacitive and produce phase shifts greater than π, while large rings are inductive and produce phase shifts less than π. For a given phase shift, the closer the separation between adjacent rings, the smaller the median ring radius required. With 15mm separation, a phase shift in the range of $\pi/2$ to 2π can be obtained simply by adjusting the ring radius. In practice, the widths of the full wave zones of a zonal reflector are limited, so a smaller separation d should always be used whenever possible.

However, it is seen from Fig. 5.5 that for any required phase shift, there is a minimum separation d. The smaller the phase shift, the greater the minimum d. This means that the minimum dimension of the rings is limited by the required phase shift.

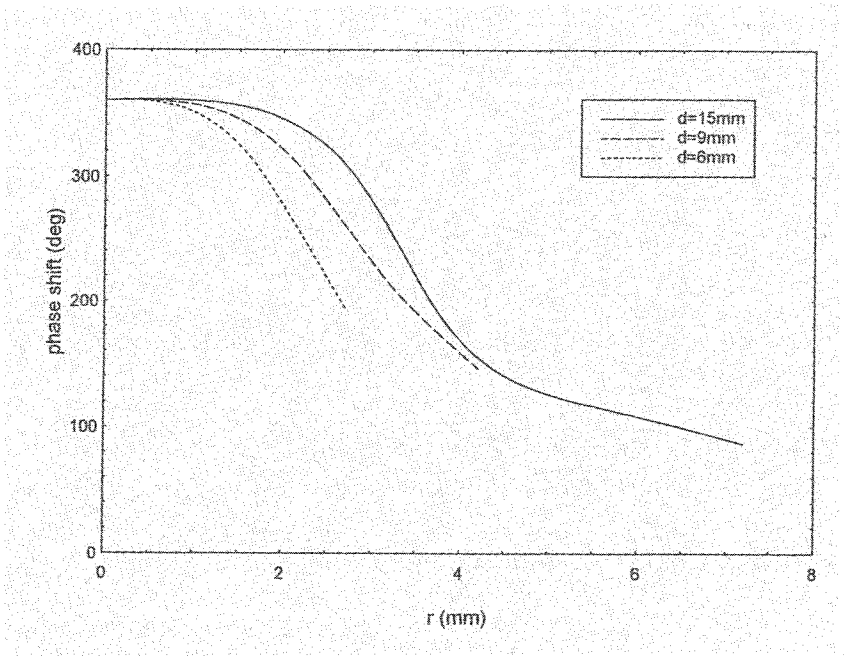

Fig. 5.5 Performance of reflective phase shifters with fixed substrate thickness and different distances between adjacent rings.

Fig. 5.6 gives the phase shifting performance of reflective phase shifters with d = 15mm and different substrate thickness, where the ring width is fixed at 0.4mm. It is seen that the three curves become very close at resonance when the ring circumference is roughly equal to the operating wavelength. This indicates that the resonant frequency of the array is not strongly influenced by the substrate thickness. The substrate thickness determines the initial phase shift and the gradient of the curves around resonance, but it does not influence the range of phase variation significantly.

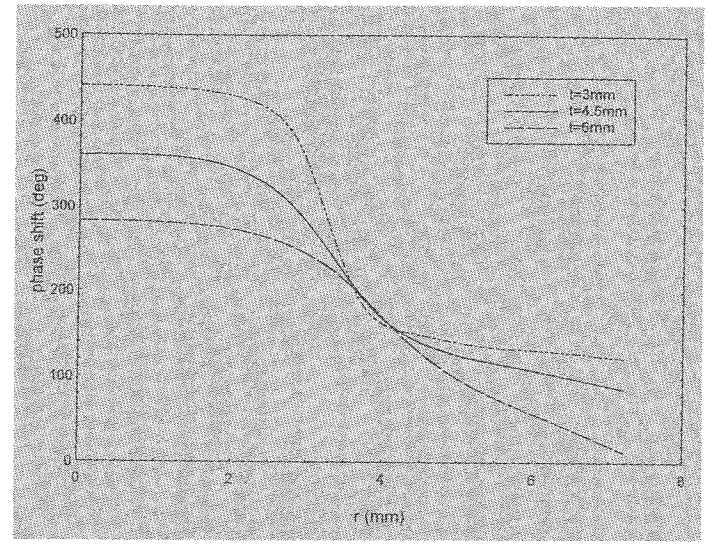

Fig. 5.6 Performance of the reflective phase shifters with fixed distance between adjacent rings and different substrate thickness.

5.3 Phase Correcting Flat Reflector Incorporating Rings

A homogeneous reflective phase shifter with a fixed substrate provides a specific phase shift at a given frequency. To obtain a phase correcting zoneplate reflector, a space-varying phase shifting function is required in order to focus an incoming plane wave at the focal point [41, 44-46]. Consequently, the conducting rings must be inhomogeneously distributed over the substrate surface. In theory, conducting rings in an inhomogeneous environment behave differently from those in a homogeneous array. Since a zoneplate reflector employs hundreds even thousands of conducting rings, however, a full numerical analysis will lead to unacceptable computer memory and CPU time. Therefore, the following approximate method is used instead. Firstly, a number of homogeneous phase shifters are designed to realise the discrete phase shifts required by the subzone phase correction technique described in the previous chapters. Then, rings of different sizes are uniformly packed in the appropriate subzones.

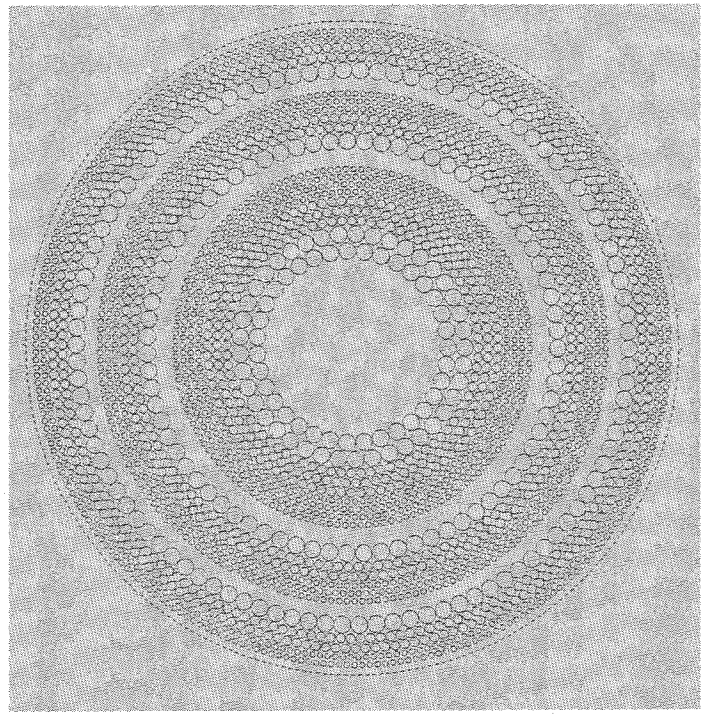

Fig. 5.7 Print-out of the quarter-wave single printed flat reflector.

As experimental prototypes, a number of small single printed phase correcting flat reflectors were fabricated and tested, which had only one full-wave zone and a 33.2cm diameter [17, 40]. Based on the success and experience gained, a larger quarter-wave flat reflector operating at 11.4GHz was designed and fabricated using the screen printing technique [18]. It has 59.4cm diameter and 0.8 *f/D* ratio. Three full wave zones and a quarter wave zone are covered by the reflector. The substrate has 5mm thickness and 2.08 permittivity. The first quarter-wave zone is left blank, which gives 17.3° phase shift to a normally incident plane wave. Three different size rings are printed in the other three quarter-wave zones to provide the following phase shifts: 107.3°, 197.3° and 287.3°. With the ring widths fixed at 0.4mm, the median ring radii are 7.4mm, 3.95mm and 2.35mm respectively. The printout of the ring arrangement is shown in Fig. 5.7. A corrugated conical

horn with 4.7cm aperture diameter was used as the feed and the whole system is shown in Fig. 5.8.

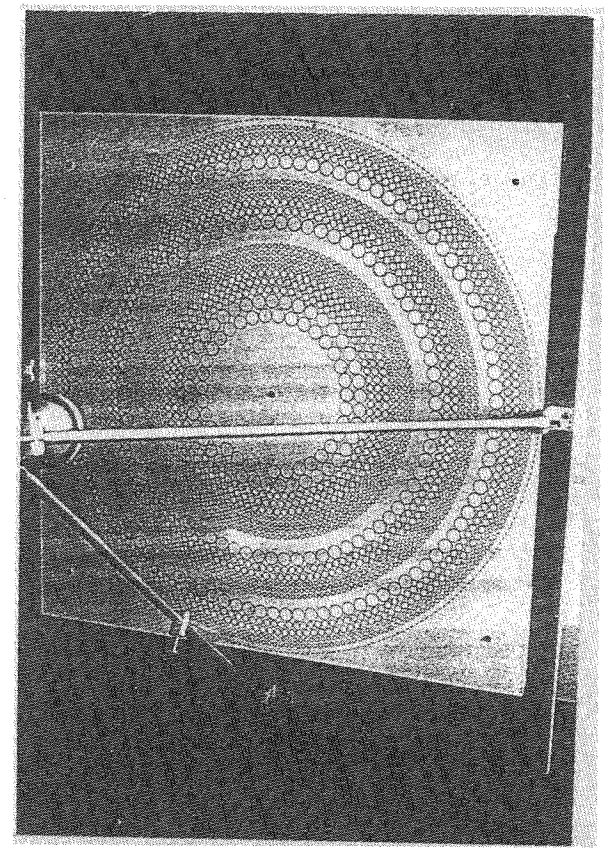

Fig. 5.8 Illustration of the antenna system.

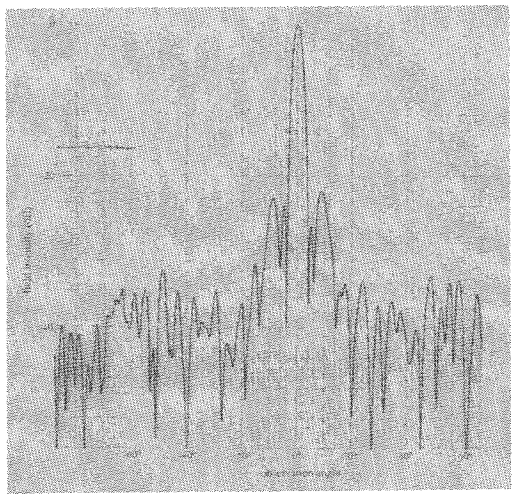

(a)

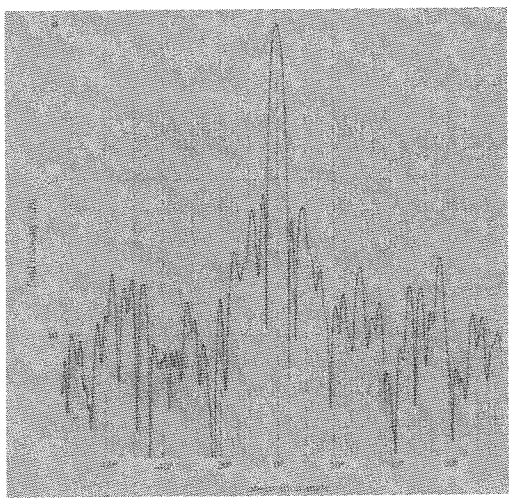

(b)

Fig. 5.9 E-plane radiation patterns of the single printed flat reflector shown in Fig. 5.8 at 10.9GHz (a) and 11.2GHz.

The antenna was measured in the band from 10.9GHz to 11.7GHz. Fig. 5.9 shows two E-plane radiation patterns of the antenna at 10.9 GHz and 11.2GHz respectively. It is seen that the close-in sidelobe level is about -22dB and the far-out sidelobes are below -30dB. Similar results were observed at other frequencies. As with the conventional dish, the sidelobe level can be further reduced if the non-blocking offset configuration is used. Fig. 5.10 shows the frequency response of the antenna and a 1.95dB maximum gain reduction was observed at the lower band edge. This yields an estimated 3dB bandwidth of greater than 10%, which agrees with the 12% bandwidth achieved with the small prototype [17]. The antenna achieved 43% maximum efficiency at the central design frequency.

5.4 Other Designs

It should be pointed out that, in addition to rings, conducting elements of various shapes can be used to produce the phase shifts required by a single printed flat reflector. Examples include patches, holes and dipoles etc.. Fig. 5.10 shows such a design by the authors using conducting discs and circular holes. The two complementary elements were employed to achieve capacitive and inductive conductance, respectively.

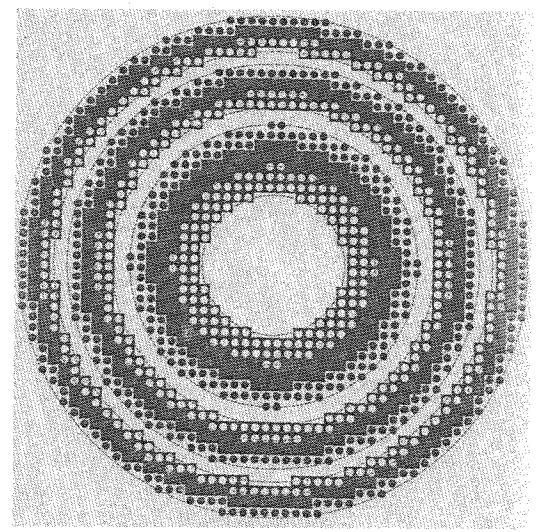

Fig. 5.10 An alternative design using discs and holes.

Malibu Research has developed a similar reflector antenna based on the crossed dipoles, which is known as FLAPS™ (Flat Parabolic Surface) [41]. The FLAPS™ consists of an array of crossed dipoles positioned approximately 1/8 wavelength above a ground plane and the phase shifting value was controlled by changing both the lengths of the dipoles and the spacing between adjacent elements (see Fig. 5.11). The dipole lengths vary from 0.25 to 0.6 wavelength to achieve a full range of phase shifts.

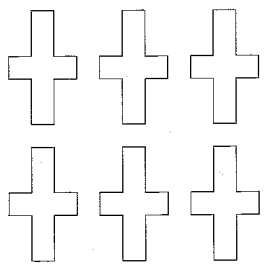

Fig. 5.11 Crossed dipoles used in FLAPS™.

An interesting aspect of the FLAPS™ antenna is that, owing to the polarisation isolation between the orthogonal dipoles (greater than 50dB), it is possible to control the two polarisations of the reflected wave independently. By designing the FLAPS™ surface to have separate focal points for the orthogonal linear polarisations, for instance, a dual polarised feed is not required. This characteristic can also be used in various applications, such as converting one linear polarisation to another or converting a linearly polarised wave to a circularly polarised one. Fig. 5.12 shows the FLAPS™ antenna configuration and Fig. 5.13 shows another possible arrangement of the crossed-dipoles [63].

5.5 Conclusions

In this chapter, the single printed flat reflector using reflective phase shifters is introduced. The spectral domain method of moments used for analysing reflective phase shifters with conducting rings is described, and experimental and numerical results are given. The theoretical model and

method can also be used in similar designs based on other phase shifting elements. A flat quarter-wave single printed flat reflector incorporating rings operating in the 11GHz band (10.9GHz to 11.7GHz) is investigated. The reflector covers three full wave zones and a quarter-wave zone. In each full wave zone, the first quarter-wave zone is left blank, the other three quarter-wave zones are packed with different size rings. The new reflector antenna achieved 43% maximum efficiency and -22dB sidelobe level. The 3dB bandwidth of the reflector is estimated to be greater than 10%. Also, two alternative designs, one based on patches and holes and the other the FLPAS™ antenna based on crossed-dipoles by Malibu Research, are discussed.

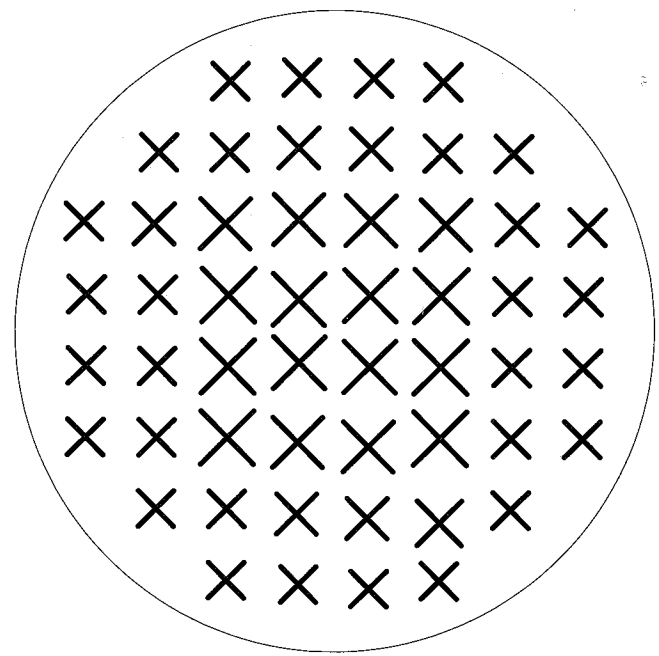

Fig. 5.12 Illustration of the element arrangement in FLAPS™

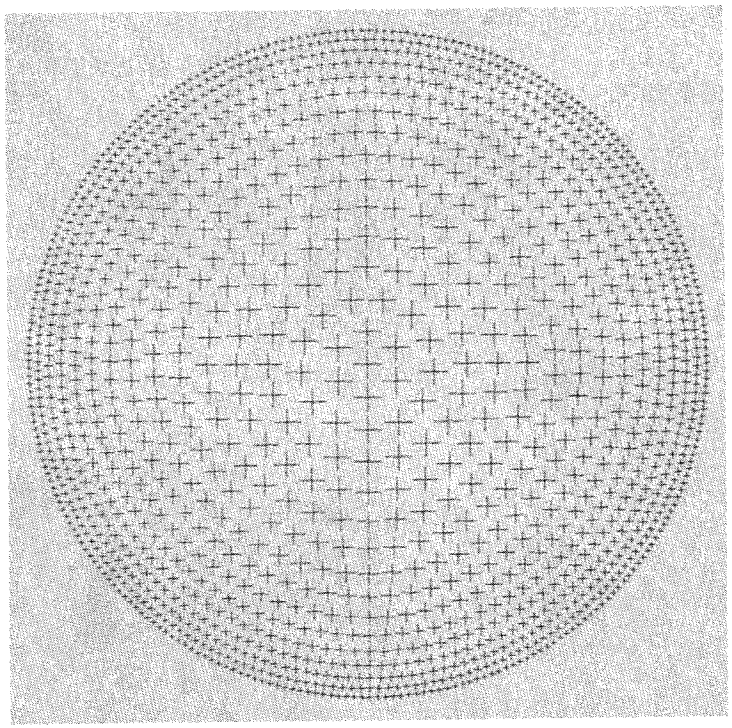

Fig. 5.13 Illustration of an alternative arrangement of crossed-dipoles as phase shifting elements. Microwave Engineering Europe.

Chapter 6 Reflective Array Antenna

In addition to various Fresnel zoneplate antennas, there is another type of electrically large antennas based on the principle of phase correction - the passive phase correcting array antenna, which consists of a regular array (Cartesian array, for instance) of phase shifting elements over a plane and a feed. In contrast to the normal array antenna which requires a feeding network, the elements in a phase correcting array are excited by the radiation field of the feed and the array radiation pattern is controlled by adjusting the phase shift or the surface impedance of each element in the array [47-50]. This type of antennas possesses the versatility of the conventional array antenna in that a variety of radiation patterns can be produced by changing the distribution of the phase correcting function across the antenna aperture. In principle, there are both reflective and transmissive arrays. This chapter is devoted to reflective arrays only, though the principle applies equally to transmissive arrays.

Reflective phase correcting arrays can be classified into two different categories. In the first, with elements whose phase shifts are chosen from a continuous range, each element provides a perfect phase correction at the element centre. To date, a few such antennas have been reported by previous investigators, including some very large ones used for astronomy [47, 50]. The second consists of quantised phase shifting elements [47, 48]. Similar to the stepped and zoned phase correcting reflectors, phase quantization errors exist at the centres of most elements [5, 13]. Although the phase efficiency of an array with quantised phase shifting elements is lower, it has the following advantages. First, the quantised phase shifting elements are more economical to produce. Second, a set of quantised phase shifting elements with fixed values forms a reconfigurable antenna kit with which planar reflectors of different performance can be conveniently built. Third, scanning can be achieved by using electronic digital phase shifters.

As with the Fresnel zoneplate antenna, the efficiency of the passive phase correcting array is a function of the illumination efficiency, the spillover efficiency and the phase efficiency etc. (see chapter 3). While the

others are related to the feed radiation pattern, the phase efficiency is mainly determined by the phase correcting function over the array aperture. In this chapter, a systematic investigation of the phase efficiency of planar reflective arrays is given [19]. Section 6.1 presents a general expression for the phase efficiency of the planar reflective phase correcting array. Section 6.2 deals with the phase correcting array with elements whose phase shifts are chosen from a continuous range. The relationship among the phase efficiency, the element size and the focal length to diameter ratio is discussed. In section 6.3, the phase correcting array with quantised phase shifting elements is studied. The probability theory is employed to investigate the influence of the quantised phase errors on the phase efficiency. Section 6.4 gives an estimate of the influence of manufacturing and installation tolerance. Section 6.5 presents a new reflective array with multilayer phase shifting tiles and section 6.6 concludes the chapter.

6.1 Phase Efficiency of a Reflective Array

As shown in chapter 3, the phase efficiency of a phase correcting aperture antenna can be studied through the focal field. Assume a plane wave is normally incident on a planar reflective surface placed at $z = 0$ plane (see Fig. 6.1), the diffracted field at the chosen focal point can be expressed as

$$\Psi_f = \frac{jk}{4\pi}\int \exp\{j[\Phi(x,y) - kR]\}(1+\frac{f}{R})\frac{1}{R}dxdy \tag{6.1}$$

where $\Phi(x, y)$ is the surface phase correcting function, f is the focal length, $k = \frac{2\pi}{\lambda}$ is the wavenumber in free space and $R = \sqrt{f^2 + x^2 + y^2}$. The phase efficiency of the phase correcting surface is defined as

$$\eta_p = \frac{\Psi_f \Psi_f^*}{\Psi_{fo}\Psi_{fo}^*} \tag{6.2}$$

where the asterisk denotes complex conjugate and Ψ_{fo} is the focal field of the ideally phase corrected surface whose phase correcting function satisfies

$$\Phi(x,y) = kR. \tag{6.3}$$

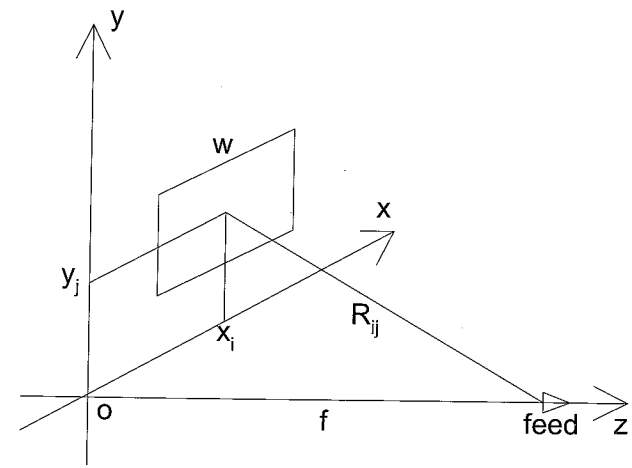

Fig. 6.1 Illustration of the co-ordinates.

In practice, it is very difficult to achieve the continuous phase correction given by Eq. (6.3), but a good approximation can be obtained by using a large number of discrete phase shifting elements, which forms the basis of the phase correcting array. When square elements are employed, the phase correcting function of a phase correcting array can be expressed as

$$\Phi(x,y) = \sum_{i,j} \Phi_{ij}\, rect(\frac{x - x_i}{w})rect(\frac{y - y_j}{w}) \tag{6.4}$$

where

$$x_i = iw$$
$$y_j = jw$$

with w as the element width (see Fig. 6.1) and $rect(u)$ defined as

$$rect(u) = \begin{cases} 1 & (u \le 1/2) \\ 0 & otherwise \end{cases}.$$

Substituting Eq. (6.4) into Eq. (6.1) yields

$$\Psi_f = \frac{jk}{4\pi}\sum_{i,j}\int_{S_{ij}} \exp\{j[\Phi_{ij} - kR]\}(1+\frac{f}{R})\frac{1}{R}dxdy \tag{6.5}$$

where S_{ij} is the aperture area of the element (i, j). To obtain an explicit expression of the focal field, one introduces a local co-ordinate system *x'o'y'* as follows:

$$x' = x - x_i$$
$$y' = y - y_j$$

This leads to

$$R = \sqrt{f^2 + (x'+x_i)^2 + (y'+y_j)^2}\ .$$

Expanding R into a Taylor series and neglecting the higher order terms produces

$$R \approx R_{ij} + \frac{x_i x' + y_j y'}{R_{ij}} \tag{6.6}$$

where R_{ij} is the distance between the element centre and the focal point given by

$$R_{ij} = \sqrt{f^2 + x_i^2 + y_j^2}\ . \tag{6.7}$$

Assuming that the element size is much smaller than the focal length, i.e., $w<<f$, one can neglect the variation of the amplitude of the integrand in Eq. (6.5) and substitute Eq. (6.6) into the phase term. This gives

$$\Psi_f \approx \frac{jk}{4\pi}\sum_{i,j} C_{ij}\int_{S_{ij}} exp(-jk\frac{x_i x' + y_j y'}{R_{ij}})\exp[j(\Phi_{ij} - kR_{ij})]dx'\,dy' \tag{6.8}$$

where

$$C_{ij} = (1+\frac{f}{R_{ij}})\frac{1}{R_{ij}}\ . \tag{6.9}$$

Performing the integration in Eq. (6.8) yields

$$\Psi_f = \frac{jkw^2}{4\pi}\sum_{i,j} C_{ij}E_{ij}\exp[j(\Phi_{ij} - kR_{ij})] \tag{6.10}$$

where

$$E_{ij} = \mathrm{sinc}(\sin\theta_{ij}\cos\phi_{ij}\frac{w}{\lambda})\mathrm{sinc}(\sin\theta_{ij}\sin\phi_{ij}\frac{w}{\lambda}) \tag{6.11}$$

with

$$\theta_{ij} = \tan^{-1}(\sqrt{x_i^2 + y_j^2}/f) \tag{6.12.a}$$

$$\varphi_{ij} = \tan^{-1}(y_j / x_i) \tag{6.12.b}$$

$$\mathrm{sinc}(x) = \frac{\sin(\pi x)}{\pi x}\ . \tag{6.12.c}$$

Similarly, the focal field of an ideally phase corrected surface can be well approximated as

$$\Psi_{fo} \approx \frac{jkw^2}{4\pi}\sum_{i,j} C_{ij}\ . \tag{6.13}$$

Substituting Eqs. (6.10) and (6.13) into Eq. (6.2) gives

$$\eta_p = \frac{\sum_{i,j}\sum_{i',j'} C_{ij}C_{i'j'}E_{ij}E_{i'j'}\exp[j(\Phi_{ij} - kR_{ij})]\exp[j(kR_{i'j'} - \Phi_{i'j'})]}{\sum_{i,j}\sum_{i',j'} C_{ij}C_{i'j'}}\ . \tag{6.14}$$

E_{ij} represents the contribution of the element (i, j). It needs modification when the element aperture field is not a constant, such as the waveguide modes used in [47]. For convenience, define the *element efficiency* as

$$\eta_{ij} = E_{ij}^2$$

$$= \mathrm{sinc}^2(\sin\theta_{ij}\cos\phi_{ij}\frac{w}{\lambda})\mathrm{sinc}^2(\sin\theta_{ij}\sin\phi_{ij}\frac{w}{\lambda}). \quad (6.15)$$

From Eq. (6.15), it is seen that the element efficiency varies with the element position and size.

6.2 Arrays with Ideal Phase Shifting Elements

When element phase shift values are in the range of (0, 2π), the phase shift of element (i, j), Φ_{ij}, can be chosen to correct the spherical phase error at the element centre completely, i.e.,

$$\phi_{ij} = kR_{ij} - 2l\pi \quad (6.16)$$

where l is an integer to ensure

$$0 \le \phi_{ij} \le 2\pi. \quad (6.17)$$

Substituting Eq. (6.16) into Eq. (6.14) produces

$$\eta_{pc} = \frac{\sum_{i,j}\sum_{i',j'} C_{ij}C_{i'j'}E_{ij}E_{i'j'}}{\sum_{i,j}\sum_{i',j'} C_{ij}C_{i'j'}}. \quad (6.18)$$

Eq. (6.11) shows that E_{ij} is a function of θ_{ij} and ϕ_{ij}. When $kw\sin\theta_{ij} < \pi$, which is normally the case for an array with reasonable phase efficiency, E_{ij} is almost independent of ϕ_{ij}, so one can write

$$\eta_{ij} \approx \mathrm{sinc}^2(\sin\theta_{ij}\frac{w}{\lambda}). \quad (6.19)$$

Numerical results showed that this approximation leads to a relative error of less than 1%. Eq. (6.19) shows that for a given element size w, the element efficiency decreases with increasing θ_{ij}. For an array circumscribed by a circle with diameter D, which can be taken as a circular reflector with zigzag boundaries, the outermost elements span the maximum angle θ_{ij}. Therefore,

$$\eta_{pc} > \mathrm{sinc}^2(\frac{w}{\lambda\sqrt{1-4\alpha^2}}) \quad (6.20)$$

where $\alpha = f/D$ is the focal length to diameter ratio of the circular reflector. It was shown in Chapter 3 that the phase efficiency of a $1/M$-wave phase correcting zoneplate is given by

$$\eta_{1/M} = \mathrm{sinc}^2(\frac{1}{M}). \quad (6.21)$$

To obtain the same phase efficiency for the phase correcting array, a sufficient condition is

$$w \le \frac{\lambda\sqrt{1+4\alpha^2}}{M}. \quad (6.22)$$

Eq. (6.22) ensures that the array phase efficiency is greater than that of the corresponding $1/M$-wave zoneplate, i.e.

$$\eta_{pc} > \mathrm{sinc}^2(\frac{1}{M}). \quad (6.23)$$

Fig. 6.2 shows the phase efficiency of three reflective arrays with the same aperture diameter ($D = 40\lambda$) but different focal length to diameter ratio α and different element size w/λ. It is seen that the phase efficiency of a planar reflective array with element phase shift values in the range [0, 2π] is determined by the focal length to diameter ratio and the element size. The greater the α and the smaller the w/λ, the greater the phase efficiency. The maximum element size which guarantees a given array phase efficiency increases with the focal length to diameter ratio of the array. Numerical results show that with the same focal length to diameter ratio α and the same

element size w/λ, the phase efficiency hardly changes with the array diameter D.

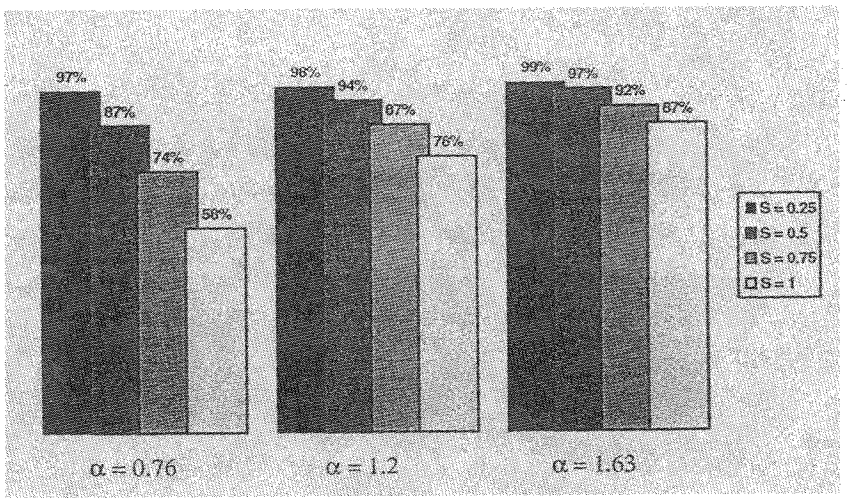

Fig. 6.2 Phase efficiency of arrays with element phase shifts in a continuous range. $d = 40\lambda$, $\alpha = f/D$ and $S = w/\lambda$.

6.3 Arrays with Quantised Phase Shifting Elements

Although arrays with element phase shifting values chosen from a continuous range have higher phase efficiency, those with quantised phase shifting elements are much easier and more economical to produce. Furthermore, the same set of quantised phase shifting elements can be employed to build different planar reflectors operating in the same band. In other words, reflectors with different performance can be produced by rearranging the positions of the elements.

When quantised phase shifting elements are employed, Φ_{ij} is restricted to such discrete values as

$$\Phi_{ij} = \frac{2n\pi}{N} \qquad (n = 0, 1, ..., N-1) \qquad (6.24)$$

where N is referred to as the *phase quantization number*. For a specific element centred at (x_i, y_j), n is so chosen that there is an integer m leading to

$$\left|\Phi_{ij} + 2m\pi - kR_{ij}\right| \le \frac{\pi}{N}. \qquad (6.25)$$

Eq. (6.25) demands that, modulo-2π, the phase error at the centre of element (i, j) is less than π/N. Defining the *phase quantization error* as

$$\delta\Phi_{ij} = \Phi_{ij} + 2m\pi - kR_{ij}, \qquad (6.26)$$

Eq. (6.14) becomes

$$\eta_{pq} = \frac{\sum_{i,j}\sum_{i',j'} C_{ij}C_{i'j'}E_{ij}E_{i'j'}\exp[j(\delta\Phi_{ij} - \delta\Phi_{i'j'})]}{\sum_{i,j}\sum_{i',j'} C_{ij}C_{i'j'}}. \qquad (6.27)$$

For an array with given parameters: focal length f, element size w, phase quantization number N and operating wavelength λ, the distribution of $\delta\Phi_{ij}$ is deterministic. To obtain a general understanding of the influence of the phase quantization error $\delta\Phi_{ij}$ on the antenna phase efficiency, however, it is assumed that $\delta\Phi_{ij}$ is an independent random variable with a uniform probability distribution. In other words, $\delta\Phi_{ij}$ can take any value in the range of $(-\frac{\pi}{N}, \frac{\pi}{N})$ with equal probability, depending on the relative position of the element to the focal point. Integrating Eq. (6.27) with a uniform probability density function (pdf) gives the expected value of the phase efficiency:

$$(\eta_{pq})_E = \left|\overline{\exp(j\delta\Phi)}\right|^2 \eta_{pc} + (1 - \left|\overline{\exp(j\delta\Phi)}\right|^2)\frac{\sum_{i,j} C_{ij}^2\eta_{ij}}{\sum_{i,j}\sum_{i',j'} C_{ij}C_{i'j'}} \qquad (6.28)$$

where $\overline{\exp(j\delta\Phi)}$ is the mean of $\exp(j\delta\Phi)$, which is the same for all the elements according to the above assumption. Eq. (6.28) shows that the

expected phase efficiency has a dominant term proportional to the phase efficiency of the phase correcting array with element phase shifts chosen from a continuous range. The coefficient is the square magnitude of the mean of a unit vector, whose phase is the element phase error.

With the rectangular distribution as the pdf of $\delta\Phi$ [51, 52], one has

$$\left|\overline{\exp(j\delta\Phi)}\right|^2 = \mathrm{sinc}^2(\frac{1}{N}). \tag{6.29}$$

Substituting Eq. (6.29) into Eq. (6.28) gives

$$(\eta_{pq})_E = \mathrm{sinc}^2(\frac{1}{N})\eta_{pc} + (1-\mathrm{sinc}^2(\frac{1}{N}))\frac{\sum_{i,j} C_{ij}^2\eta_{ij}}{\sum_{i,j}\sum_{i',j'} C_{ij}C_{i'j'}}. \tag{6.30}$$

By virtue of Eq. (6.9), it can be proved that

$$\frac{\sum_{i,j} C_{ij}^2\eta_{ij}}{\sum_{i,j}\sum_{i',j'} C_{ij}C_{i'j'}} < \frac{(C_{ij})^2_{\max}}{K_A(C_{ij})^2_{\min}} < \frac{4(R_{ij})^2_{\max}}{K_A f^2} \tag{6.31}$$

where $(R_{ij})_{\max}$ is the maximum distance between the focal point and the element centre, and K_A is the number of elements in the array. For a practical array, K_A is normally very large and

$$\frac{4(R_{ij})^2_{\max}}{K_A f^2} << 1, \tag{6.32}$$

so the second term in Eq. (6.30) is negligible. This gives

$$(\eta_{pq})_E \approx \mathrm{sinc}^2(\frac{1}{N})\eta_{pc}. \tag{6.33}$$

Substituting Eq. (6.20) into Eq. (6.33) produces

$$(\eta_{pq})_E > \mathrm{sinc}^2(\frac{1}{N})\mathrm{sinc}^2(\frac{w}{\lambda\sqrt{1-4a^2}}). \tag{6.34}$$

The physical explanation of Eq. (6.34) is given as follows. The phase efficiency of the quantised phase correcting array is a function of the phase quantization number N, the element size w and the focal length to diameter ratio α. The phase quantization number determines the mean phase error at each element centre, and the element size and the focal length to diameter ratio determine the maximum phase variation across the element. Therefore, greater quantization number and focal length to diameter ratio, and smaller element size are favourable to produce a reflective phase correcting array with higher efficiency. Since a quantised phase correcting array can be taken as a device to simulate a subzone phase correcting Fresnel zoneplate described in chapter 3, this is quite understandable.

Based on Eq. (6.27), Fig. 6.3 shows the phase efficiencies of reflective arrays with a phase quantization number $N = 5$. The other array parameters are kept the same as those for Fig. 6.2. Numerical results showed that these phase efficiency values are almost identical with the expected values given by Eq. (6.33), with errors less than 1%. Therefore, one can conclude that for a phase correcting array with N different types of phase shifting elements, the phase quantization error reduces the phase efficiency by a factor of $\mathrm{sinc}^2(1/N)$.

It should be pointed out that both Fig. 6.3 and Fig. 6.4 indicate that the phase efficiency of a reflective array antenna increases when the element size w/λ decreases. In a practical design, however, the element size may affect the distribution of the electromagnetic fields. When the multilayer tiles as described in section 6.5 are used, for instance, the edge diffraction degrades the effect of phase compensation if the element size is smaller than the wavelength. In this case, a large f/D ratio may have to be used to accommodate large array elements.

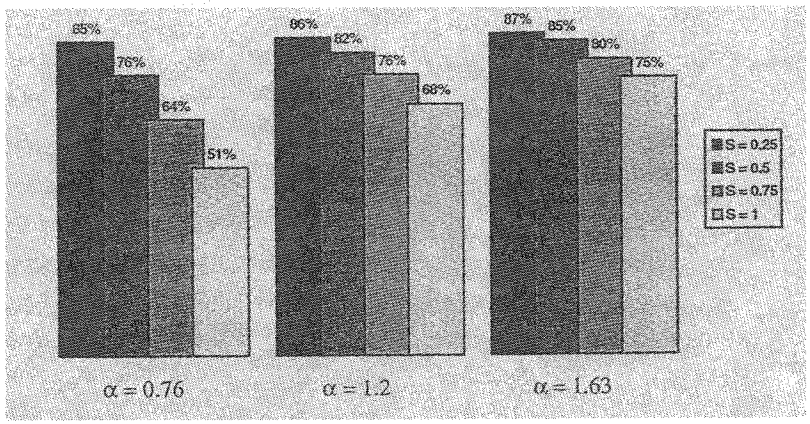

Fig. 6.3 Phase efficiency of arrays with element phase shifts of quantised values. N = 5, d = 40λ, α = f/D and S = w/λ.

6.4 Tolerance Analysis

Once the parameters of the reflective array with ideal quantised phase shifters are given, which include the focal length, operating wavelength, quantization number and element size, the distribution of the phase quantization error $\delta\Phi_{ij}$ is deterministic. When the manufacturing and installation tolerance is considered, however, $\delta\Phi_{ij}$ becomes a genuine random variable. To distinguish the random phase error caused by the tolerance from the deterministic phase quantization error, replace Eq. (6.27) by

$$\eta_{pqr} = \frac{\sum_{i,j}\sum_{i',j'} C_{ij}C_{i'j'}E_{ij}E_{i'j'}\exp[j(\delta\Phi_{ij}-\delta\Phi_{i'j'})]\exp[j(\delta\Phi_{rij}-\delta\Phi_{ri'j'})]}{\sum_{i,j}\sum_{i',j'} C_{ij}C_{i'j'}} \tag{6.35}$$

where $\delta\Phi_{ij}$ is the phase quantization error defined in Eq. (6.26) and $\delta\Phi_{rij}$ is the random phase error. To quantify the influence of the manufacturing and installation tolerance on the array phase efficiency, assume that the random

phase errors at different elements are independent of each other, but have the same pdf. Integrating Eq. (6.35) with the pdf gives the expected value of the phase efficiency:

$$(\eta_{pqr})_E = \left|\overline{\exp(j\delta\Phi_r)}\right|^2 \eta_{pq} + (1-\left|\overline{\exp(j\delta\Phi_r)}\right|^2)\frac{\sum_{i,j} C_{ij}^2\eta_{ij}}{\sum_{i,j}\sum_{i',j'} C_{ij}C_{i'j'}} \tag{6.36}$$

where $\overline{\exp(j\delta\Phi_r)}$ is the mean of $\exp(j\delta\Phi_r)$, which is the same for all the elements according to our assumption. Taking the normal distribution as the pdf of $\delta\Phi_r$ yields

$$\left|\overline{\exp(j\delta\Phi_r)}\right|^2 = \exp(-\sigma_\Phi^2) \tag{6.37}$$

where σ_Φ is the standard deviation of the random phase error $\delta\Phi_r$ [7, 8]. Substituting Eq. (6.37) into Eq. (6.36) and neglecting the second term, as with Eq. (6.28), gives

$$(\eta_{pqr})_E \approx \exp(-\sigma_\Phi^2)\eta_{pq} \tag{6.38}$$

Eq. (6.38) shows that the manufacturing tolerance is expected to reduce the phase efficiency of the quantised phase correcting array by a factor of $\exp(-\sigma_\Phi^2)$. This result is the same as that for conventional arrays and reflectors [53]. In contrast to the quantization phase error, the distribution of $\delta\Phi_{rij}$ is usually unknown, so the only way to ensure a required phase efficiency is to control the manufacturing tolerance.

6.5 Arrays with Multilayer Tiles

To put the concept of the phase correcting array into practice, multilayer phase correcting tiles can be used as the phase correcting elements. Fig. 6.4 shows a set of four different phase shifting tiles based on the multilayer configuration. The tiles are composed of three identical pieces of dielectric substrates and a conducting film located at different positions, where the film thickness has been exaggerated for the purpose of illustration. Type-1 tile is the reference tile which has a conducting film on the top and

provides π phase shift. The conducting films are moved down successively in type-2 to type-4 tiles in order to provide quantised phase shifts by using different numbers of dielectric substrates above the conducting film. When a ray is normally incident on the type-p tile, it produces a geometrical optics (G. O.) phase shift given by

$$\varphi_p^t = \pi - 2k(p-1)t\sqrt{\varepsilon_r} \qquad (p = 1, 2, ..., 4) \tag{6.39}$$

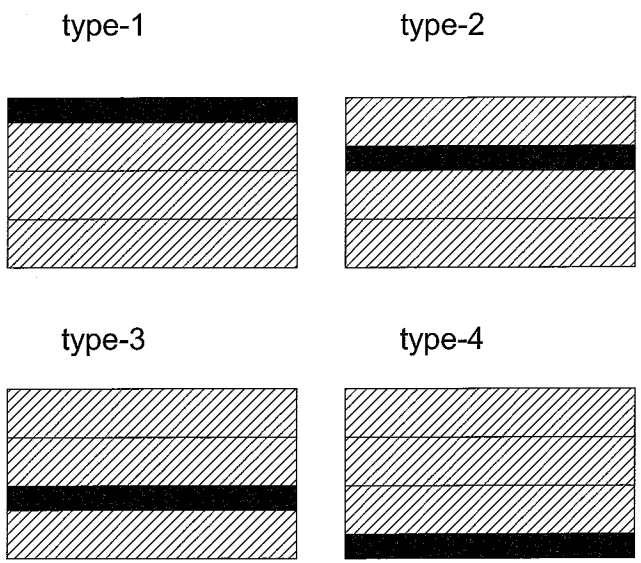

Fig. 6.4 Sectional view of the multilayered tiles.

where t is the thickness of the dielectric substrates and ε_r is the relative dielectric constant. With $N = 4$ as the quantization number, one obtains

$$t = \frac{\lambda}{8\sqrt{\varepsilon_r}}. \tag{6.40}$$

The whole tile thickness is given by

$$h = \frac{\lambda}{2\sqrt{\varepsilon_r}}. \tag{6.41}$$

Based on some preliminary experiments on small size laboratory prototypes [19, 47, 48], a working reflective array antenna with four types of multilayer tiles was fabricated in the University of Bradford workshop. The antenna was designed at 11.4GHz, with D = 0.8m and f = 1.064m, leading to f/D = 1.33. In order to use as large tiles as possible, this f/D ratio is greater than that of a normal dish. The offset angle of the array was chosen as 20°. The parameters for the tiles are ε_r = 2.01, tile width w = 25mm and tile thickness t = 2mm. Fig. 6.5 shows the layout of the tiles. The feed horn used for the antenna was a conical horn with a 52mm diameter. The antenna was tested at the Baldock Satellite Test Site by Mr T. M. Wright of Mawzones.

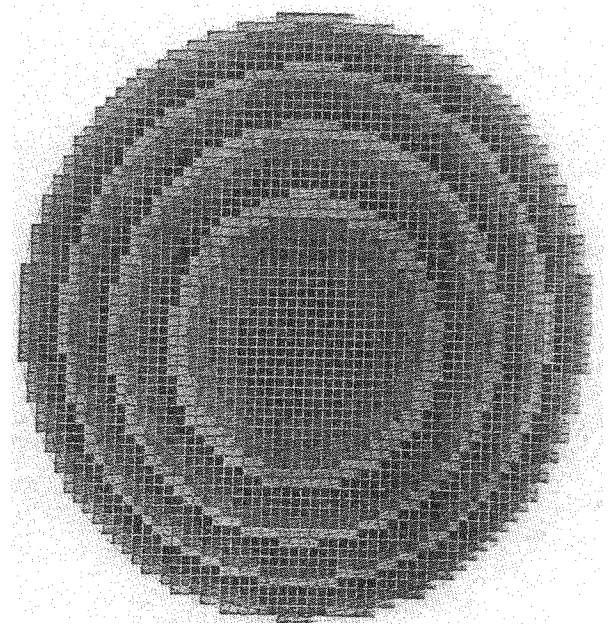

Fig. 6.5 Tile arrangement of the experimental array.

For economical reasons, the experiment was designed mainly to demonstrate the feasibility of the design, which consisted of the following

procedures. First, the strength of a beacon signal from a satellite received using a multilayer quarter-wave zoneplate was recorded. Then, the beacon signal strength received using the reflector array with multilayer tiles was recorded. The two recorded beacon signals are shown in Fig. 6.6 and Fig. 6.7. Comparing the two signals, it is seen that the signal picked up by the array antenna was by average 3dB stronger than that received by the quarter-wave zoneplate. Knowing that the zoneplate has 59cm diameter and 30° offset angle, the difference in the areas of the two antennas projected in the main direction accounts for about 2.29dB gain difference, thus resulting in about 0.7dB improvement in total efficiency. Although the experiment was not meant to produce any quantitative antenna performance measure, it is safe to conclude that an efficient reflective array antenna can be produced by using quantised phase shifting elements, such as multilayer tiles.

6.6 Conclusions

A systematic theory on the phase efficiency of planar reflective array antennas is given. Arrays with element phase shifts chosen from both continuous and quantised ranges are studied and closed-form equations for predicting the phase efficiency have been derived. The relationship among the phase efficiency, element size and focal length to diameter ratio is discussed. It is shown that for arrays with element phase shifts chosen from a continuous range, the phase efficiency is mainly determined by the element size and focal length to diameter ratio; whereas for arrays with quantised phase shifting elements, the element size, focal length to diameter ratio and quantization number altogether determine the phase efficiency. The influence of the manufacturing and installation tolerance is also quantified. The theory has been demonstrated by a working reflective array antenna with multilayer dielectric tiles.

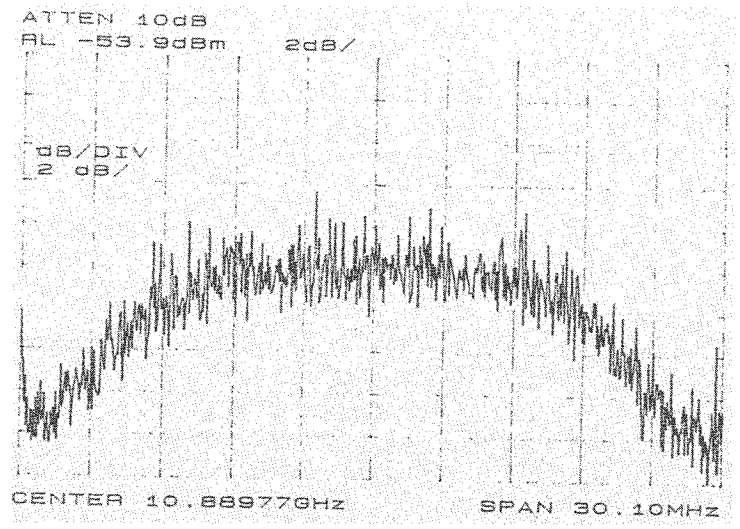

Fig. 6.6 Measured signal strength with a quarter-wave Fresnel zoneplate reflector.

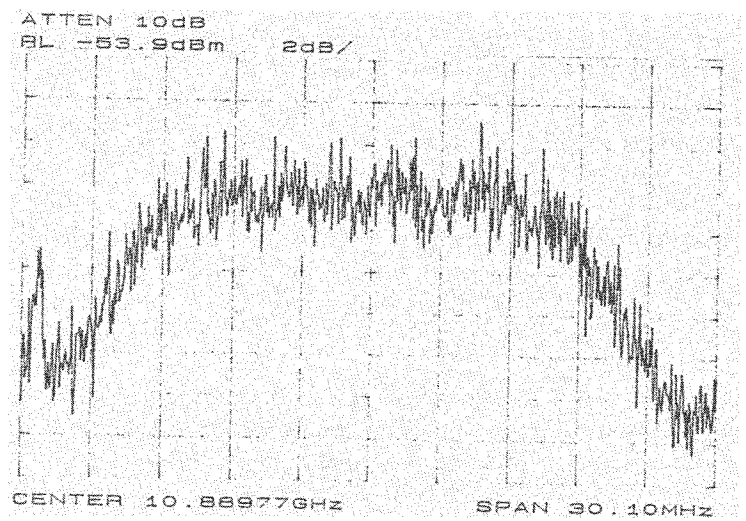

Fig. 6.7 Measured signal strength with the reflective phase correcting array.

Chapter 7

Other Fresnel Zone Antennas

In the preceding chapters, theoretical investigations and experiments on a number of Fresnel zone antennas are presented. This chapter is intended to introduce a wider range of Fresnel zone antennas. Section 7.1 presents a theory regarding the possibility of producing single printed Fresnel lens that doubles the efficiency of the simple Fresnel lens (transmission zoneplate). The rest of the chapter is devoted to other Fresnel zone antenna configurations published in the open literature by other researchers in the field. Readers who are interested in the application of Fresnel zone concept in different fields are recommended to refer to [65] for a comprehensive review.

7.1 Single Printed Fresnel Lens

Owing to the blockage caused by the conducting rings of the simple Fresnel lens (or transmission zoneplate) as discussed in chapter 2 and chapter 3, its antenna efficiency is intrinsically low, which limits its wide use in many practical applications. In the following, it is shown that it is theoretically possible to produce a single printed Fresnel lens of higher efficiency by replacing the opaque half-wave zones with conducting phase shifting elements.

Assuming a plane wave is normally incident on an infinitely thin homogeneous lossless screen, the reflection coefficient Γ and the transmission coefficient T satisfy the following equations:

$$1 + \Gamma = T \tag{7.1a}$$

$$|\Gamma|^2 + |T|^2 = 1 \tag{7.1b}$$

Eq. (7.1a) is derived from the electromagnetic boundary condition which demands the tangential component of the electric field to be continuous across the screen, and Eq. (7.1b) results from the law of energy conservation. To investigate the phase and manitude characteristics of the reflection coefficient Γ and the transmission coefficient T, let

$$\Gamma = \gamma e^{j\psi} \tag{7.2}$$

Substituting Eq. (7.2) into Eq. (7.1) yields

$$\Gamma = -\cos\psi e^{j\psi} \tag{7.3a}$$

$$T = -j\sin\psi e^{j\psi}. \tag{7.3b}$$

Eq. (7.3) shows that the reflection coefficient has a non-positive real part and the transmission coefficient has a non-negative real part. Therefore, the phase of the reflected and transmitted waves can be changed only in a range of π.

In a simple Fresnel lens, the phase deviation in the transparent half-wave zones is not compensated. Owing to the relationship between the phase and the magnitude in the transmission coefficient given in Eq. (7.3b), however, it does not help to employ phase correcting elements in the otherwise transparent half-wave zones, as the effect of compensating for the phase error would be offset by the reflection loss. It should be realised, however, that in a Fresnel lens the energy intercepted by the opaque half-wave zones is completely wasted. It is, therefore, possible to increase the efficiency of the Fresnel lens by replacing the opaque half-wave zones with phase shifting elements. The contribution from a transparent half-wave zone is given by

$$I_1 = \int_0^{\pi} e^{-j\psi} d\psi = -2j \tag{7.4}$$

Using Eq. (7.3b), the contribution from the phase correcting half wave zone is given by

$$-j\int_{\pi}^{2\pi} \sin\psi e^{j\psi} e^{-j\phi} d\phi \tag{7.5}$$

Let

$$\psi = \phi + \pi \tag{7.6}$$

Eq. (7.5) yields

$$I_2 = -j\int_{\pi}^{2\pi} \cos\phi d = -2j \tag{7.7}$$

The efficiency of the Fresnel zone lens consisting of transparent half-wave zones and phase correcting half-wave zones is thus given by

$$\eta = \frac{|I_1 + I_2|^2}{4\pi^2} = \frac{4}{\pi^2}. \tag{7.8}$$

Eq. (7.10) shows that a single printed Fresnel lens can achieve 40.5% efficiency, the same as that of an ideal phase reversal Fresnel zone reflector, provided that the phase shifting property given in Eq. (7.6) can be realised. As an illustration, a Fresnel zone lens of such configuration with two full wave zones is shown in Fig. 7.1.

7.2 Millimetre-Wave Dielectric Fresnel Lens

To increase the antenna efficiency of the Fresnel zone lens further, dielectric material of different thickness or permittivity can be used in different subzones to form Fresnel phase correcting lens antennas [5]. The concept behind these configurations is similar to that described in Chapter 3 and Chapter 4 on Fresnel zone reflector antennas.

The first quarter-wave Fresnel lens was reported in [5], which employed the same dielectric material but different thickness in each quarter-wave zone. One advantage of using this grooved structure is that any material with reasonable permittivity and low loss can be used. An alternative structure is to use composite dielectric material of the same

thickness but different permittivity [55]. For illustration, a full wave zone of such configuration is shown in Fig. 7.2. This configuration has the advantage that both the front and back surfaces of the lens are flat. In practice, however, it may be difficult to obtain all the material needed for a chosen frequency, so using composite material to make high efficiency Fresnel lens antenna may prove inconvenient, although the antenna efficiency of the Fresnel lens antenna using composite material can be higher than that of the grooved configuration [63]. It should be noted that neither configuration avoids the reflection loss incurred at the interface between the air and the dielectric.

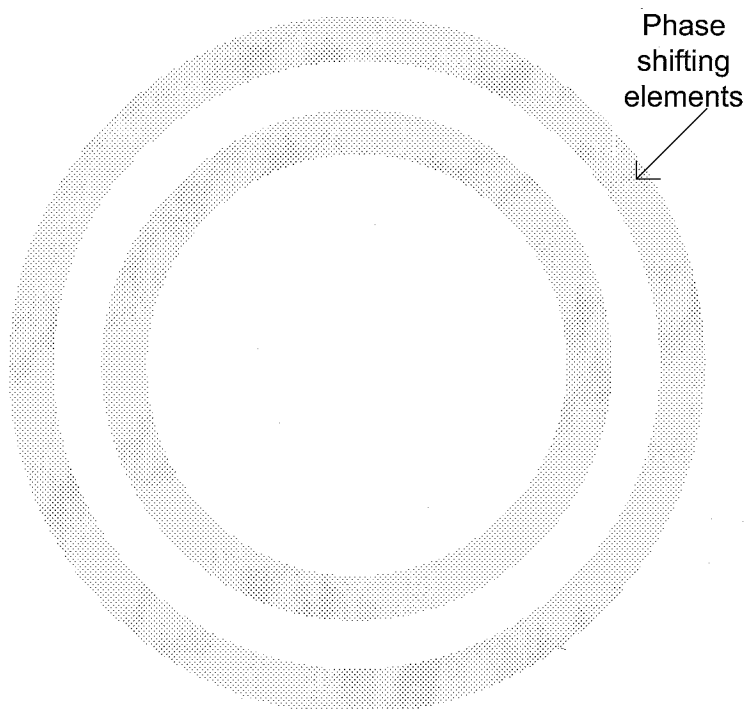

Fig. 7.1 A speculative single printed Fresnel lens.

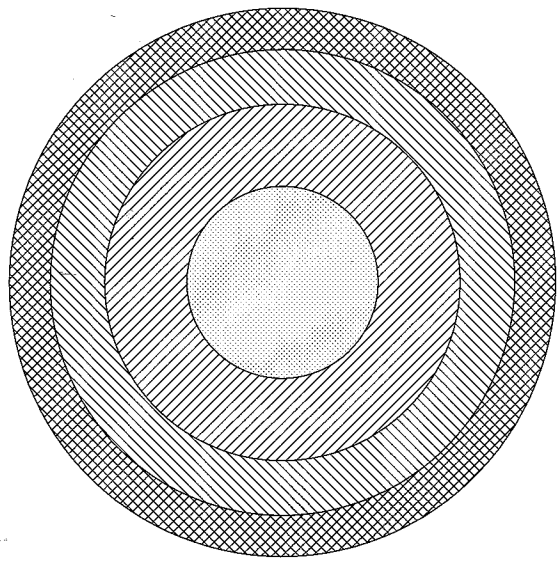

Fig. 7.2 The first full wave zone of a quarter-wave Fresnel dielectric lens.

7.3 Phase Correcting Lens Employing Artificial Dielectric

In principle, high efficiency and low cost phase correcting Fresnel lens antennas can be produced using the same concept given in Chapter 3 for reflector antennas. Unlike the reflector antenna, however, an ideal lens should provide not only effective phase correction to an incident wave but also good impedance matching so that the reflection loss can be kept small. Therefore, a multi-layer structure is inevitably needed to produce a high efficiency Fresnel lens antenna. This is similar to the concept of producing flat phase correcting lens employing non-homogeneous artificial dielectric. As an illustration, Fig. 7.3 shows a multi-beam phase correcting lens antenna considered by the European Space Agency (ESA) [63].

Employing artificial dielectric in lens antennas is potentially attractive. Compared with normal dielectric material, artificial dielectric has the advantage of lighter weight, higher thermal stability and strength, and the flexibility of synthesising any desired permittivity. Furthermore, artificial

material can be cheaply produced by printing conducting elements on low loss substrates. Better still, it may even be possible to produce a phase correcting lens antenna using non-homogeneous conducting polymers, a new kind of material which allows different degrees of conductivity to be synthesised [63].

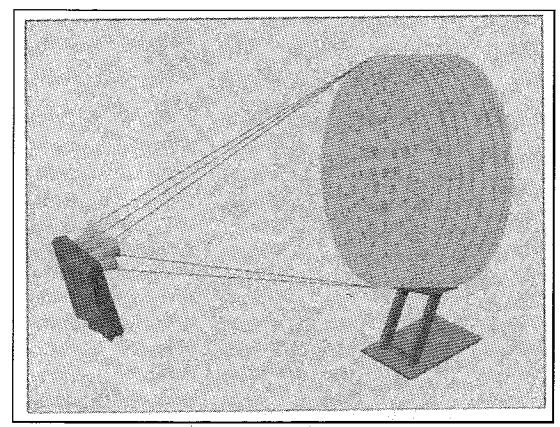

Fig. 7.3 A multilayer phase correcting lens antenna considered by ESA. Microwave Engineering Europe

7.4 Waveguide Lens

A waveguide lens based on the Fresnel zone antenna concept has been used as a satellite-borne antenna (see Fig. 7.4). It consists of an array of waveguide tubes in which focusing is achieved by means of the phase correction introduced by the tube length or tube section profile [63]. Zoning is introduced in this configuration not only to keep the profile low, but also to reduce the weight. It is interesting to note that zoning also results in an improvement of the lens bandwidth, as short weveguides reduces the phase distortion due to dispersion. Such a lens can be fabricated using light metals, and it was reported that a bandwidth of between 5% and 15% can be achieved.

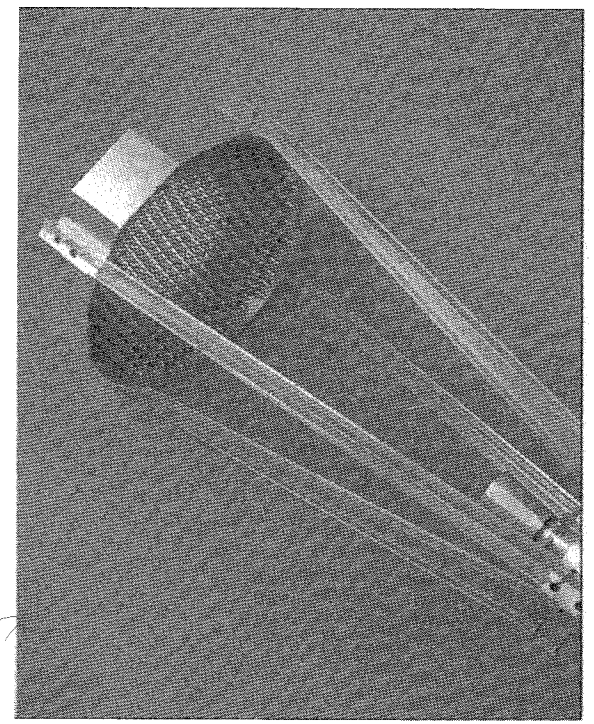

Fig. 7.4 A Fresnel zone using waveguides. Microwave Engineering Europe

7.5 Cylindrical Fresnel Lens

Although most of the material presented so far in this book is devoted to flat Fresnel zoneplate antennas, Fresnel antennas with curved surfaces do find applications in practice. A cylindrical Fresnel lens antenna was proposed as a candidate for base station antennas in wireless communications [58]. The antenna is constructed from a cylinder with metal opaque zones and is fed by a dipole placed along the axis of the cylinder (see Fig. 7.5). A sharp beam is formed in the elevation (θ direction) by the diffraction caused by the zonal cylinder, and the direction of the main beam is controlled by moving the position of the dipole along the central axis of the cylinder, thus providing wide-coverage tilt capability. As a circularly

symmetrical structure, the antenna pattern is omni-directional in the azimuth (φ direction), so it is mainly suited for micro-cellular and pico-cellular mobile communications systems and wireless local area networks (WLANs).

As a simple Fresnel lens, the cylindrical antenna has high sidelobes and low efficiency. The advantage is that a high directivity can be achieved in the elevation with a simple and low-cost structure.

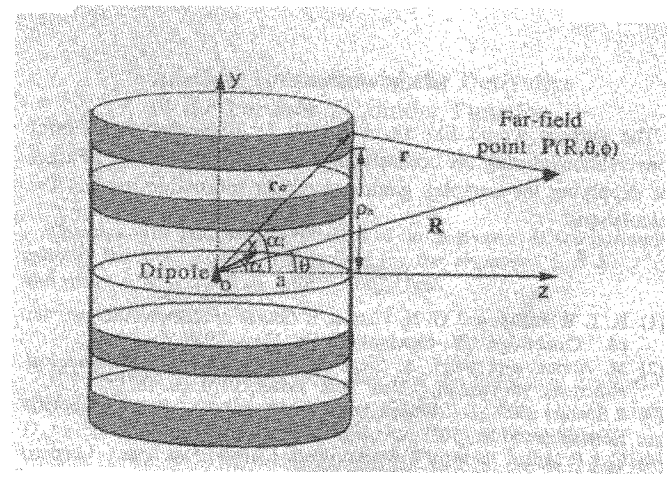

Fig. 7.5 A cylindrical Fresnel lens antenna for wireless LANs. IEEE

7.6 Fresnel Lens for Automotive Radar

Recently, there has been a fast growing interest in microwave and millimetre-wave sensors (radar) for industrial and domestic applications, one of which is the automotive sensors [64]. The advanced automotive distance warning system to be installed on future cars will use front, side and rear radar to monitor obstacles. This car vision system determines the distance from and the speed of detected objects and alerts drivers if they are too close to an obstacle. Compared with other techniques such as laser and ultrasound, the microwave/millimetre-wave radar are more robust in severe weather conditions and therefore more reliable. Undoubtedly, price is a key

issue in such consumer products and the low cost feature of the Fresnel zone antenna makes it a very competitive candidate.

A curved Fresnel lens antenna has been considered as an automotive radar antenna by Russian scientists I. V. Mini and O. V. Mini [64] in a research project sponsored by Daimler Chrysler AG. Although referred to as quasi-optical diffraction element (QDE), it is basically a quarter-wave Fresnel lens antenna (see Fig. 7.6). The following characteristics of the QDE were reported in [64]:

Penetration loss: ≤ 2 dB

beamwidth in azimuth plane (3 dB points): less than 1°

Sidelobe level: ≤ -30 dB

Angular coverage in azimuth plane: up to (-30°, 30°).

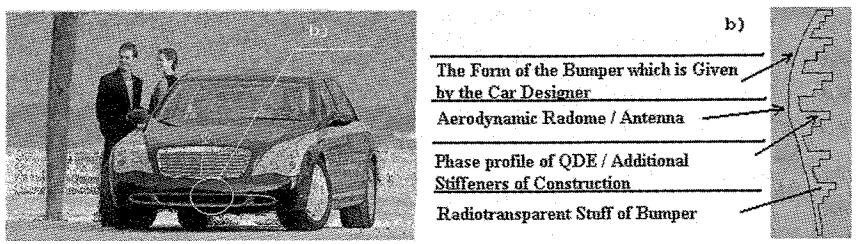

Fig. 7.6 A curved Fresnel lens antenna used for automotive radar. Permitted to publish by Professors I. V. Minin and O. V. Minin.

7.7 Integrated-Circuit Fresnel Zone Antenna

An integrated circuit millimetre wave Fresnel zoneplate antenna was reported in [57]. The antenna is based on the principle of phase reversal zoneplate described in chapter 3. It is composed of a Fresnel zoneplate on one side of the substrate with a strip dipole at the focal point of the zoneplate on the opposite side of the substrate (see Fig. 7.7). The novelty of this structure is that the feed element is naturally incorporated into the

feeding circuitry so the overall antenna system becomes compact. Compared with other millimetre-wave antennas, the production cost can be significantly reduced.

Thanks to the multi-layer structure, the integrated circuit millimetre wave zoneplate can be analysed accurately using spectral domain integral equation techniques. As a quasi-optical device, however, it is found that the radiation field of the antenna can be predicted using a simpler approach as follows. First, the radiation field of a dipole located at the boundary of half free space and half dielectric space is obtained by using the classical plane wave expansion approach. Second, the induced current on the zoneplate is obtained using the physical optics approximation. Third, the reflector behind the zoneplate is modelled by placing fictitious conducting rings between the actual conducting rings of the zoneplate. To account for the phase correction introduced by the $\lambda/4$ spacing between the reflector and the zoneplate, a phase shift of π is added to the physical optics current on the fictitious rings. Fourth, the radiation field of the induced current is calculated using the plane wave expansion method again. Finally, the radiation field of the zoneplate antenna is calculated as the sum of the direct radiation from the dipole and the contribution from the induced current. It is found that the approach described above provides reliable results when the focal length of the antenna is long [57].

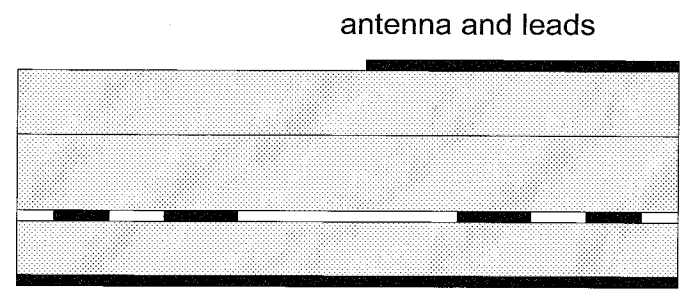

Fig. 7.7 Sectional view of the integrated Fresnel zone antenna.

It is interesting to note that when a printed antenna is placed at the interface between two different dielectric half space, the boundaries of the half-wave zones differ from those in free space. Therefore, the straightforward geometrical design approach given in chapter 2 becomes

sub-optimum. An optimum design should be based on the phase variation of the radiation field of the radiating elements in the dielectric. Obviously, the distortion on the width and shape of the zonal regions depends on the permittivity of the dielectric material used. The higher the permittivity, the greater the distortion becomes.

7.8 Suggestions for Future Work

We conclude with a brief discussion on the future of Fresnel zone antennas. It appears that there are at least four areas for further research. First, the application of the Fresnel zone concept and phase correcting techniques to various types of antennas, such as the cylindrical antenna described in section 7.5. Second, the development of efficient and low-cost phase correcting techniques. The third area of interest includes accurate analysis and design of phase correcting flat antennas, prediction of power handling ability and power dissipation in the dielectric used in the antenna [5, 61]. The fourth area is the study of broadband Fresnel zone antennas. One possible solution to increase the bandwidth of the Fresnel zone antenna is to use mutiple-band resonators, which has been employed in the FSS study [62], as phase correcting elements. At the moment, the telecommunications industry is moving toward the Universal Mobile Telecommunications Service (UMTS) and other broadband systems, and there is a high demand for novel antenna solutions to satellite, cellular mobile and wireless LAN radio problems. In the meantime, the automotive industry is introducing more and more radio technology to make driving a safer and more enjoyable experience. It is believed that low-cost and broadband Fresnel zone antennas will find many applications in those areas.

Bibliography

1. R. W. Wood, 'Phase-Reversal Zone Plates and Diffraction-Telescopes', *Phil. Mag.*, S.5, June 1898, vol. 45, no. 277, pp.511-523.

2. J. E. Garret and J. C. Wiltse, 'Fresnel Zone Plate Antennas at Millimetre Wavelength', *Int. Journal of Infrared and Millimetre Waves*, vol.12, no.3, Dec. 1991, pp.195-216.

3. I. Maddaus, "The Fresnel Zone Plate Antenna", NRL Report No. R-3293, Naval Research Laboratory, June 1948.

4. L. F. Van Buskirk and C. E. Hendrix, 'The Zone Plate as a Radio Frequency Focusing Element', *IRE Trans. Antennas Propagat.*, vol. 9, May 1961, pp.319-320.

5. D. N. Black and J. C. Wiltse, 'Millimetre-Wave Characteristics of Phase-Correcting Fresnel Zone Plates', *IEEE Trans Microwave Theory Tech,* vol. MTT-35, no. 12, Dec. 1987, pp.1122-1128.

6. B. Huder and W. Menzel, 'Flat printed reflector antenna for mm-wave applications', *Electron. Lett.*, vol. 24, no. 6, Mar. 1988, pp.318-319.

7. J. M. Franke and B. D. Leighty, "Reflection-Zone-Plate Antenna", NASA Tech Briefs, Feb. 1989.

8. W. L. H. Shuter, C. P. Chan, E. W. P. Li and A. K. C. Yeung, "A Metal Plate Fresnel Lens for 4GHz Satellite TV Reception", *IEEE Trans. Antennas Propagat.,* vol. AP-32, no. 3, March 1984., pp. 306 - 307.

9. R. Lambley, "Fresnel Antenna", *Electronics & Wireless World*, August, 1989, p. 792.

10. Y. J. Guo and S. K. Barton, "Offset Fresnel Zone Plate Antennas", *International Journal of Satellite Communications*, vol. 12, 1994, pp. 381-385.

11. Y. J. Guo, I. H. Sassi and S. K. Barton, "Offset Fresnel Lens Antenna", *IEE Proc. -Microwave Antennas and Propagation*, vol. 141, no. 6, December 1994, pp. 517-522.

12. Y. J. Guo and S. K. Barton, "Flat Printed Zone Plate Antennas for DBS Reception", Proceedings of 1992 International Broadcasting Convention, Amsterdam, July 1992, pp. 355-358.

13. Y. J. Guo and S. K. Barton, "On the Subzone Phase Correction of Fresnel Zone Plate Antennas" , *Microwave and Optical Technology Letters*, vol. 16, no. 15, Dec. 1993, pp. 840-843.

14. Y. J. Guo and S. K. Barton, "Multilayer Phase Correcting Fresnel Zone Plate Reflector Antennas", *International Journal of Satellite Communications*, vol. 11, no. 2, 1993, pp. 75-80.

15. Y. J. Guo, I. H. Sassi and S. K. Barton, "Multilayer Offset Fresnel Zone Plate Reflector", *IEEE Microwave and Guided Wave Letters*, vol. 4, no. 6, June 1994, pp. 196-198.

16. Y. J. Guo and S. K. Barton, "Analysis of One-Dimensional Zonal Reflectors", *IEEE Transactions on Antennas and Propagation*, vol. 43, no. 4, April 1995, pp. 385-389.

17. Y. J. Guo and S. K. Barton, "Fresnel Zone Plate Reflector Incorporating Rings", *IEEE Microwave and Guided Wave Letters*, vol. 3, no. 11, Nov. 1993, pp. 417-419.

18. Y. J. Guo and S. K. Barton, "Phase Correcting Zonal Reflector Incorporating Rings", *IEEE Transactions on Antennas and Propagation*, vol. 43, no. 4, April 1995, pp. 350-355.

19. Y. J. Guo and S. K. Barton, "Phase Efficiency of the Reflective Array Antenna", *IEE Proc. -Microwave Antennas and Propagation*, vol. 142, no. 2, April 1995, pp. 115-120.

20. R. E. Collin, Antennas and Radiowave Propagation, McGraw-Hill, 1985.

21. A. C. Ludwig, 'The Definition of Cross-Polarisation', *IEEE Trans. Antennas Propagat.*, vol. 21, no. 1, Jan. 1973, pp.116-119.

22. L. Leyten and M. H. A. J. Herben, 'Vectorial Analysis Of the Fresnel-Zone plate Antenna: A Comparison With the Parabolic Reflector Antenna', *Microwave and Optical Technology Letters*, vol. 5, no. 2, Feb. 1992, pp49-55.

23. R. Mittra, Y. Rahmat-Samii, V. Galindo-Israel, and R. Norman, 'An Efficient Technique for the Computation of Vector Secondary Patterns of Offset Paraboloid Reflectors', *IEEE Trans. Antennas Propagat.*, vol. 27, no. 3, May 1979, pp.294-304.

24. M. S. Narasimhan and M. Karthikeyan, 'Evaluation of Fourier Transform Integrals Using FFT with Improved Accuracy and Its Application', *IEEE Trans. Antennas Propagat.*, vol. 32, no. 4, April 1984, pp.404-408.

25. D. Pozar, Antenna Design Using Personal Computers, Artech House, Inc., 1985.

26. C. J. Sletten, Reflector and Lens Antennas, Artech House, 1988

27. Y. J. Guo and S. K. Barton, "Offset Fresnel Zone Plate Antennas", 18th Antenna Symposium, Queen Mary and Westfield College, London, March 1992.

28. Y. J. Guo, S. K. Barton and T. M. B. Wright, "Focal Field Distribution of Fresnel Zone Plate Antennas", Proceedings of the International Conference on Antennas and Propagation (ICAP'91), York, UK, April 1991, pp. 6-8.

29. Y. J. Guo, S. K. Barton and T. M. B. Wright, "Design of High Efficiency Fresnel Zone Plate Antennas", 1991 IEEE AP-S International Symposium Digest, Canada, June 1991, pp. 182-185.

30. Y. J. Guo and S. K. Barton, "A High Efficiency Quarter-Wave Zone Plate Reflector", *IEEE Microwave and Guided Wave Letters*, vol. 2, no. 12, Dec. 1992, pp. 470-471.

31. Y. J. Guo and S. K. Barton, "On the Sidelobe Performance of Fresnel Zone Plate Antennas", 1992 IEEE AP-S International Symposium Digest, Chicago, USA, June 1992, pp. 2175-2178.

32. J. D. Kraus, Antennas, McGraw-Hill Book Company, 1988.

33. W. E. Kock, 'Metal-Lens Antennas', *Proceedings of the IRE*, vol. 34, Nov., 1946, pp.828-836.

34. G. Colinge, Private Communications, 1993.

35. R. F. Harrington, Field Computation by Moment Methods, Macmillan, 1968.

36. W. L. Stuzman and G. L. Thiele, Antenna Theory and Design, John Wiley & Sons, Inc., 1981.

37. H. D. Griffith and K. Milne, "Planar Phase Shifting Structures for Steerable DBS Antennas", Proceedings of the International Conference on Antennas and Propagation (ICAP'89), April, 1989, pp. 45-49.

38. Y. J. Guo and S. K. Barton, "Flat Printed Lens and Reflector Antennas", Proceedings of the International Conference on Antennas and Propagation (ICAP'95), the Netherlands, April 1995, pp. 253-256.

39. E. A. Parker and S. M. A. Hamdy, 'Rings as Elements for Frequency Selective Surfaces', *Electron. Lett.*, vol. 17, no. 17, Aug. 1981, pp.612-614.

40. Y. J. Guo and S. K. Barton, 'High Efficiency Zone Plate Reflector Incorporating Printed Resonators', Proc. of the 8th Int. Conf. on Antennas and Propagation, Edinburgh, UK, 1993, pp.620-622.

41. R. Milne, "Dipole Array Lens Antennas", *IEEE Trans. Antennas Propagat.*, vol. AP-30, no. 4, July 1982.

42. Craig Scott, The Spectral Domain Method in Electromagnetics, Artech House, Inc., 1989.

43. N. Amitay, V. Galindo and C. P Wu, Theory and Analysis of Phased Array Antennas, John Wiley & Sons, New York, 1972.

44. Y. J. Guo and S. K. Barton, "Printed Zonal Reflector With Phase Shifting Rings", 20th Antenna Symposium, Queen Mary and Westfield College, London, March 1994.

45. http://www.maliburesearch.com/.

46. Y. J. Guo and S. K. Barton, "Spectral Domain Moment Method Analysis of Reflective Phase Shifters and Its Application to a Flat Reflector Antenna", Proceedings of the 1994 International Conference on Computational Electromagnetics and Its Applications (ICCEA'94), Beijing, China, November 1994, pp. 413-416.

47. D. G. Berry, et al., 'The Reflectarray Antenna', *IEEE Transactions on Antennas and Propagation,* November 1963, pp.645-651.

48. Y. J. Guo, I. H. Sassi and S. K. Barton, "A New Flat Reflector with Phase Shifting Tiles", Proceedings of the 1994 Progress in Electromagnetics Research Symposium (PIERS'94), Noordwijk, The Netherlands, July, 1994, pp.2041-2044.

49. I. H. Sassi, Y. J. Guo and S. K. Barton, "Reflective Phase Correcting Array with Dielectric Tiles", 20th Antenna Symposium, Queen Mary and Westfield College, London, March 1994.

50. A. C. Schell, et al., 'An Experimental Evaluation of Multiplate Antenna Properties', *IEEE Transactions on Antenna and Propagation*, vol. AP-14, no. 5, Sept. 1966, pp.543-550.

51. H. Taub and D. L. Schilling, Principles of Communication Systems, McGraw-Hill Book Company, 1986.

52. B. D. Steinberg, Principles of Aperture and Array System Design, John Wiley & Sons, 1976.

53. J. Ruze, 'Antenna Tolerance Theory - A Review', *Proc. IEEE*, vol. 54, April 1966, pp.633-640.

54. J. C. Wiltse and J. E. Garrett, ' The Fresnel Zone Plate Antenna', *Microwave Journal*, January 1991, pp. 101-114.

55. H. D. Hristov and H. A. J. Herben, "Millimetre-Wave Fresnel Zone Plate Lens and Antenna", *IEEE Trans Microwave Theory Tech.*, vol. MTT-43, no. 12, December 1995, pp. 2779 - 2785.

56. M. Marin et al, "Lens Antennas: A Study of Their Potential for Satellite Missions", Microwave Engineering Europe, August/September 1992.

57. M. A. Gouker and G. S. Smith, " A millimeter-wave integrated-circuit antenna based on the Fresnel zoneplate", *IEEE Trans. Microwave Theory Tech.*, vol. MTT-40, May 1992, pp. 968-977.

58. Y. Ji and M. Fujita, "A Cylindrical Fresnel Zone Antenna", *IEEE Trans. Antennas Propagat.*, vol. AP-44, no. 9, Sept. 1996, pp. 1300-1301.

59. Y. J. Guo and S. K. Barton, "A Spectral Domain Method for Analysing Flat Printed Zone Plate Antennas", Proceedings of the URSI International Symposium on Electromagnetic Theory, Sydney, August 1992, pp. 372-374.

60. Y. J. Guo and S. K. Barton, "CG-FFT Analysis of Two Dimensional Fresnel Zone Plate Antennas", Proceedings of the 8th Annual Review of Progress in Applied Computational Electromagnetics, Monterey, USA, March 1992, pp. 258-265.

61. Y. J. Guo, S. K. Barton and T. M. B. Wright, "Reflection Efficiency of the Phase Reversal Zone Plate Antenna Made of Thin Conducting Film", IEE Colloquium on Material and Manufacturing Process for Antennas, London, November 1990.

62. R. J. Langley and E. A. Parker, "Double-Square Frequency-Selective Surfaces and Their Equivalent Circuit", *Electron. Lett.*, vol. 19, no. 17, Aug. 1983, pp.675-676.

63. M. Marin, P. G. Muller and A. Rodriguez, "Lens Antennas: A Study of Their Potential for Satellite Missions", Microwave Engineering Europe, August/September 1992.

64. Minin I.V. and Minin O.V. "Diffraction quasioptics and its application", SibAgs Publisher, Novosibirsk, 1999. - 308 p. (in Russian).

65. Hristo D. Hristov. "Fresnel Zones in wireless links, zone plate lenses and antennas", Artech House, Boston, London, 2000.

Index